July–August 1984
Vol. 63 No. 6 Part 1

AT&T
BELL LABORATORIES

TECHNICAL JOURNAL

A JOURNAL OF THE AT&T COMPANIES

Reflection Coefficient for Optical Waveguide

Transmultiplexers

Soliton Propagation in Materials

Integrated Circuit Fabrication

Radio-Wave Attenuation

Companded PCM

EDITORIAL COMMITTEE

A. A. PENZIAS,[1] *Committee Chairman*

M. M. BUCHNER, JR.[1]
R. P. CLAGETT[2]
R. P. CREAN[2]
B. R. DARNALL[1]
B. P. DONOHUE, III[3]
R. C. FLETCHER[1]
D. HIRSCH[4]
S. HORING[1]
R. A. KELLEY[1]
J. F. MARTIN[2]
J. S. NOWAK[1]
B. B. OLIVER[5]
J. W. TIMKO[3]
V. A. VYSSOTSKY[1]

[1]AT&T Bell Laboratories [2]AT&T Technologies [3]AT&T Information Systems
[4]AT&T Consumer Products [5]AT&T Communications

EDITORIAL STAFF

B. G. KING, *Editor*
P. WHEELER, *Managing Editor*
L. S. GOLLER, *Assistant Editor*
A. M. SHARTS, *Assistant Editor*
B. G. GRUBER, *Circulation*

AT&T BELL LABORATORIES TECHNICAL JOURNAL (ISSN0005-8580) is published ten times each year by AT&T, 550 Madison Avenue, New York, NY 10022; C. L. Brown, Chairman of the Board; T. O. Davis, Secretary. The Computing Science and Systems section and the special issues are included as they become available. Subscriptions: United States—1 year $35; 2 years $63; 3 years $84; foreign—1 year $45; 2 years $73; 3 years $94. A subscription to the Computing Science and Systems section only is $10 ($12 foreign). Single copies of most issues of the Journal are available at $5 ($6 foreign). Payment for foreign subscriptions or single copies must be made in United States funds, or by check drawn on a United States bank and made payable to the Technical Journal and sent to AT&T Bell Laboratories, Circulation Dept., Room 1E335, 101 J. F. Kennedy Pky, Short Hills, NJ 07078.

Single copies of material from this issue of the Journal may be reproduced for personal, noncommercial use. Permission to make multiple copies must be obtained from the Editor.

Comments on the technical content of any article or brief are welcome. These and other editorial inquiries should be addressed to the Editor, AT&T Bell Laboratories Technical Journal, Room 1H321, 101 J. F. Kennedy Pky, Short Hills, NJ 07078. Comments and inquiries, whether or not published, shall not be regarded as confidential or otherwise restricted in use and will become the property of AT&T. Comments selected for publication may be edited for brevity, subject to author approval.

Printed in U.S.A. Second-class postage paid at Short Hills, NJ 07078 and additional mailing offices. Postmaster: Send address changes to the AT&T Bell Laboratories Technical Journal, Room 1E335, 101 J. F. Kennedy Pky, Short Hills, NJ 07078.

Copyright © 1984 AT&T.

AT&T Bell Laboratories

Technical Journal

VOL. 63 JULY-AUGUST 1984 NO. 6, PART 1

Copyright © 1984 AT&T, Printed in U.S.A.

Exact Calculation of the Reflection Coefficient for Coated Optical Waveguide Devices 857
D. R. Kaplan and P. P. Deimel

The LT-1 Connector Family of Transmultiplexers 879
G. W. Bleisch, W. J. Mitchell, and S. Dodds

Electrical Transmission Lines as Models for Soliton Propagation in Materials: Elementary Aspects of Video Solitons 901
G. E. Peterson

800-MHz Attenuation Measured In and Around Suburban Houses 921
D. C. Cox, R. R. Murray, and A. W. Norris

Transmission Errors in Companded PCM Over Gaussian and Rayleigh Fading Channels 955
R. Steele, C.-E. Sundberg, and W. C. Wong

Overtone Absorption and Raman Spectra of H_2 and D_2 in Silica Optical Fibers 991
J. Stone, A. R. Chraplyvy, J. M. Wiesenfeld, and C. A. Burrus

PAPERS BY AT&T BELL LABORATORIES AUTHORS **1001**

CONTENTS, SEPTEMBER ISSUE **1005**

AT&T Bell Laboratories Technical Journal
Vol. 63, No. 6, July–August 1984
Printed in U.S.A.

Exact Calculation of the Reflection Coefficient for Coated Optical Waveguide Devices

By D. R. KAPLAN* and P. P. DEIMEL*

(Manuscript received March 8, 1984)

We derive an exact solution to the problem of the reflection coefficient for a coated slab waveguide. A series of computer calculations apply these results to a $\lambda = 1.3$ μm InGaAsP laser with an active area of 0.2 micron, an active area index of refraction of 3.51, and a cladding index of refraction of 3.22. Our results show that the correction due to the index step is a few percent for an uncoated laser. For antireflection coatings (reflectivity less than 1 percent), the correction due to the index step is significant. These results are important in choosing coating indices and thicknesses when minimum reflectivities are desired (e.g., for a superluminescent diode). The results, calculated over a range of indices of refraction of the coating, show that the TE and TM reflectivities are minimized at about the same value of the index, 1.84. However, the coating thicknesses at which the reflectivity is minimized are different for the TE and TM case. For example, when the TE reflectivity is minimized, the TM reflectivity exceeds the TE reflectivity by over two orders of magnitude.

I. INTRODUCTION

The reflectivity of light from optical waveguide devices can be modified by the application of suitably chosen coatings. Examples of waveguide devices include semiconductor lasers, optical switches, optical modulators, and optical fibers. In this paper an exact solution to the problem of the reflectivity from single transverse mode, two-dimensional waveguide devices (such as slab waveguides) is derived

* AT&T Bell Laboratories.

Copyright © 1984 AT&T. Photo reproduction for noncommercial use is permitted without payment of royalty provided that each reproduction is done without alteration and that the Journal reference and copyright notice are included on the first page. The title and abstract, but no other portions, of this paper may be copied or distributed royalty free by computer-based and other information-service systems without further permission. Permission to reproduce or republish any other portion of this paper must be obtained from the Editor.

and the results are applied to a typical gain-guided semiconductor laser. The calculation is only limited to a single transverse mode for convenience. The extension to a multimode system is straightforward.

The problem of reflectivity from an uncoated laser was described in detail by McKenna[1] and his method was employed by Reinhart et al.,[2] Gordon,[3] and Krupka.[4] The eigenstates in the waveguide consist of a discrete set of bound modes and a continuous set of unbound modes. A numerical calculation for the uncoated laser was performed by Ikegami,[5] although he neglected the continuous part of the spectrum. Pudensi and Ferreira[6] have developed a method to correct for this by combining the continuous modes to form a discrete description of the continuum. Kardontchik[7] used a method similar to Ikegami to calculate the reflectivity for three-dimensional laser structures.

Clarke[8] suggested an approximate method to calculate the reflectivity from an antireflection coated laser. However, that approximation is based on truncating the angular spectrum of the incident bound state. This approximation is especially poor when the reflectivity is calculated for a coating close to the quarter-wave condition. The problem of mode conversion by reflection from the mirror facets in an uncoated laser was considered in detail by Lewin.[9]

II. MODEL

The detailed derivation of the reflection coefficient is described in the Appendix. This section describes the model for the calculation and gives the analytical results.

The model used for this calculation is shown in Fig. 1. The wave incident on the boundary between regions 1 and 2 is described by a single bound state, ψ. The collection of all unbound states, ϕ_k, plus the bound state, ψ, forms a complete orthogonal set inside the waveguide (region 1). The arrows labeling the states in Fig. 1 denote whether the state has a wave vector with a positive z component (e.g., $\vec{J}$) or negative z component (e.g., $\overleftarrow{J}$).

Inside the coating (region 2) the states may be described as an infinite sum of plane waves and evanescent fields. Finally, in air (region 3) the complete set is again a set of plane waves and evanescent fields.

The boundary between regions 1 and 2 cannot, in general, be described as the boundary between two uniform media. In addition, the states, ϕ_k, are not plane waves. As a result, the Fresnel reflection coefficients,[10] which were used extensively in previous calculations,[1-4,8] are not, in principle, valid for this problem. We define $\Delta n(x)$ as the difference between the refractive index inside the laser at position x, $(n_1(x))$, and the refractive index of the cladding layers at position $x =$

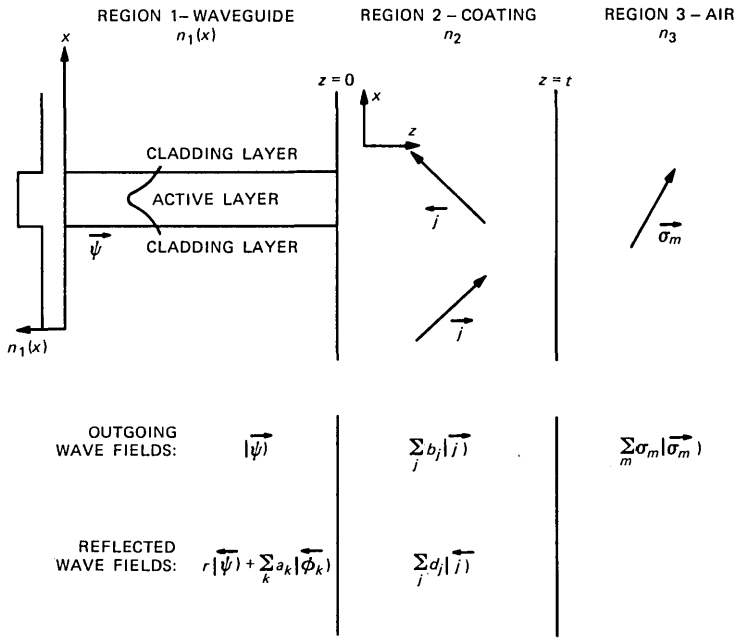

Fig. 1—Two-dimensional model used in calculation.

$\pm\infty$, (n_1^0). For the case of an asymmetric waveguide $\Delta n(x)$ is the difference between the refractive index at position x and the average of the refractive index of the cladding layers at positions $x = +\infty$ and $x = -\infty$ (see Section III). In the limit that $\Delta n(x)$ approaches zero for all x, the unbound states in region 1 again become plane waves and the Fresnel reflection coefficients are again valid. In this condition the bound state, ψ, can be expressed as a sum over plane waves.* For each plane wave there is a different reflectivity at the interface between regions 1 and 2, r_{12}^j, where j denotes a particular plane wave transmitted into region 2.

The method adopted in this paper is to calculate the reflection coefficient, r, in the limit that $\Delta n(x)$ approaches zero and then calculate an infinite perturbation expansion in terms of a suitably chosen integral of $\Delta n(x)$. By r we mean the amplitude for the bound state to reflect back onto the same bound state. This number is important in determining the threshold condition for semiconductor laser operation.

Since we are concerning ourselves with a slab waveguide, we can break the problem into the solution of TE modes and TM modes.

* When $\Delta n(x) = 0$ for all x, there are no bound states. In general, ψ corresponds to a sum of plane waves only at a given surface z = constant.

The results for the TE modes are

$$r_{\mathrm{TE}} = \int_{-\infty}^{\infty} ds_2 f(s_2) f^*(s_2) R(s_2) + \int_{-\infty}^{\infty} ds_2 f^*(s_2) \Delta(s_2) \frac{[R(s_2) + 1]}{2n_1^0 h_1^0(s_2)}, \quad (1)$$

where the zeroth approximation to $\Delta(s_2)$ is given by

$$\Delta^{(0)}(s_2) = \int_{-\infty}^{\infty} ds_2' \Delta H(s_2, s_2') f(s_2')(1 - R(s_2')), \quad (2)$$

and the ith approximation to $\Delta(s_2)$ is

$$\Delta^{(i)}(s_2) = \Delta^{(0)}(s_2) - \int_{-\infty}^{\infty} ds_2' \Delta H(s_2, s_2') \Delta^{(i-1)}(s_2') \left[\frac{R(s_2') + 1}{2n_1^0 h_1^0(s_2')}\right]. \quad (3)$$

The terms of the above expression are now described. The Fourier transform of the bound state, $f(s_2)$, is given by

$$f(s_2) = \frac{1}{\sqrt{\lambda_2}} \int_{-\infty}^{\infty} dx\, \vec{\psi}(x)\, e^{-ik_2 s_2 x}, \quad (4)$$

where λ_2 is the wavelength of the light inside the coating, λ_0 is the wavelength in vacuum, n_2 is the index of the coating layer, and $k_2 = 2\pi n_2/\lambda_0$. The complex conjugate of $f(s_2)$ is given by $f^*(s_2)$. For $|s_2| < 1$ in eqs. (1) through (4), s_2 is equivalent to the $\sin(\Theta)$, where Θ is the angle of the transmitted plane wave in the coating relative to the normal vector of the surface between regions 1 and 2. Also, $R(s_2)$ is the Fresnel reflection coefficient for a field incident (at a coating angle Θ) onto the coated interface.[10] Thus,

$$R(s_2) = \frac{r_{12}(s_2) + r_{23}(s_2)\, e^{2i\phi(s_2)}}{1 + r_{12}(s_2) r_{23}(s_2)\, e^{2i\phi(s_2)}}, \quad (5)$$

where r_{12} is the Fresnel reflection coefficient for the semi-infinite boundary between regions 1 and 2, r_{23} is the Fresnel reflection coefficient between regions 2 and 3, and

$$\phi(s_2) = \frac{2\pi n_2 t}{\lambda_0} \sqrt{1 - s_2^2}. \quad (6)$$

The index of refraction of the coating is n_2. The thickness of the coating is t, and λ_0 is the wavelength in vacuum.

Furthermore,

$$h_1^0(s_2) = \sqrt{1 - \left(\frac{n_2 s_2}{n_1^0}\right)^2}, \quad (7)$$

$$h_1(s_2, x) = \sqrt{1 - \left(\frac{n_2 s_2}{n(x)}\right)^2}, \quad (8)$$

and

$$\Delta H(s_2, s_2') = \frac{n_2}{\lambda_0} e^{ik_0 n_2 x(s_2 - s_2')} [h_1(s_2', x) n_1(x) - h_1^0(s_2') n_1^0], \tag{9}$$

where $k_0 = 2\pi/\lambda_0$.

The first term in eq. (1) is the Fresnel approximation to the reflection coefficient. The second term in eq. (1) is the correction due to the presence of $\Delta n(x)$ in region 1. With eq. (3) the higher-order correction terms are calculable. These terms are negligible for the laser configuration described below.

Equation (5) shows how the reflection coefficient can easily be generalized for a multiple coating condition. The reflection coefficients, $r_{12}(s_2)$ and $r_{23}(s_2)$, are single-interface Fresnel reflection coefficients. Only the interface between regions 2 and 3 plays a role in the coefficient r_{23}. For a multiple layer condition r_{23} is replaced by the effective reflection coefficient for a plane wave incident from region 2 onto a series of layers.

For the TM, results below a "~" mean that TM parameters (as opposed to TE parameters) are used. Thus,

$$\begin{aligned} r_{\mathrm{TM}} = & \int_{-\infty}^{\infty} ds_2 \tilde{f}^*(s_2) \tilde{f}(s_2) \tilde{R}(s_2) \\ & + \frac{n_2}{n_1} \int_{-\infty}^{\infty} ds_2 (1 + \tilde{R}(s_2)) \left[\tilde{f}(s_2^*) + \int_{-\infty}^{\infty} ds_2' \Delta\tilde{D}(s_2, s_2') \right] \\ & \cdot \left\{ \frac{\tilde{\Delta}^A(s_2)}{2h_1^0(s_2)} + \frac{\tilde{\Delta}^B(s_2)}{2n_1^0} \right\} \\ & + \int_{-\infty}^{\infty} ds_2 (1 + \tilde{R}(s_2) \tilde{f}(s_2)) \int_{-\infty}^{\infty} ds_2' \Delta D(s_2, s_2') \tilde{f}^*(s_2'), \end{aligned} \tag{10}$$

where

$$\Delta\tilde{D}(s_2, s_2') = \frac{n_2}{\lambda_0} \int_{-\infty}^{\infty} dx\, e^{ik_0 n_2 (s_2 - s_2')x} \left[\frac{n_1^0}{n_1(x)} - 1 \right], \tag{11}$$

$$\tilde{\Delta}^{A(0)}(s_2) = \int ds_2' (1 - \tilde{R}(s_2')) \tilde{f}(s_2') \Delta h(s_2, s_2'), \tag{12}$$

$$\tilde{\Delta}^{B(0)}(s_2) = \int ds_2' (1 + \tilde{R}(s_2')) \tilde{f}(s_2') \Delta n(s_2, s_2'), \tag{13}$$

$$\begin{aligned} \tilde{\Delta}^{A(i)}(s_2) = & \tilde{\Delta}^{A(0)}(s_2) + \int_{-\infty}^{\infty} ds_2' \\ & \cdot \left\{ \tilde{\Delta}^{A(i-1)}(s_2') \frac{[-(1 + \tilde{R}(s_2'))]}{2h_1^0(s_2')} + \tilde{\Delta}^{B(i-1)}(s_2') \frac{[1 - \tilde{R}(s_2')]}{2n_1^0} \right\} \Delta h(s_2, s_2'), \end{aligned} \tag{14}$$

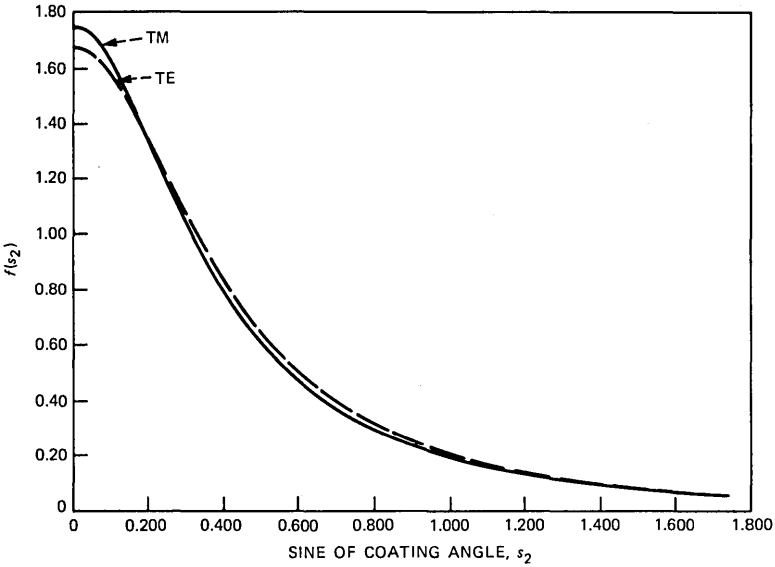

Fig. 2—The k-space wave functions of TE and TM modes. Solid curve is TE mode and dashed curve is TM mode.

$$\tilde{\Delta}^{B(i)}(s_2) = \tilde{\Delta}^{B(0)}(s_2) + \int_{-\infty}^{\infty} ds_2' \cdot \left\{ \tilde{\Delta}^{A(i-1)}(s_2') \frac{[1 + \tilde{R}(s_2')]}{2h_1^0(s_2')} - \tilde{\Delta}^{B(i-1)}(s_2') \frac{[1 - \tilde{R}(s_2')]}{2n_1^0} \right\} \Delta n(s_2, s_2'), \quad (15)$$

and

$$\Delta h(s_2, s_2') = \frac{n_2}{\lambda_0} \int_{-\infty}^{\infty} dx\, e^{ik_0 n_2 (s_2 - s_2')x} [h_1(s_2, x) - h_1^0(s_2)], \quad (16)$$

and

$$\Delta n(s_2, s_2') = \frac{n_2}{\lambda_0} \int_{-\infty}^{\infty} dx\, e^{ik_0 n_2 (s_2 - s_2')x} [n_1(x) - n_1^0]. \quad (17)$$

III. NUMERICAL CALCULATIONS

We now calculate several of the terms given in eqs. (1) through (17).

3.1 Determination of $f(s_2)$

The terms, $f(s_2)$, are the Fourier transforms of the incident wave function, according to eq. (4). The wave function, $\psi(x, z)$, is calculated by solving Maxwell equations in the infinite waveguide defined by $n_1(x)$. The wave functions used in the calculations below are the lowest-order TE mode and the lowest-order TM mode. The k-space wave functions are shown in Fig. 2.

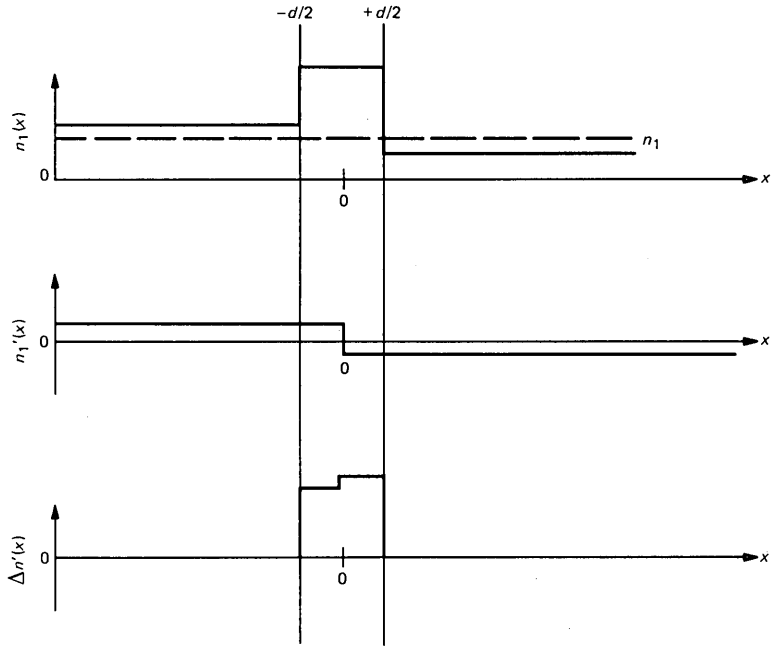

Fig. 3—Details of index step for an asymmetric waveguide.

3.2 Determination of $\Delta n(s_2, s_2')$

The correction integral, $\Delta n(s_2, s_2')$ in eq. (17), determines the strength of the correction term. For a symmetric step waveguide of thickness d, $\Delta n(s_2, s_2') = \dfrac{\Delta n d n_2}{\lambda_0}\left[\dfrac{\sin u}{u}\right]$, where $u = \dfrac{2\pi n_2}{\lambda_0}\dfrac{d}{2}(s_2 - s_2')$.

For real waveguide devices the index of refraction of the two cladding layers is not, in general, identical. Under these conditions $\Delta n(x)$ does not approach zero as x approaches $\pm\infty$. We must, therefore, show that the calculation of $\Delta n(s_2, s_2')$ for an asymmetric waveguide leads to a finite result. As Fig. 3 shows, $n_1(x)$ is broken into three terms: $n_1(x) = n_1 + n_1'(x) + \Delta n'(x)$. From eq. (8) we obtain

$$\begin{aligned}\Delta n(s_2, s_2') &= \frac{n_2}{\lambda_0}\int_{-\infty}^{\infty} dx\, e^{ik_0 n_2 x(s_2 - s_2')}(n_1'(x) + \Delta n'(x)) \\ &= \frac{n_2}{\lambda_0}\int_{-\infty}^{\infty} dx\, e^{ik_0 n_2 x(s_2 - s_2')} n_1'(x) + \frac{n_2}{\lambda_0}\int_{-\infty}^{\infty} dx\, e^{ik_0 n_2 x(s_2 - s_2')}\Delta n'(x). \qquad (18)\end{aligned}$$

The problem is solved by placing the system in a large box of length $2b$ where the length is defined along the x axis. The box then defines

the allowed values of k_x. By invoking periodic boundary conditions, k_x is quantized such that

$$k_x = m\delta k_0, \tag{19}$$

where $\delta k_0 = (2\pi)/b$ and m is an integer.

The first integral in expression (18) then becomes

$$\frac{n_2}{\lambda_0}\int_{-b}^{b} dx\, e^{i\frac{2\pi}{b}(m-m')x}\, n_1'(x) \propto [\cos(2\pi(m - m')) - 1] = 0. \tag{20}$$

We next allow b to approach infinity. Then, $\Delta n(s_2, s_2')$ is calculable with the modified step defined by $\Delta n'(x)$. This is a finite result for any guiding structure. Note that to solve the problem self-consistently, ψ must be recalculated for an asymmetric waveguide. In a similar manner, $\Delta h(s_2, s_2')$ [eq. (16)] and $\Delta H(s_2, s_2')$ [eq. (9)] can be calculated for an asymmetric waveguide.

3.3 Calculation of $R(s_2)$ and $\tilde{R}(s_2)$

R and $\tilde{R}$ are calculated in eq. (5) and are used in eqs. (1) and (10). Since the integrals extend from $-\infty$ to $+\infty$, $R(s_2)$ must be calculated for all values of s_2. There are three critical angles involved, as shown in Fig. 4:

$$s_{1c} = \frac{n_3}{n_2}$$

$$s_{2c} = 1$$

$$s_{3c} = \frac{n_1^0}{n_2}. \tag{21}$$

For $s_2 < s_{1c}$ an incident wave in region 1 is coupled to a reflected wave in region 1, two plane waves in region 2, and a transmitted plane wave in region 3.

For $s_{2c} < s_2 < s_{2c}$ an incident wave is coupled to a reflected wave in region 1, plane waves in region 2, and an evanescent field in region 3.

When $s_{2c} < s_2 < s_{3c}$ a wave incident in region 1 is coupled to evanescent fields in regions 2 and 3 and to a reflected wave in region 1.

When $s_2 > s_{3c}$ all the fields are evanescent fields.

The real and imaginary parts of $R(s_2)$ are plotted in Fig. 5a for a normalized coating thickness, $h = 0$, where $h = tn_2/\lambda_0$. Shown in Fig. 5b are the real and imaginary parts of the product $R(s_2)|f|^2$, which correspond to the integrand of the first term in eq. (1). Figures that are similar to Figs. 5a and b but are for the case of $h = 1/4$ are plotted in Figs. 6a and b. Note that the terms can be both positive and negative

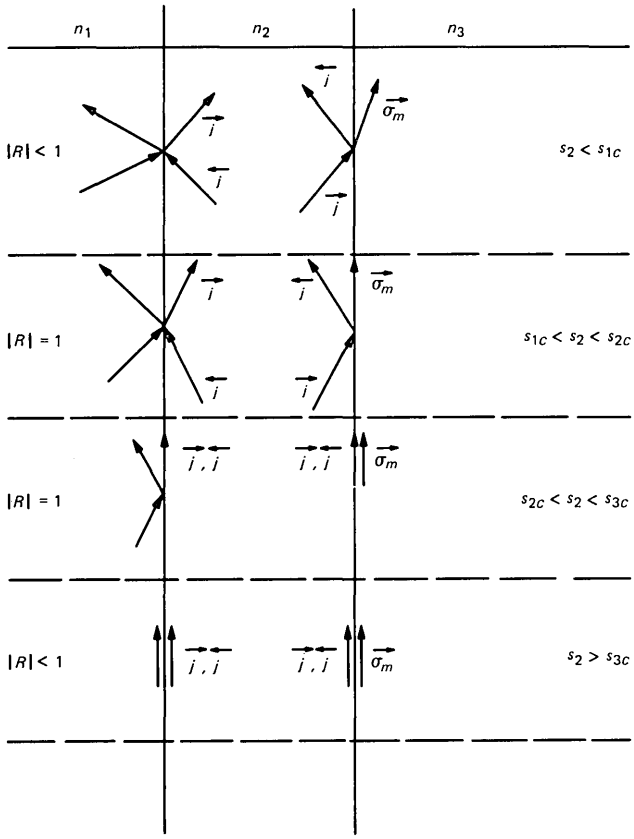

Fig. 4—The k-vectors for states involved in the calculation of $R(s_2)$ for all values of s_2.

and that a minimization may correspond to a balancing of the positive and negative parts of the integral. The cusps in the real and imaginary parts of $R(s_2)$ occur at the first critical angle. In the region of total reflection (from $s_2 = s_{2c}$ to $s_2 = s_{3c}$) $|R(s_2)|$ is equal to 1. The phase of the reflection coefficient varies in this region such that the real and imaginary parts of $R(s_2)$ take values between -1 and $+1$.

When the normalized thickness, h, is ~0.25, the relative weight of large s_2 terms ($s_2 \gtrsim 0.6$) is much more significant. Therefore, any calculation of r_{TE} or r_{TM} that is limited to the region of small incident angles is invalid for antireflection coatings.

IV. RESULTS

To demonstrate the above formalism, we have performed reflectivity calculations for a $\lambda_0 = 1.3$ μm laser with an index of refraction of 3.51

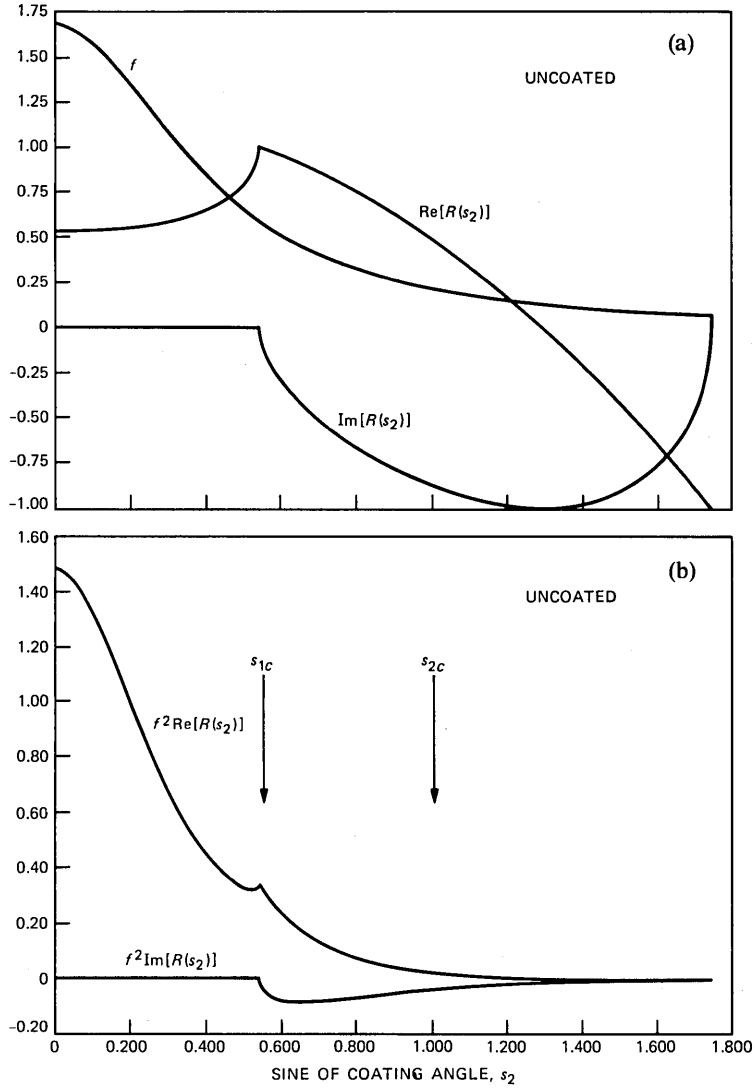

Fig. 5—Real and imaginary parts of (a) $R(s_2)$ for $h = 0$, and (b) $R(s_2)|f|^2$ for $h = 0$. $f(s_2)$ is shown for comparison.

for the active region and 3.22 for both cladding layers and with an active layer thickness of 0.2 micron. We have limited the calculations to the zeroth-order correction term.

The optimum reflectivity, $r^{\text{opt}}(n_2)$, is defined as the minimum of the $r(h)$ curve for a given coating index n_2. In Fig. 7 $r^{\text{opt}}(n_2)$ is plotted for various conditions. In all of these calculations the incident wave function is the zeroth mode of the laser waveguide described above.

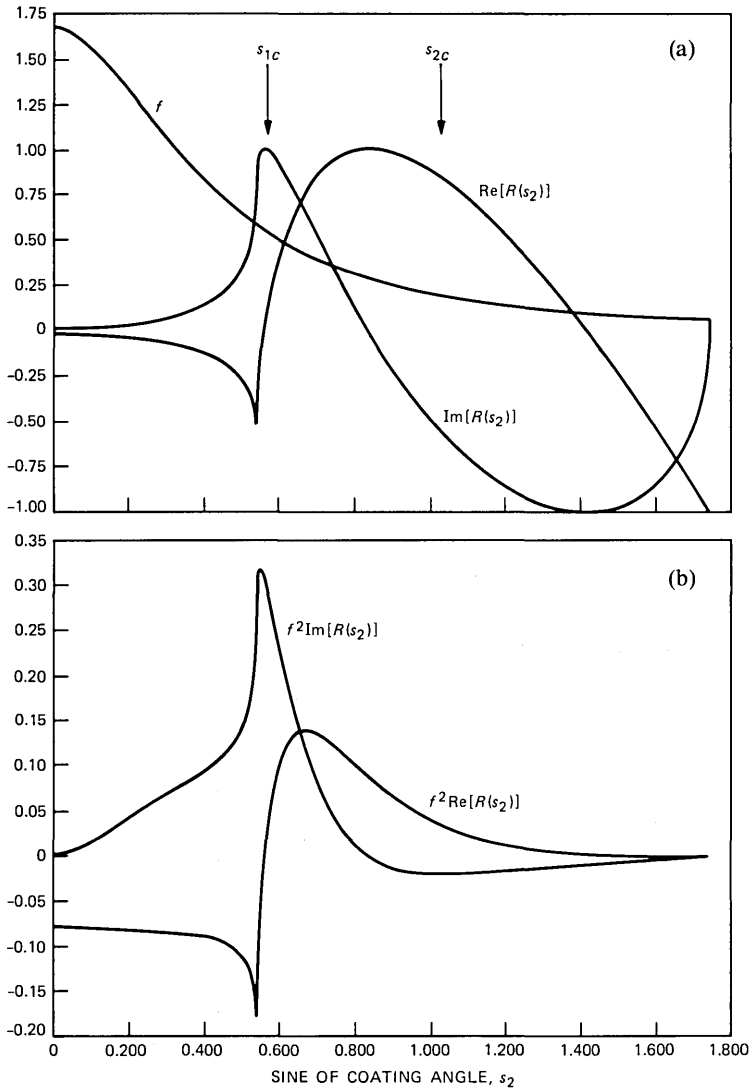

Fig. 6—Real and imaginary parts of (a) $R(s_2)$ for $h = 1/4$, and (b) $R(s_2)|f|^2$ for $h = 1/4$. $f(s_2)$ is shown for comparison.

The solid curves show the approximation in which the index of refraction of the laser is assumed to be constant and equal to that of the active layer. The dashed curves correspond to our calculations in which the correction terms are neglected. The dotted curves represent the calculation with the zeroth-order correction term included. Note that the result that includes the correction term lies between the results arrived at by assuming the index of the laser is a constant

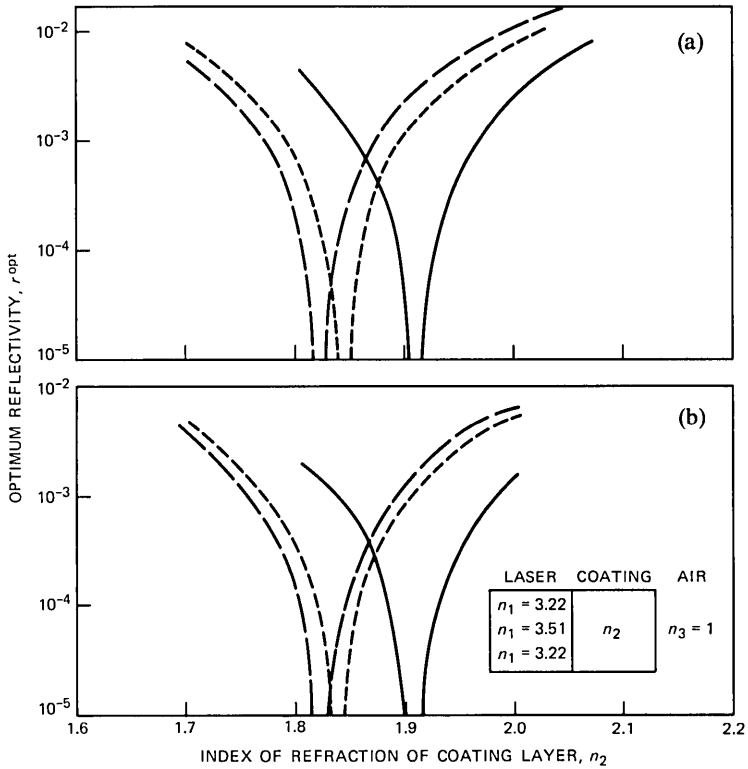

Fig. 7—Optimum reflectivity as a function of index of refraction of coating for (a) TE and (b) TM modes for laser structure shown in inset.

equal to the active area and the result in which the constant index is equal to that of the cladding.

Figure 7 demonstrates the significance of the error obtained when approximating the index of refraction inside the laser as a constant equal to the index of refraction of the active layer. The results shown in Fig. 7 are very similar for both the TE and the TM results. For the TE case the reflectivity is minimized at a coating index of refraction equal to 1.845. For the TM case the minimum occurs at a coating index of refraction equal to 1.840.

Although both the TE and TM reflectivities are minimized by an optimum coating index that is very similar, the coating thicknesses at which this minimum occurs are different. This is shown in Fig. 8, where both the TE and the TM curves are plotted as a function of the coating thickness for a coating index of refraction of 1.840. The thickness for which the reflectivity is minimized is greater for the TE case than for the TM case. When the TE reflectivity is less than 10^{-5}, the TM reflectivity is approximately 4×10^{-3}.

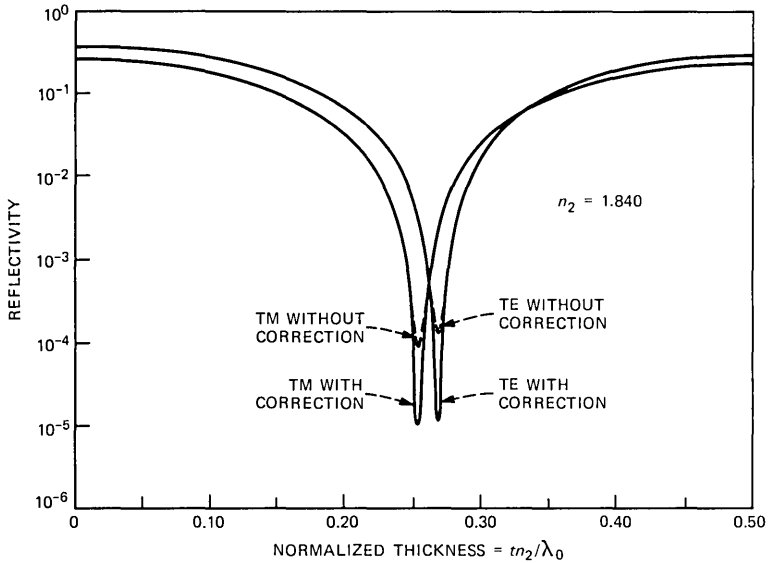

Fig. 8—Reflectivity as a function of normalized thickness for a coating index of 1.840.

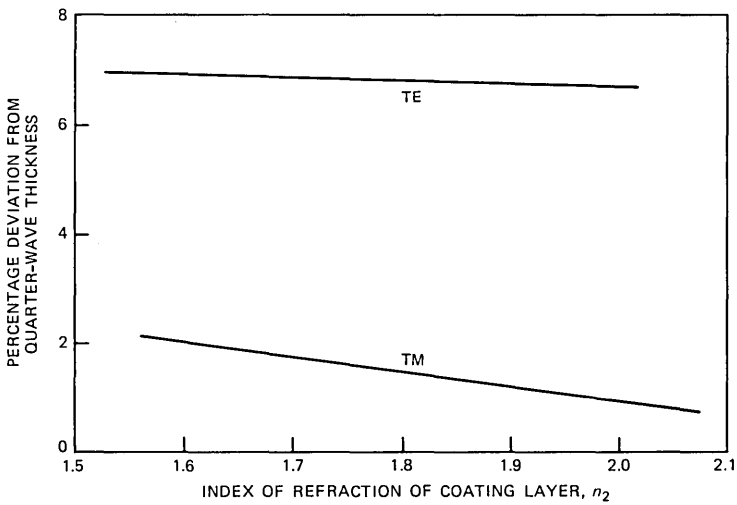

Fig. 9—Percentage deviation from quarter-wave condition of optimum normalized thickness of coating layer as a function of index of refraction of coating layer.

From Fig. 8 we learn that to maintain the reflectivity of the TE component below 10^{-4}, the film thickness must be controlled to within ±17Å; to maintain the reflectivity below 10^{-3} the film thickness must be held to ±44Å. The same conditions for the TM component correspond to ±17Å and ±53Å, respectively.

In Fig. 9 the percentage deviation of the coating (at the minimum

reflectivity) from the quarter-wave thickness is plotted as a function of the index of refraction of the coating for the TE and TM cases. Because the curves never cross, it will not be possible to simultaneously minimize both the reflectivity for the TE and the TM components at a level below $\approx 10^{-4}$. The TE deviation is approximately 7 percent over the range considered. The TM deviation varies from 2 percent to 1 percent.

The calculations can be compared with previous modal reflectivity results at $h = 0$. In agreement with these calculations,[5] the TE reflectivity is higher than the plane-wave result and the TM reflectivity is lower than the plane-wave result.

V. CONCLUSIONS

We have derived an exact solution to the coated waveguide reflectivity problem. The solution is valid for an arbitrary index variation, $n_1(x)$, of the waveguide structure.

We have observed significant deviations between the exact results and the results obtained when the index of the waveguide structure is approximated as a constant equal to the active layer index.

The range of the indices of refraction and the thickness of the coating layer to minimize either the TE or the TM reflectivity were obtained. The TE and TM reflectivities have their minima at different thicknesses. This suggests that tailoring the output polarization of light-emitting devices by controlling the coating parameters might be possible.

Also, we have outlined the procedure for calculating the parameters to minimize the optical reflectivity. A sample calculation has been given for a particular laser structure. Further work is necessary to set up general guidelines for coating parameters for the various laser structures.

VI. ACKNOWLEDGMENTS

The authors wish to express their appreciation to W. B. Joyce and to F. K. Reinhart for many helpful discussions and for critical comments on the paper.

REFERENCES

1. J. McKenna, "The Excitation of Planar Dielectric Waveguides at p-n Junctions, I," B.S.T.J., *46*, No. 7 (September 1967), pp. 1491–526.
2. F. K. Reinhart, I. Hayashi, and M. B. Panish, "Mode Reflectivity and Waveguide Properties of Double-Heterostructure Injection Lasers," J. Appl. Phys., *42* (October 1971), pp. 4466–79.
3. E. I. Gordon, "Mode Selection in GaAs Injection Lasers Resulting From Fresnel Reflection," IEEE J. Quant. Electron., *QE-9* (July 1973), pp. 772–6.
4. D. C. Krupka, "Selection of Modes Perpendicular to the Junction Plane in GaAs

Large-Cavity Double-Heterostructure Lasers," IEEE J. Quant. Electron., *QE-11* (July 1975), pp. 390–400.
5. T. Ikegami, "Reflectivity of Mode of Facet and Oscillation Mode in Double-Heterostructure Injection Lasers," IEEE J. Quant. Electron., *QE-8* (June 1972), pp. 470–6.
6. M. A. A. Pudensi and L. G. Ferreira, "Method to Calculate the Reflection and Transmission of Guided Waves," J. Opt. Soc. Am., *F2* (January 1982), pp. 126–30.
7. J. E. Kardontchik, "Mode Reflectivity of Narrow Stripe-Geometry Double Heterostructure Lasers," IEEE J. Quant. Electron., *QE-18* (August 1982), pp. 1279–86.
8. R. H. Clarke, "Theory of Reflection From Antireflection Coatings," B.S.T.J., *62* (December 1984), pp. 2885–92.
9. L. Lewin, "A Method for the Calculation of the Radiation-Pattern and Mode-Conversion Properties of a Solid-State Heterojunction Laser," IEEE Trans. Microw. Theory and Tech., *MTT-23*, No. 7 (July 1975), pp. 576–85.
10. M. Born and E. Wolfe, *Principles of Optics*, Fifth Edition, New York: Pergamon, 1975.

APPENDIX A

TE Reflectivity

We will use a bra-ket notation, $(|)$, in the following derivation for simplicity of notation. In this context a bra-ket denotes integration over the x coordinate only. Therefore, the bra-ket depends on the z coordinate. Some of the bra-kets involve integrations over products of functions defined in adjacent regions. These integrals only have meaning when evaluated at the boundary between these regions. Equation (22) is a summary of some basis states used in the calculation and some elementary integrals needed later. To further simplify the notation, the system is placed in a large box of unit volume. The integrals in the main text of the paper are derived from the sums presented in this section by allowing the volume to approach infinity. Note that in this section the continuous variable s_2 has been replaced by the discrete variable j.

The incident wave function in region 1 is

$$|\vec{\psi}) = e^{ik_1 z}\, g(x) \tag{22a}$$

$$|\overleftarrow{\psi}) = e^{-ik_1 z}\, g(x). \tag{22b}$$

Basis states in region 2 are

$$|\vec{j}) = \frac{1}{\sqrt{\lambda_2}}\, e^{ik_z^j z}\, e^{ik_x^j x},\ (k_z^2 + k_x^2 = k_2^2 = (k_0 n_2)^2),\ (k_z^j = k_z^{-j}) \tag{22c}$$

$$|\overleftarrow{j}) = \frac{1}{\sqrt{\lambda_2}}\, e^{ik_z^j z}\, e^{ik_x^j x} \tag{22d}$$

$$(\vec{j}\,|\,\overleftarrow{j}') = e^{-2ik_z^j z}\, \delta_{jj'} \tag{22e}$$

$$(\vec{j}\,|\,\vec{\psi})\,|_{z=0} = f_j \tag{22f}$$

$$(\overleftarrow{\jmath}\,|\,\overleftarrow{\psi})\,|_{z=0} = (\overleftarrow{\jmath}\,|\,\vec{\psi})\,|_{z=0} = (\overleftarrow{\jmath}\,|\,\vec{\psi})\,|_{z=0} = f_j \tag{22g}$$

$$(\overleftarrow{\psi}\,|\,\vec{\psi})\,|_{z=0} = \sum_j f_j f_j^*. \tag{22h}$$

In the above expressions $g(x)$ corresponds to the real space modal distribution and $\delta_{jj'}$ is a Kronecker delta function.

There is a one-to-one correspondence between the wave functions $\vec{\jmath}$, $\overleftarrow{\jmath}$ and the wave function $\vec{\sigma}_m$, where the wave function $\vec{\jmath}$ corresponds to a state in region 2 and $\vec{\sigma}_m$ corresponds to a state in region 3. This correspondence is due to the uniformity of the interface between regions 2 and 3. Thus we may write

$$(\vec{\jmath}\,|\,\vec{\sigma}_m)\,|_{z=t} = \delta_{mj}\alpha_m, \tag{23}$$

where α_m is a constant.

The following calculation consists of demanding continuity of the tangential components of the electric and magnetic fields at the two interfaces. The wave functions, $\vec{\psi}$, represent the electric fields. The magnetic fields may be easily obtained by using Maxwell equations. We define an operator, h_i, which multiplies the plane-wave functions in region i by the cosine of the angle between the incident k-vector and the surface normal vector. For the TE fields, in which the electric field is along the y axis, the magnetic fields can be obtained with operator h_i:

$$\overleftrightarrow{B}^j_{\tan \mathrm{TE}} \propto n_i(x)h_i\,|\,\overleftrightarrow{\jmath}) = \mp h_i^j(x)n_i(x)\,|\,\overleftrightarrow{\jmath}) \tag{24}$$

With the help of Snell's law,[10] we write for the operators

$$h_1 = \sqrt{1 - \left(\frac{n_2 s_2}{n_1}\right)^2}, \qquad s_2 = \sin\Theta_2 \quad \text{for} \quad |s_2| < 1$$

$$h_2 = \sqrt{1 - s_2^2}$$

$$h_3 = \sqrt{1 - \left(\frac{n_2 s_2}{n_3}\right)^2}. \tag{25}$$

At the surface between regions 2 and 3 the equation describing the continuity of the electric field is written

$$\sum_j [b_j\,|\,\vec{\jmath}) + d_j\,|\,\overleftarrow{\jmath})] = \sum_m c_m\,|\,\vec{\sigma}_m). \tag{26}$$

The transverse magnetic field continuity equation is written

$$\sum_j [b_j n_2 h_2^j\,|\,\vec{\jmath}) - d_j n_2 h_2^j\,|\,\overleftarrow{\jmath})] = \sum_m n_3 h_3^m c_m\,|\,\vec{\sigma}_m). \tag{27}$$

Project with $|\vec{j})$ on eqs. (26) and (27) and use eqs. (22) and (23) for substitutions to obtain

$$b_j + d_j\, e^{-2i\phi_j} = c_j \alpha_j \tag{28}$$

$$n_2 h_2^j\, [b_j - d_j\, e^{-2i\phi_j}] = n_3 h_3^j c_j \alpha_j, \tag{29}$$

where

$$\phi_j = \frac{2\pi n_2 h_2^j t}{\lambda_0}$$

and where λ_0 is the wavelength in vacuum and t is the thickness of the coating.

Equations (28) and (29) are combined to eliminate $c_j \alpha_j$,

$$d_j = b_j \frac{(n_2 h_2^j - n_3 h_3^j)}{(n_2 h_2^j + n_3 h_3^j)}\, e^{2i\phi_j} = b_j r_{23}^j\, e^{2i\phi_j}. \tag{30}$$

The equation for the continuity of the electric field on the surface of regions 1 and 2 is written

$$|\vec{\psi}) + r|\overleftarrow{\psi}) + \sum_k a_k |\overleftarrow{\phi}_k) = \sum_j [(b_j|\vec{j}) + d_j|\vec{j})]. \tag{31}$$

With the use of the identity operators $1 = \sum_j |\vec{j})(\vec{j}|$ and $1 = \sum_j |\overleftarrow{j})(\overleftarrow{j}|$, eq. (31) becomes

$$\sum_{j'} \left[f_{j'} |\vec{j}') + r f_{j'} |\overleftarrow{j}') + \sum_k a_k (\overleftarrow{j}'|\overleftarrow{\phi}_k) |\overleftarrow{j}') \right] = \sum_{j'} [b_{j'} |\vec{j}') + d_{j'} |\vec{j}']. \tag{32}$$

With the help of eq. (24), the magnetic field continuity equation is written

$$\sum_{j'} \left[h_1^{j'}(x) n_1(x) [f_{j'} |\vec{j}') - r f_{j'} |\overleftarrow{j}')] - \sum_k a_k (\overleftarrow{j}'|\overleftarrow{\phi}_k) h_1^{j'}(x) n_1(x) |\overleftarrow{j}') \right] = \sum_{j'} n_2 h_2^{j'} [b_{j'} |\vec{j}') - d_{j'} |\vec{j}')]. \tag{33}$$

We project on eqs. (32) and (33) with $|\overleftarrow{j})$ at the surface of regions 1 and 2 ($z = 0$). We must consider that since both $h_1^{j'}(x)$ and $n_1(x)$ depend on x, $(\overleftarrow{j}|h_1^{j'}(x) n_1(x)|\vec{j}') \neq h_1^{j'}(x) n_1(x) (\overleftarrow{j}|\vec{j}')$.

We obtain

$$f_j + f_j r + \sum_k a_k (\overleftarrow{j}|\overleftarrow{\phi}_k) = b_j + d_j \tag{34}$$

$$\sum_{j'} \left(f_{j'} - f_{j'} r - \sum_k a_k (\overleftarrow{J}' \,|\, \overleftarrow{\phi}_k) \right) (\overleftarrow{J} \,|\, h_1^{j'}(x) n_1(x) \,|\, \overleftarrow{J}') = n_2 h_2^j (b_j - d_j). \quad (35)$$

We now rewrite the product $n_1(x)h_1^j(x)$ as discussed in the main text,

$$n_1(x)h_1^j(x) = n_1^0 h_1^0 + \Delta H_j, \quad (36)$$

where

$$h_1^0 = \sqrt{1 - \left(\frac{n_2 s_2}{n_1^0}\right)^2}$$

and combine eqs. (34) and (35) to obtain

$$f_j[r_{12}^j + 1] + \frac{\Delta_j}{(n_1 h_1^j + n_2 h_2^j)} = b_j[1 + r_{12}^j \, r_{23}^j \, e^{2i\phi_j}], \quad (37)$$

where r_{12}^j and r_{23}^j are the plane boundary Fresnel reflection coefficients and

$$\Delta_j = \sum_{j'} \left[f_{j'} - f_{j'} r - \sum_k a_k (\overleftarrow{J}' \,|\, \overleftarrow{\phi}_k) \right] (\overrightarrow{J} \,|\, \Delta H_{j'} \,|\, \overrightarrow{J}') \,|_{z=0}. \quad (38)$$

To calculate r we project $|\overleftarrow{\psi})$ on eq. (31) at $z = 0$ and use the fact that $|\overleftarrow{\psi})$ is orthogonal to $|\overleftarrow{\phi}_k)$ to obtain

$$r = \sum_j f_j^* (b_j + d_j - f_j). \quad (39)$$

If we use eq. (30) to substitute for d_j, eq. (37) to substitute for b_j, and eq. (5) to define R_j we obtain eq. (1), the desired result. The last step in the calculation requires that the box dimensions approach infinity so that the sum tends to an integral.

The expansion for Δ_j is obtained by equating like terms in eqs. (1) and (39), and using eq. (34) to replace $b_j + d_j - f_j$. We obtain

$$f_j r + \sum_k a_k (\overleftarrow{J} \,|\, \overleftarrow{\phi}_k) = f_j R_j + \Delta_j \frac{[R_j + 1]}{2 n_1^0 h_1^0}. \quad (40)$$

If (40) is substituted into (38), we obtain eqs. (2) and (3).

APPENDIX B

TM Reflectivity

The TM field is analyzed in close analogy to the TE field. In this case the magnetic field is along the y axis. The operator, h_i, is useful

to determine, for a given angle Θ, the tangential component of the electric field vector. To obtain the magnetic field, the wave function is multiplied by the index of refraction. With these considerations the two equations representing continuity at the surface of regions 2 and 3, after projecting on $|\tilde{\jmath})$, are written

$$n_2(\tilde{b}_j + \tilde{d}_j e^{-2i\phi_j}) = n_3 \tilde{c}_j \tilde{\alpha}_j \tag{41}$$

$$h_2^j(\tilde{b}_j - \tilde{d}_j e^{-2i\phi_j}) = h_3^j \tilde{c}_j \tilde{\alpha}_j. \tag{42}$$

Combining eqs. (41) and (42) to eliminate $\tilde{\alpha}_j \tilde{c}_j$, we obtain

$$\tilde{d}_j = \tilde{b}_j \frac{(n_3 h_2^j - n_2 h_3^j)}{(n_3 h_2^j + n_2 h_3^j)} e^{2i\phi_j} = \tilde{b}_j \tilde{r}_{23} e^{2i\phi_j}. \tag{43}$$

The conditions for continuity of the electric field and magnetic field at the surface between regions 1 and 2 are written

$$h_1 |\vec{\tilde{\psi}}) + h_1 r |\overleftarrow{\tilde{\psi}}) + \sum_k h_1 \tilde{a}_k |\overleftarrow{\tilde{\phi}}_k) = h_2 \left[\sum_j \tilde{b}_j |\tilde{\jmath}) + \tilde{d}_j |\tilde{\jmath}) \right] \tag{44}$$

$$n_1(x) \left[|\vec{\tilde{\psi}}) + r |\overleftarrow{\tilde{\psi}}) + \sum_k \tilde{a}_k |\overleftarrow{\tilde{\phi}}_k) \right] = n_2 \left[\sum_j (\tilde{b}_j |\tilde{\jmath}) + \tilde{d}_j |\tilde{\jmath})) \right]. \tag{45}$$

After using the identity operator, projecting on $|\tilde{\jmath})$, and using the fact that at $z = 0$ $(\tilde{\jmath}|n_1(x)|\tilde{\jmath}') = (\tilde{\jmath}|n_1(x)|\tilde{\jmath}')$ and $(\tilde{\jmath}|h_1^j(x)|\tilde{\jmath}') = -(\tilde{\jmath}|h_1^j(x)|\tilde{\jmath}')$ [see eq. (24)], we get

$$h_1^0 \tilde{f}_j - \tilde{r} h_1^0 \tilde{f}_j - h_1^0 \sum_k \tilde{a}_k (\tilde{\jmath}|\overleftarrow{\tilde{\phi}}_k) + \tilde{\Delta}_j^A = h_2^j(\tilde{b}_j - \tilde{d}_j) \tag{46}$$

and

$$n_1^0 \tilde{f}_j - n_1^0 \tilde{r} \tilde{f}_j + n_1^0 \sum_k \tilde{a}_k (\tilde{\jmath}|\overleftarrow{\tilde{\phi}}_k) + \tilde{\Delta}_j^B = n_2(\tilde{b}_j + \tilde{d}_j), \tag{47}$$

where

$$\tilde{\Delta}_j^A = \sum_{j'} (\tilde{f}_{j'} - \tilde{r} \tilde{f}_{j'} - \sum_k \tilde{a}_k (\tilde{\jmath}'|\overleftarrow{\tilde{\phi}}_k))(\tilde{\jmath}|h_1^j(x) - h_1^0|\tilde{\jmath}') \tag{48}$$

and

$$\tilde{\Delta}_j^B = \sum_{j'} (\tilde{f}_{j'} + \tilde{r} \tilde{f}_{j'} + \sum_k \tilde{a}_k (\tilde{\jmath}|\Delta n(x)|\tilde{\jmath}'). \tag{49}$$

Combine eqs. (46) and (47) by multiplying (46) by n_1^0 and (47) by h_1^0 and then adding them together. Use the fact that

$$\tilde{r}_{12} = \frac{n_2 h_1 - n_1 h_2}{n_2 h_1 + n_1 h_2}$$

to get

$$\tilde{b}_j = \frac{\dfrac{n_1^0}{2n_2}\,[1 + \tilde{r}_{12}^j]\left[2\tilde{f}_j + \dfrac{\tilde{\Delta}_j^A}{h_1^0} + \dfrac{\tilde{\Delta}_j^B}{n_1^0}\right]}{[1 + \tilde{r}_{12}^j \tilde{r}_{23}^j e^{2i\phi_j}]}. \tag{50}$$

The reflection coefficient is then derived by dividing eq. (45) by $n_1(x)$ and then projecting on $|\overleftarrow{\tilde{\psi}})$, so that

$$(\overleftarrow{\tilde{\psi}}|\overrightarrow{\tilde{\psi}}) + \tilde{r} = n_2 \sum_j \left(\overleftarrow{\tilde{\psi}}\left|\frac{1}{n_1(x)}\right|\overrightarrow{\tilde{J}}\right)(\tilde{b}_j + \tilde{d}_j). \tag{51}$$

Expand $1/n_1(x)$ as

$$\frac{1}{n_1(x)} = \frac{1}{n_1^0} + \frac{1}{n_1^0}\left[\frac{n_1^0}{n_1(x)} - 1\right] \tag{52a}$$

$$= \frac{1}{n_1^0}\,[1 + \Delta D(x)]. \tag{52b}$$

We then define

$$\Delta\tilde{D}_{jj'} = \left(\overrightarrow{\tilde{J}}'\left|\frac{n_1^0}{n_1(x)} - 1\right|\overrightarrow{\tilde{J}}\right) \tag{52c}$$

and combine eqs. (51) with (52) to obtain

$$\sum_j \tilde{f}_j^* \tilde{f}_j + \tilde{r} = \frac{n_2}{n_1^0}\sum_j \left[\tilde{f}_j^* + \sum_{j'} \Delta\tilde{D}_{jj'}\tilde{f}_{j'}^*\right]\tilde{b}_j(1 + \tilde{r}_{23}e^{2i\phi_j}). \tag{53}$$

Now substitute (50) for b_j to yield an expression for the reflection coefficient:

$$\tilde{r} = \sum_j \tilde{f}_j^* \tilde{f}_j \tilde{R}_j + \sum_j \tilde{f}_j^*\,[1 + \tilde{R}_j]\left[\tilde{f}_j^* + \sum_j \Delta\tilde{D}_{jj'}\tilde{f}_{j'}^*\right]\left[\frac{\tilde{\Delta}_j^A}{2h_1^{j0}} + \frac{\tilde{\Delta}_j^B}{2n_1^0}\right]$$
$$+ \sum_j \left[\sum_{j'} \Delta\tilde{D}_{jj'}\tilde{f}_{j'}^*\right][1 + \tilde{R}_j]\tilde{f}_j. \tag{54}$$

We must now form a series expansion for $\tilde{\Delta}_j^A$ and $\tilde{\Delta}_j^B$.

Combining eqs. (47) and (43) and (50) we get

$$\tilde{r}\tilde{f}_j + \sum_k \tilde{a}_k(\overrightarrow{\tilde{J}}|\overleftarrow{\tilde{\phi}}_k) = \tilde{R}_j\,\tilde{f}_j + [1 + \tilde{R}_j]\,\frac{\tilde{\Delta}_j^A}{2h_1^{j0}} - [1 - \tilde{R}_j]\,\frac{\tilde{\Delta}^B}{2n_1^0}. \tag{55}$$

Equation (55) is now plugged into (48) and (49) to obtain eqs. (12) through (15).

AUTHORS

Peter P. Deimel, Dipl. Phys. (Physics), 1974, Technical University in Munich; Ph.D. (Physics), 1980, University of Oregon; AT&T Bell Laboratories, 1980—. Mr. Deimel's initial work involved coupling semiconductor lasers to a grating and wavelength tuning. His recent work involves integral lens calculations, and he is currently working on problems in monolithic integrated optoelectronics.

Daniel R. Kaplan, B.S. (Physics), 1977, State University of New York at Albany; M.A. (Physics), 1979, Ph.D. (Physics), 1981, Princeton University; Institute for the Study of Defects in Solids (I.S.D.S.), Albany, 1976; Brookhaven National Laboratories, Physics Department, Summer 1978 and Summer 1979; AT&T Bell Laboratories, 1979—. At I.S.D.S. Mr. Kaplan worked on Extended Huckel Theory Calculations of impurities in silicon and on RBS measurements of impurity diffusion in silicon. At Brookhaven Labs he worked on RBS analysis and nuclear reaction analysis of the diffusion of oxygen in alumina. His doctoral work, performed while at AT&T Bell Laboratories from 1979 to 1981, consisted of measurements of inelastic scattering from X-ray standing waves. Since 1981 he has been involved in lightwave communications, and his current work is in monolothic integrated optoelectronics.

AT&T Bell Laboratories Technical Journal
Vol. 63, No. 6, July–August 1984
Printed in U.S.A.

The LT-1 Connector Family of Transmultiplexers

By G. W. BLEISCH,* W. J. MITCHELL,* and S. DODDS*

(Manuscript received June 17, 1983)

The LT-1 family of transmultiplexers was designed to provide a flexible and economical means of interconnecting the widely deployed long-haul analog transmission plant with the emerging network of digital switches and facilities. The LT-1 connector eliminates redundant interfaces and uses custom integrated circuits. The most significant improvement is in the analog signaling circuits—the function of an entire circuit pack is reduced to circuitry occupying less than 2 square inches. Reuse of circuits designed for other systems under development helped to introduce this technology rapidly. The original design, targeted for the *4ESS*™ market, was enhanced with three additional designs, which expanded the signaling capability to include special services, added a digital echo canceler for satellite applications, and provided compatibility with international signaling.

I. INTRODUCTION

In 1976 the first digital toll switching office *4ESS*† switch was placed into service in the Bell System and plans were finalized to develop the LT-1 connector. It was clear that in the decade ahead, most of the vast network of analog toll trunks would need a digital signal format at the switching system interface. This was the primary motivation for developing the LT-1 connector—to economically terminate analog trunks on a time division, digital switching machine. This equipment is referred to generically as a transmultiplexer.

---

* AT&T Bell Laboratories.
† Trademark of AT&T Technologies, Inc.

Copyright © 1984 AT&T. Photo reproduction for noncommercial use is permitted without payment of royalty provided that each reproduction is done without alteration and that the Journal reference and copyright notice are included on the first page. The title and abstract, but no other portions, of this paper may be copied or distributed royalty free by computer-based and other information-service systems without further permission. Permission to reproduce or republish any other portion of this paper must be obtained from the Editor.

II. LONG-HAUL TOLL NETWORK

Plans for deploying the LT-1 connector were closely linked to the *4ESS* cutover program. At the outset it was clear that even with expedited development and manufacture, initial shipment would not be possible before the year 1979; *4ESS* installation schedules indicated that actual service on the equipment could be achieved in 1980. In the 5 years (1979 through 1984), plans called for retiring about 120 electromechanical 4A toll switches, and replacing them with about 90 digital *4ESS* switches. Figure 1 illustrates an estimate of analog trunk needs in the LT-1 connector availability time frame. This estimate indicated a program to deploy 900 frames of LT-1 connectors providing 432,000 analog trunk terminations each year. By 1985 all but 14 percent of these analog trunks will be switched by digital *4ESS* machines; over 83 percent of the analog trunks will be terminated with transmultiplexer equipment.

The intertoll transmission facilities are predominately analog and include coaxial cable, FM radio, and, most recently, single-sideband AM radio. This situation is not expected to change until the advent of long-haul optical fiber and digital radio transmission systems in the late 1980's.

Toll-connect transmission facilities also incorporate significant amounts of analog, as well as digital, equipment. The division is about equal; the current, modest analog majority is expected to change to a modest digital majority by the mid-1980's.

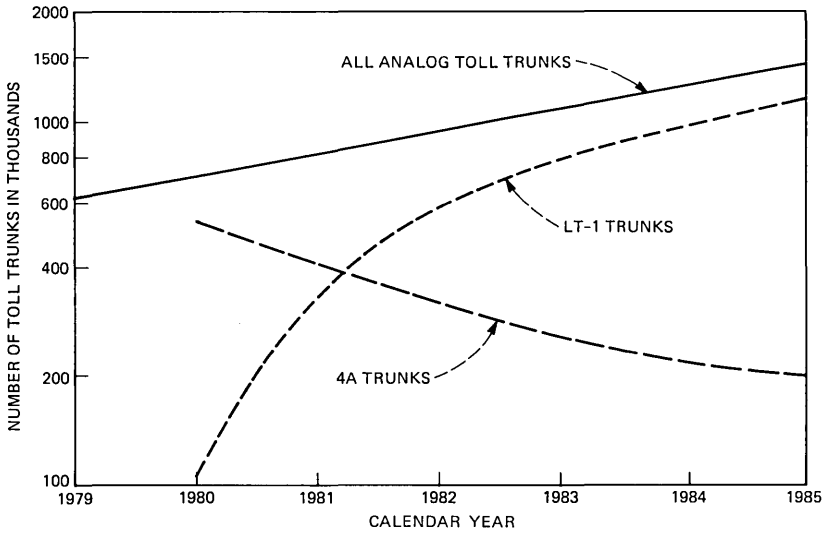

Fig. 1—Long-haul, toll network, analog trunk estimate.

III. OTHER APPLICATIONS

Another application of the LT-1 connector is the more general interconnection of digital, T-carrier transmission facilities with analog, L-type facilities. When this potential application was surveyed, the telephone operating companies indicated fairly limited needs (estimated to be less than 10 percent of *4ESS* switch analog trunk termination applications). It was thus decided to defer the facility interconnect development (LT-1B) and concentrate on making the *4ESS* switch version available as soon as possible. Also, the need to accommodate many signaling types in the facility interconnect applications made possible a less costly version, tailored to the less stringent signaling requirements of the *4ESS* switch application.

The digital access and cross-connect system (DACS) has considerably changed the facility interconnect application. DACS "grooms" digital facilities by collecting individual special-service channels from a number of different digital systems and routing them to the special office equipment required to operate and maintain them. Similarly, the individual channels can be distributed to many different digital systems to reach the end customers. The LT-1B facility connector, in combination with DACS, will collect and distribute special-service channels, utilizing analog transmission facilities in a similar manner.

IV. DESIGN PHILOSOPHY

Two design techniques were originally investigated. The first approach was to merge the block diagrams of the individual systems—frequency division multiplexing (FDM), single frequency signaling, and digital pulse code modulation (PCM)—into a single diagram. Immediately, it was clear that much of the interface circuitry in an integrated terminal was redundant, consisting primarily of magnetic components used to isolate the circuit packs from the outside world. Also, standard interfaces for signaling and transmission were unnecessary for this application.

Once these standard interfaces and the interface circuitry were removed, up-to-date integrated circuit techniques would be applied to the remaining circuits. The result was a compact modern design that was within the bounds of existing manufacturing technology. Figure 2 shows the block diagram.

The 12-channel analog FDM signal is buffered and distributed on a low-impedance bus to the 12 channel units. On the channel unit, the 4-kHz band of interest is selected by a crystal bandpass filter and demodulated to voice frequency (VF). Any signaling information present is detected and sent to the digital transmit unit in the form of a digital logic signal. The voice signal is then sampled at 8 kHz, and the

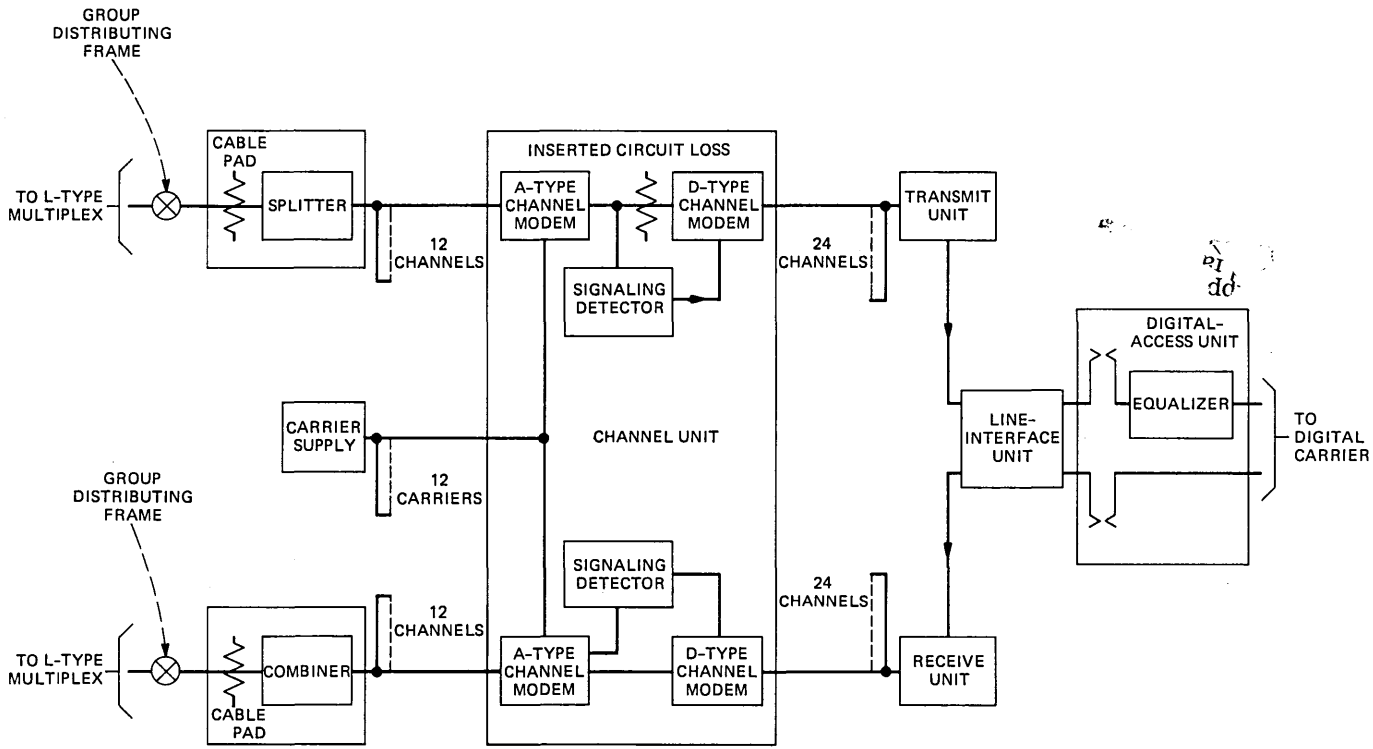

Fig. 2—LT-1 connector.

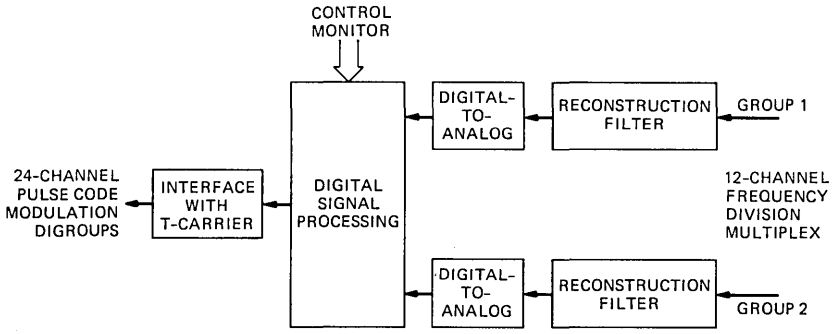

Fig. 3—All-digital transmultiplexer.

samples are time-division-multiplexed on a pulse amplitude modulation (PAM) bus with 23 other channels. These samples are encoded, along with the signaling information, into the standard 24-channel DS-1 signal. The other direction of transmission inverts this process.

Also, some of the circuits are identical to those used in two recently completed developments—D4 and N4. This reduces manufacturing needs and training requirements for the operating companies.

The second approach considered was an all-digital design. Very simply, it would convert the analog group signal into a digitized version with a high-precision, high-speed, analog-to-digital (A/D) converter and perform the demodulation, signal detection, and time division multiplexing functions entirely with digital hardware. It could time-share the circuitry over a large number of channels and thus achieve the well-known benefits of digital circuitry. Figure 3 shows a simplified block diagram of the terminal.

Selecting the approach for final development required an estimate of the cost, size, and power consumption of each design, as well as an estimate of the development time and risk. The results of the study with the per-channel parameters normalized to one are shown in Table I. To the authors' knowledge, this is the first time in which such a study has shown that an all-digital version of what is essentially an analog transmission function could be cost-competitive with a modern per-channel design. We believe this is caused by two factors. The first factor is the degree of complexity possible with very large-scale integrated (VLSI) devices; tens of thousands of switching elements can be integrated into a single device. The second reason is inherent in the transmultiplexer itself in that an A/D conversion need be performed only in one direction of transmission. The fact that the cost estimate for an all-digital transmultiplexer was comparable to the per-channel design suggests that continued development in this area is warranted, and further, it seems likely that an all-digital design soon will become

Table I—Transmultiplexer parameter comparison

	Per Channel	Digital
Cost	1.0	1.0
Size	1.0	0.5
Power	1.0	2.0

more economical than the per-channel design. However, the all-digital design was considered to have significantly greater risk and a longer design interval than the per-channel approach. The cutover of a *4ESS* office is planned several years in advance, and the unavailability of a significant amount of terminal equipment could jeopardize the service date. This would result in a large amount of capital not being used productively. Therefore, it was decided to proceed with the per-channel transmultiplexer for final development and, at the same time, continue, on an exploratory basis, the all-digital transmultiplexer.

As we stated earlier, LT-1 initially was used to terminate analog trunks on the *4ESS* switch. In the beginning, two types of circuit designs were made available—the common channel interoffice signaling (CCIS) channel unit, and E and M channel unit. Both channel units share identical transmission circuits. The difference between them is that the E and M channel unit has additional circuits to detect the 2600-Hz signaling tone and map it into the robbed eighth-bit signaling format used in the DS-1 signal.

V. CHANNEL-UNIT DESCRIPTION

Figure 4 shows that the channel unit performs three separate functions: analog modulation, signal conversion, and digital sampling. On the analog side, the channel unit must interface with a broadband FDM signal that contains twelve voice channels in a basic group. These must be converted to voice frequency. Signaling information, if present, must then be extracted and the VF signal must be sampled and applied to the PAM bus to interface with the digital common circuits. These three functions are described in the following paragraphs.

VI. ANALOG MODULATOR

A single custom integrated circuit performed the analog modulation functions. This circuit had been thoroughly characterized previously when it was used in LMX-3 and N4. In this circuit the signal voltage is converted into a current and applied to a pair of emitter-coupled pairs. These are switched on and off under the control of the carrier. The switching effectively multiplies the signal by plus and minus one and performs the modulation process. Because of the balanced nature

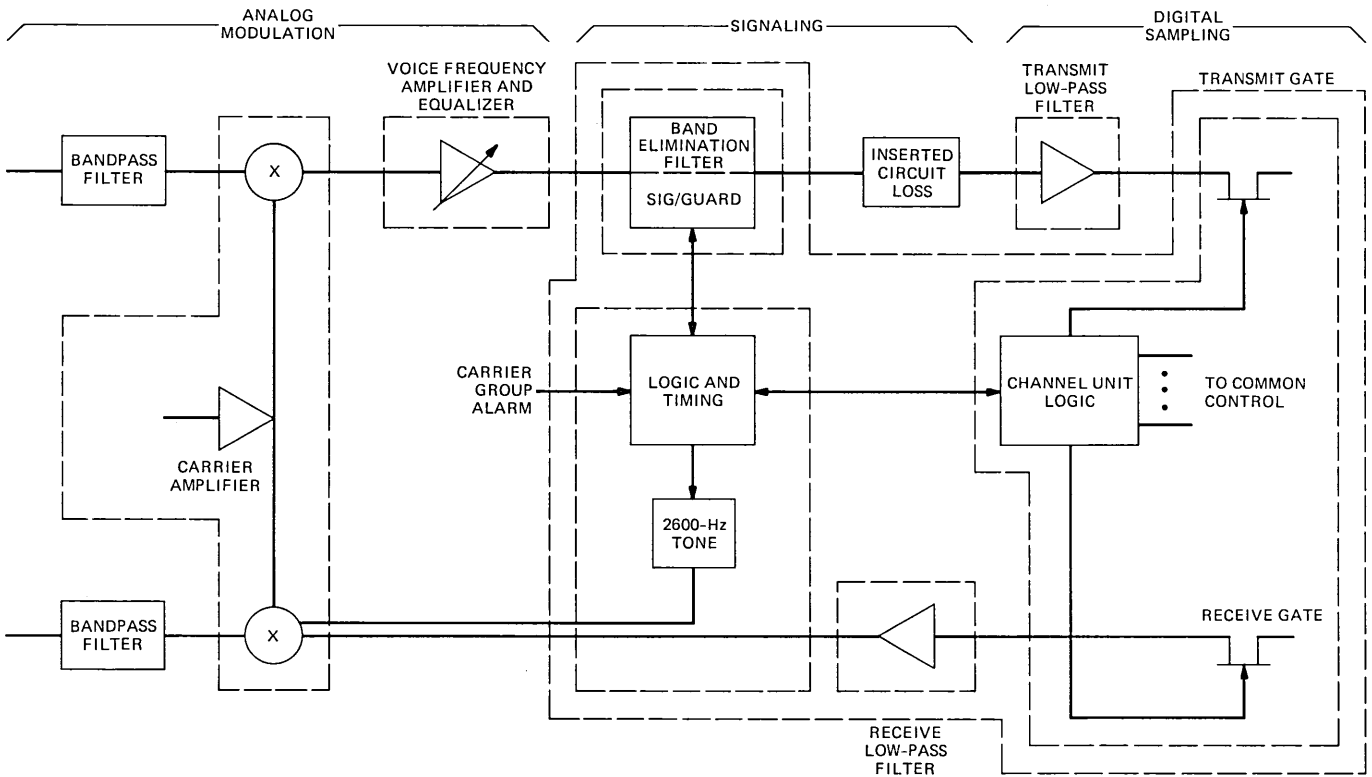

Fig. 4—LT-1 channel unit.

of the circuit, the VF signal and the 2600-Hz signal are effectively summed at the same time. The double-sideband output of the modulation process is filtered with a discrete crystal filter, which selects the lower sideband.

The reverse of this process occurs in the opposite direction. The broadband analog signal is applied to a crystal filter, which selects one channel, and the modulator circuit converts it to VF. Equalization to compensate for low frequency rolloff is provided, as well as a variable gain adjustment to compensate for amplitude misalignment in the analog facility.

VII. DIGITAL SAMPLER

The next step in the process is to convert the VF signal into PAM samples. This is accomplished with a standard D4 high-pass active filter and junction field-effect transistor (JFET) sampler. The sampler timing is controlled by a channel counter that interleaves the samples from 23 other channel units to create the complete PAM bus signal.

In the reverse direction, a second JFET gates in the appropriate sample from the receive PAM bus, also under the control of the channel counter. This sample is then filtered in a low-pass filter to reconstruct it into a continuous waveform and applied to the modulator. These circuits were designed to be compatible with the common circuits used in D4 so that the latter could be used interchangeably in an office that has both LT-1 and D4.

VIII. SIGNALING

Figure 5 shows a block diagram of the functions in the signaling receiver. The requirement is to distinguish between the presence of the true 2600-Hz signaling tone and talker energy, which may have frequency components around 2600 Hz. To accomplish this, the signal is processed by two active filters. Since one has a transmission peak at 2600 Hz (SIG) and one has a null (GUARD), the relative amount of energy from the two filters determines if the input is a pure 2600-Hz signal or if it contains significant energy at other frequencies. Because the circuit has short time constants so it can respond to pulse inputs in a few milliseconds, the output of the comparator, EN, must be further processed by pulse-correcting circuits before being transmitted to the digital circuitry.

During certain high noise conditions, such as those that occur during radio fades, the amount of energy detected by the guard amplifier can simulate talker conditions. If no other action was taken, it would appear that a trunk seizure had occurred. Since this would happen on all trunks simultaneously, the switching machine could become over-

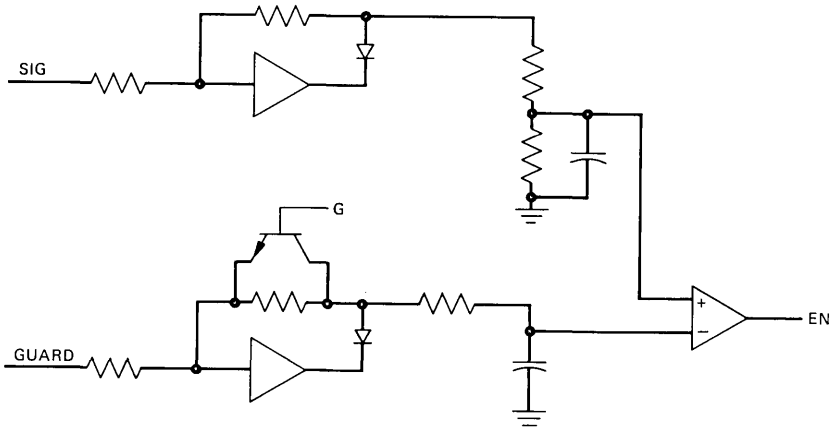

Fig. 5—Signal receiver.

loaded. To prevent this, the gain of the guard amplifier is reduced after 185 ms of being in the idle state.

Figure 6 shows a simplified block diagram of the signal transmitter. When the 2600-Hz signal is first transmitted, it is applied at a −8 dBm0 level, the high level. Because the continuous application of that much power in every channel exceeds the power level that the analog facility was designed to carry, the power is reduced to −20 dBm0 after 400 ms. In Fig. 6, the buffers convert the unregulated transistor-transistor logic (TTL) signals 2600H (high) and 2600HL (high-low) into controlled amplitude square waves. Generating none, one, or two of these signals and summing them produces tone off, low tone, or high tone. This output is added to the VF signal and modulated to the group band.

The balance of the signaling circuitry, which consists of seven timers, is shown in Fig. 7. The timers perform pulse correction in both directions, M lead correct and E lead correct; control the amplitude of the tone (HI-LO); enable an active filter to remove the received tone (BAND ELIMINATION FILTER TIMER); control the gain of the guard amplifier (G TIMER); and disable the transmission path during signaling activity (CUT A, CUT B). These seven timers are all implemented on two custom digital integrated circuits.

Because the LT-1 architecture does not require standard interface points for VF and signaling, the entire signaling function can be accomplished with these three chips mounted on a hybrid integrated circuit, along with an active filter and a few discrete components. Before LT-1 was developed, signaling required an entire printed wiring board. Further, since the timers are all digital, no problems exist with aging or component drift.

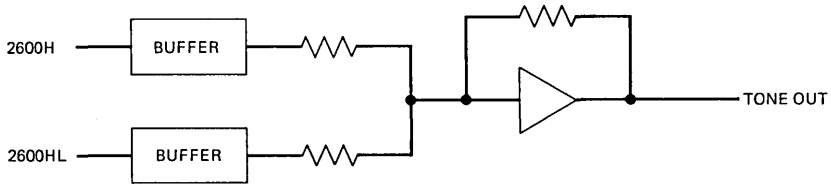

Fig. 6—Signal transmitter.

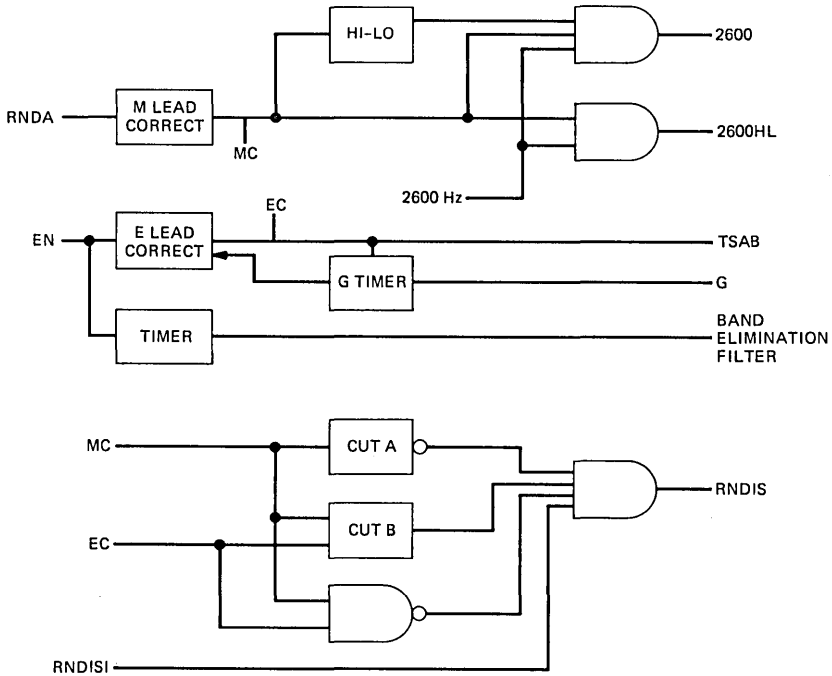

Fig. 7—Signaling control.

These two types of channel units are sufficient for all 4*ESS* switch trunks since only E and M, or CCIS signaling is used in that machine.

After the CCIS and E and M channel units were introduced, a different CCIS channel unit equipped with an echo canceler was developed. Echo canceling is implemented by a VLSI chip[1] that can generate an approximation of the echo introduced at the 2- to 4-wire points in the transmission path. The echo canceler was first used in LT-1 on satellite circuits. As is well known, the subjective annoyance of echo increases with delay. The round-trip delay through a geostationary satellite is approximately 600 ms. Long-distance connections whose echo performance would have been satisfactory on terrestrial circuits became unsatisfactory on a satellite. Further, echo suppres-

sors, traditionally used on long terrestrial circuits, are unsatisfactory on domestic satellite circuits. The echo canceler has been shown to provide a grade of service on a satellite that is equivalent to terrestrial circuits.

LT-1 is a natural point in the transmission path to place an echo canceler because it is located at the termination of an analog trunk on the switching machine. Further, since the VLSI echo canceler was implemented as a digital device, the canceler will interface with the digital signals already present in LT-1. Figure 8 shows the initial LT-1 transmission path. The receive unit converts the PCM to PAM and distributes it to the channel unit. Similarly, the transmit unit converts the PAM samples from the channel unit to PCM. Figure 9 shows how the echo-canceler unit operates. In the digital transmitting direction, the same PAM-to-PCM conversion occurs, but the PCM is sent back to the channel unit for echo canceling. In the receiving direction, the digital-to-analog (D/A) converter is not used. Rather, the received PCM is sent directly to the echo canceler as a digital signal. Having access to both directions of transmission allows the canceler to make an approximation to the echo path and thereby cancel the echo. The output of the canceler is a digital signal, which must be converted to VF by a per-channel decoder. The analog portion of the terminal is unchanged.

IX. COMMON UNITS

The line interface, transmit, and receive units are unchanged D4 units. The alarm control units (there are two versions) use the D4 alarm control unit layout but with features not needed for LT-1 deleted to reduce their cost. The version used depends upon whether LT-1 is located in the same office as the 4*ESS* switch or in another office with connection to the 4*ESS* switch provided by a T1 line.

The D4 line build-out circuit was incorporated into the LT-1 digital access units, of which there are two versions. These units provided the access points for testing and aligning the digital access time-slot selector (DATS). One of the versions provides a looping point, so that the 4*ESS* switch could be looped back on itself prior to LT-1 being put into service. Which digital access unit is selected depends upon whether the 4*ESS* switch is to be looped at the LT-1 or at a DSX-1 cross-connect frame located in the circuit between the LT-1 and the 4*ESS* switch.

The combine-and-split unit provides low-impedance summing and driving points for the 12 channel filters. Finally, a power unit provides ±12V and +5V power to all plug-ins in a double digroup. With the development of the echo canceler, an echo-canceler timing unit has

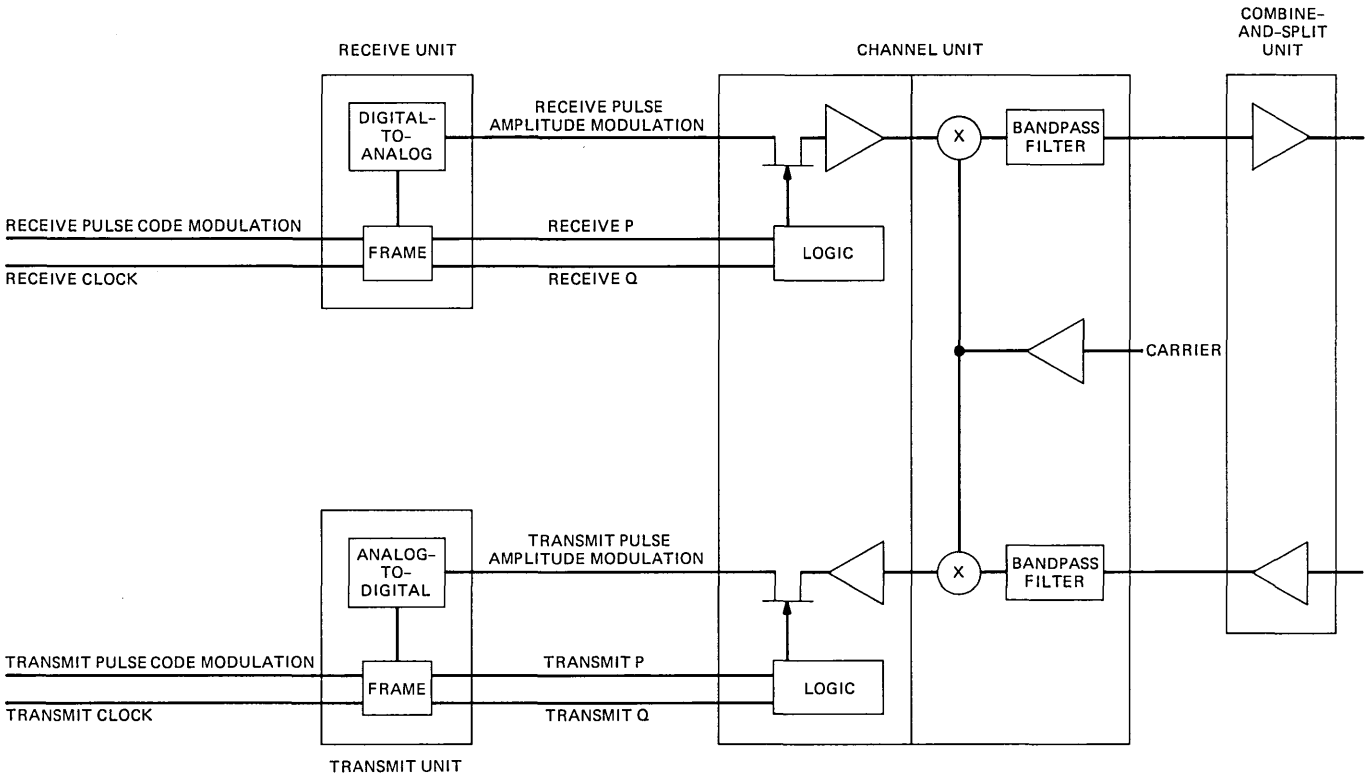

Fig. 8—Existing LT-1 connector.

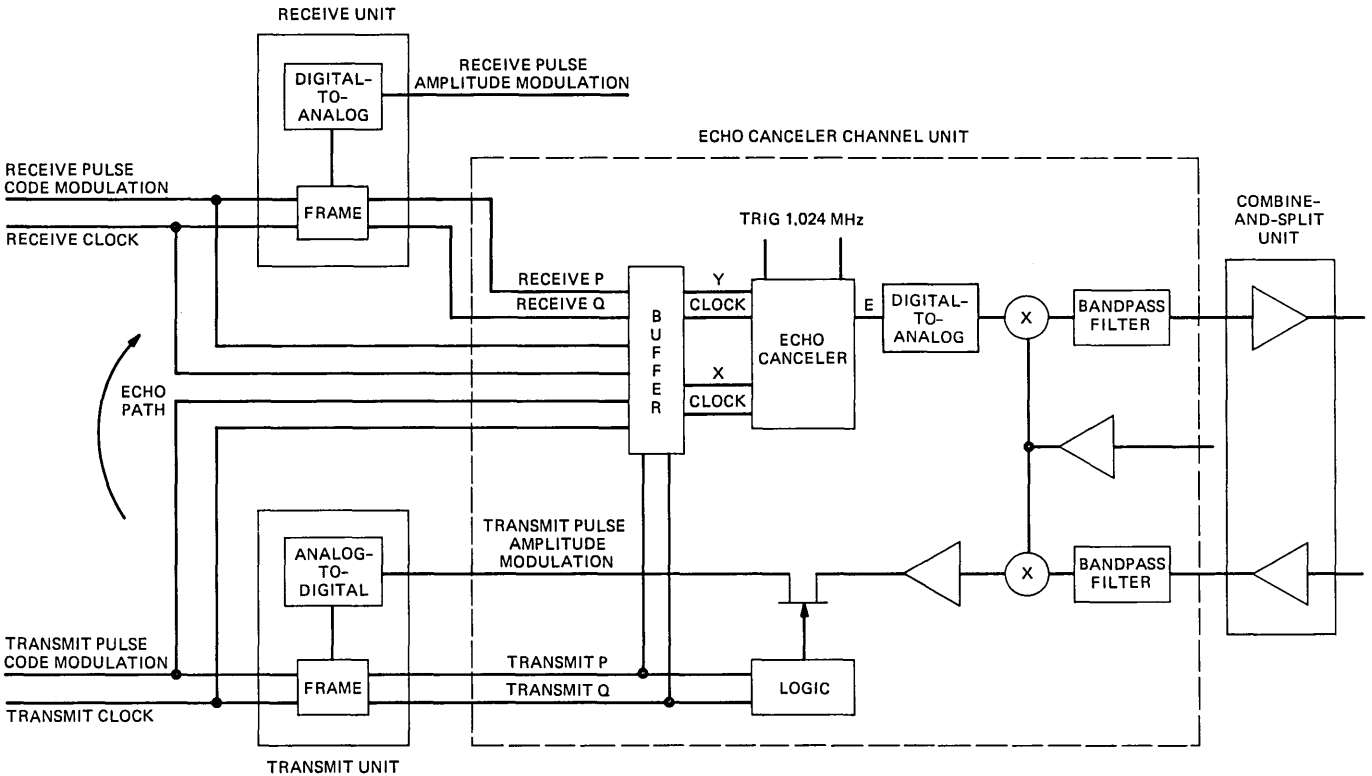

Fig. 9—LT-1 connector with echo canceler.

been added. Also, a new power unit, with additional +5V power capability needed to drive the echo cancelers, has been designed. It is interchangeable with the original unit.

These various units, together with the equipment shelves, are the major components of the LT-1 double bay frame.

X. MAINTENANCE CONSIDERATIONS

An integral part of the design for the *4ESS* switch was a plan for installing and maintaining the LT-1. Existing equipments used the switched maintenance access system (SMAS) to enable VF testing to be done on various trunks from a remote test position. Since LT-1 has no VF access, a new testing method was needed. DATS filled this need.[2] The DATS is essentially a portable D4 channel bank under microprocessor control. It can address any two of the 24 channels (one for use as an order wire, the other for test) and measure the VF power or frequency or the state of the signaling bits. It can generate a set of tones at three frequencies and four levels from information stored in a read-only memory (ROM). In addition, it can interface with any VF equipment and digitally encode external test signals or convert the digital signal on any channel into the equivalent VF signal so that it can be measured by using standard test equipment. This capability gives the DATS several advantages. First, since it is measuring and generating digital information, there is no error in the measurements caused by circuit misalignment beyond the measurement point. Second, since the DATS is microprocessor-controlled, macro programs that very quickly do repetitive tasks characteristic of trunk lineup procedures can be, and indeed have been, written.

XI. FACILITY CONNECTOR

After the LT-1 design for *4ESS* switch applications was completed, the more general problem of a facility connector, to be designated LT-1B, was investigated. Here the purpose was to connect two 12-channel group signals to a 24-channel digital signal independent of trunk type or orientation. The differences in requirements were primarily related to signaling. The types of signaling units currently in production were studied to find any commonality in the way they represent trunk conditions in the analog and digital signaling domains. The results indicated that a great deal of commonality exists, while the differences between the various units are typically in the interface circuitry, e.g., two wire or four wire, rather than in the mapping of 2600 Hz into the A and B signaling bits. It follows that for LT-1B, a single design could handle all of the 2-state signaling. The 3-state design is more complex. Here a 20-Hz modulation is placed on the 2600-Hz tone to indicate

the third state. A channel unit must be able to detect or generate the modulation, depending upon the orientation of the analog and digital sides of the transmultiplexer relative to the switching office. Finally, a fourth type of channel unit without a signaling circuit was developed for CCIS applications.

With 4 signaling types and 12 channel filters, it was obvious that the signaling circuits should be placed on a small module that could be plugged into the main channel unit. This would give complete flexibility to the operating company planners and simplify sparing.

In addition to the enhanced signaling capability, LT-1B provides features not required in LT-1.

1. The channel counting sequence in each digroup can be made compatible with D1D, D2, or D3/D4 channel banks in the field.
2. The transmitting clock can be locked to either incoming digroup or it can run free.
3. The digital side can operate in mode 2 (DS-1C) or mode 3 (two DS-1s).
4. An optional 2-way carrier failure alarm (CFA) with trunk processing can be provided.

This last feature is necessary to allow arbitrary routing of the analog groups. Consider the arrangement shown in Fig. 10. A short-haul, 24-channel digital DS-1 signal from Lawrence, MA is converted, by an LT-1B in Boston, into two long-haul analog groups that terminate in different cities, Cleveland and Chicago. If a failure occurs on the digital digroup, the normal red and yellow alarms will be propagated and trunk processing will occur at the Lawrence, MA end. The LT-1B will remove the outgoing CFA pilot, and the channel banks in Cleveland and Chicago will be processed. However, if a failure occurs on one of the analog trunk groups, it cannot be propagated to the digital banks without all 24 trunks being taken out of service. Therefore, supervisory trunk processing is performed by the LT-1B only on the 12 trunks affected by the failure. This allows service to continue on the other group.

To accommodate the various kinds of signaling, three trunk processing options may be selected on a per-channel basis:

1. On-hook for 2.5s followed by off-hook
2. On-hook
3. Off-hook.

The purpose of these three options is to terminate billing when a failure occurs on any calls in progress and to prevent false ringing or other similar problems on special-service lines.

A particularly important application for LT-1B is its use, in conjunction with DACS, to groom analog facilities. The DACS, which was introduced in 1981, performs a time-slot interchange function, similar

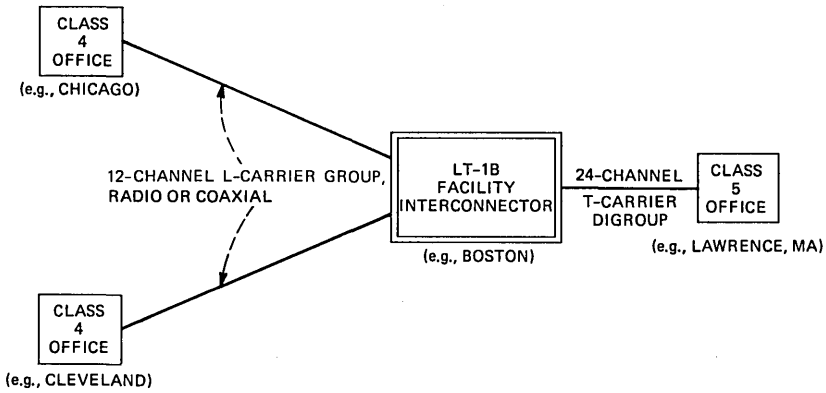

Fig. 10—LT-1 facility connector end-office trunking.

to that of the 4*ESS* switch. Its role in the network is to separate switched message and special services on T1 lines. The combination of LT-1B and DACS will allow the same type of network flexibility in the analog plant.

XII. THE LT-1E CONNECTOR

Another variation in the basic LT-1 design is compatible with International Telegraph and Telephone Consultative Committee (CCITT) transmission and signaling on the analog side and the standard North American DS-1 on the digital side.

The LT-1E connector is the CCITT version of LT-1. It required new carrier supply units, a new channel unit, and a new combine and split unit. The channel unit was a combination of CCITT analog modem and D4 circuits. The analog circuit used 2-step modulation requiring both 12-channel carriers in the 192- and 236-kHz band and a 128-kHz premodulation carrier. The advantage was that only one code of channel filter was required, and hence, the same code of channel unit could be used for all 12 channels. In addition, the channel unit used out-of-band signaling at 3825 Hz. This signal tone could be transmitted at either a high level of −5 dBm0 or a low level of −20 dBm0, and it could be used as "tone on" or "tone off" in the idle (on-hook) state.

The new combine-and-split unit provided CCITT levels at the group distributing frame (GDF). It could insert a pilot frequency of either 84.08 or 104.08 kHz into the analog path and included regulating circuits for the receive pilot.

The carrier supply used the LT-1 shelf but was made up of 12 carrier generators whose frequencies were equally spaced between 192 and 236 kHz, a premodulation generator, a pilot generator, a signal

generator, and a power unit. The last four items were duplicated for reliability.

XIII. LT-1 EQUIPMENT DESIGN

13.1 Introduction

The similarities between the LT-1 carrier supply needs and the needs of N4 have been pointed out earlier. Secondly, a number of digital D4 common circuits could be used directly in LT-1. Finally, there was also a similarity in systems' architecture. In its simplest form, LT-1 converted and combined two sets of 12 separate analog signals to form a (digital) DS-1 signal. In D4, 24 separate analog signals were combined to form a DS-1 signal. Additionally, it would be of economic benefit if components, piece parts, or entire units from N4 or D4 that were developed ahead of LT-1 could be used in LT-1.

The plan was to use a reduced N4 carrier supply, the D4 channel bank shelves, and many of the D4 common units, with the LT-1 channel units and certain of the common units being new.

13.2 Equipment considerations

LT-1 operates in conjunction with the digital interface frame (DIF) to terminate analog signals on the 4*ESS* switch. Five DS-1 signals (120 channels) from the LT-1 are combined in the DIF to form a DS-120 signal, which is the input to a 4*ESS* switch. To maintain compatibility with the 4*ESS* switch, LT-1 was made up in multiples of 120 channels.

The decision to use N4 and D4 equipment shelves meant using an unequal flange bay with a nominal width of 2 ft 2 in. Further, since LT-1 was to be installed in a 4*ESS* switch, the bay height (7 ft) was set by the new equipment building standards (NEBS), to which both the DIF and the 4*ESS* switch conformed. An objective of 480 channels for LT-1 in two 7-ft bays was established. This was accomplished by a special channel unit design described below.

13.3 Channel units

The basic D4 shelf assembly consists of four shelves, each with 12 channel units. The shelves are die-cast type with 60 equally spaced slots on both sides for the printed wiring boards. Each channel unit requires four slots, with the remaining ones left over for the common units. This arrangement, if used for LT-1, would result in empty shelf space since not all the D4 common units are needed. To alleviate this problem, the channel units were rearranged so that 48 channel units would fill two shelves (that is, 2-1/2 slots per channel), with the third one for the common units. This was done by turning every second channel unit assembly over so that within a pair of assemblies the

boards were on the outside and the components extended towards the middle. The components on each board were also rearranged so that the high and low components mesh properly without touching. Each double-channel unit thus occupies five slots.

13.4 The LT-1 double digroup

Since LT-1 requires only three of the four shelves, the D4 shelf assembly was reworked. New castings slotted on one side only were designed to be used either as the top or the bottom and were attached by side panels to create a 13-1/2 in. high, 3-shelf module. The center shelf accepts the D4 common units, and the top and the bottom shelves contain the LT-1 channel units. Each shelf assembly is thus a 48-channel, self-contained module; a 480-channel system would require two 7-ft bays.

A fully equipped system (480 channels) with E and M channel units requires 35 different codes, or circuit packs. Of these, six are double channel units, ten are new to LT-1, and the remainder are taken directly or with slight modifications from N4 or D4.

13.5 Carrier supply shelves

Since the LT-1 and N4 were progressing in parallel, the N4 supply shelf was redesigned to meet both LT-1 and N4 carrier supply requirements. The new castings are slotted on one side only so that they can be used as the top or the bottom of a shelf. These castings were screwed to the side plates and to a connector panel (backplane), with provision for 24 carrier units.

13.6 Carrier supply units

The 24 carrier supply units, including those for the carrier failure alarm, were made from 20 codes. Twelve carrier generators provide separate carrier frequencies, of which six were used unchanged from N4, while the other six were modified to remove a transmitted carrier circuit not needed in LT-1. The twelve received their reference frequency from a 4-kHz generator driven from the office primary frequency supply. This unit also provided 4 kHz to the 100.08-kHz carrier failure alarm generator. The 2600-Hz signaling frequency was generated by a free-running oscillator. These three units were duplicated for reliability. Finally, there was an alarm unit and duplicate power units.

13.7 Channel units

A double channel unit consists of two printed wiring boards with components between them. The terminal (pin out) arrangement was kept the same on both boards so that all channel units had the same

functions on the same terminals. This simplified bus wiring on the connector panel backplane for all common functions. Similarly, components that would be adjusted by craft personnel were kept in the same relative position on faceplates. Except for layout, the only difference among 12 channel units of the same general type, within a group, was the frequency of their filters.

The same pair of printed wiring board layouts was used for both E and M and CCIS double-channel units, with the E and M signaling circuits left off the CCIS units. However, a switch was provided on the E and M unit so that it could be converted directly to CCIS.

Later, when the echo-canceler circuits were incorporated into the channel units using a single, 2-1/2 position unit, the high components were placed at the top of the board and the low components at the bottom. This was reversed on the adjacent board, and by using notched faceplates that conformed to the component arrangement, one unit of an opposing pair slid past the other as it was moved in and out of a shelf.

13.8 LT-1 double bay frame

The LT-1 connector is housed in a double bay frame made from two standard 7-ft unequal flange bays set side by side. The base is 4 ft 4 in. wide and 12 in. deep.

Prior to assembly, the individual equipment shelves are wired. The transmit and receive leads from the digroups are then connected to the connectors on the bays.

13.9 Cabling

The transmission path for LT-1 is connected to the GDF on the analog side, and to either the DIF, the digroup terminal (DT), or the digital cross-connect frame (DSX-1) on the digital side.

The analog connections are made using twisted shielded pairs (761A type), with the shields grounded at the GDF and floating at the LT-1. There are two pairs—one transmit and one receive—for each group. They are terminated on the combine-and-split unit connector at the back of the double digroup.

The digital connections are made using 600B (type) cables. The cables for the DIF and DT connections are fully connectorized, while the DSX-1 cable is connectorized at the LT-1 end and wire wrapped at the DSX-1. The aluminum cable sheaths are grounded at the LT-1 bay, and there are separate cables for the transmit and receive paths.

13.10 The LT-1B connector

The LT-1B is packaged in three versions. The first is a 7-ft unequal flanged bay, which, from the top, contained a fuse and alarm panel

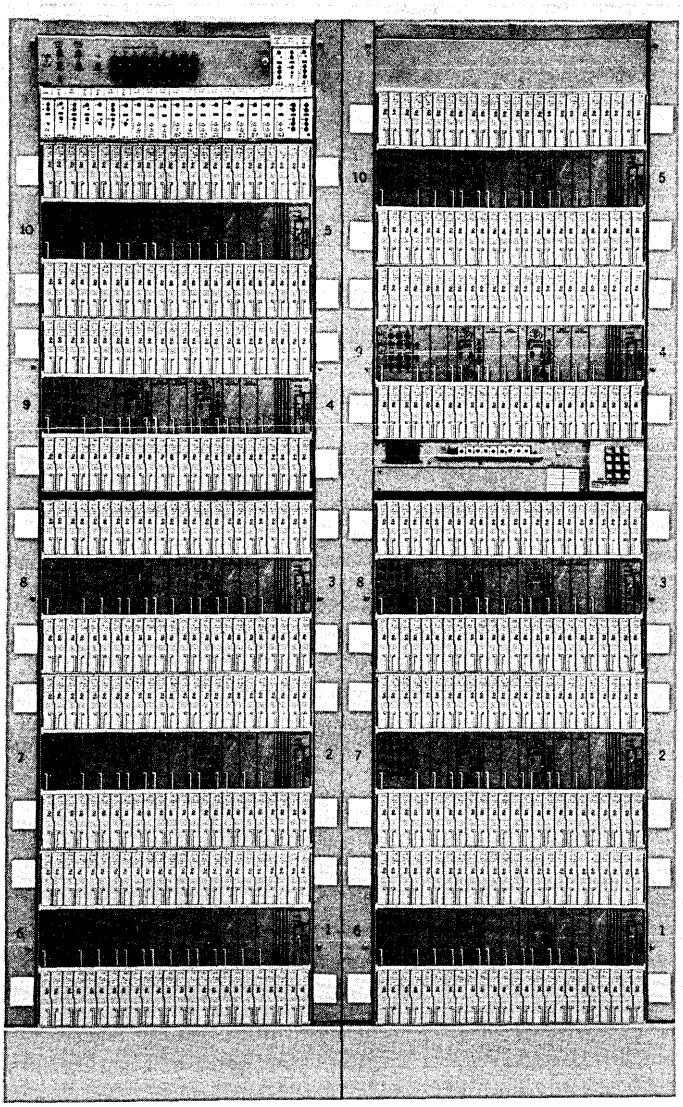

Fig. 11—LT-1B connector primary and secondary bays.

designed for LT-1B, the LT-1 carrier supply, and five modified double digroups. The double digroups have two more connectors on the common shelf connector panel so that they can be used for LT-1 and LT-1B with and without T1C operation. New channel units and a synchronizer/desynchronizer (SYNDES) unit (a D4 circuit) were added. This was the primary bay of a pair and contained 240 channels.

The second bay holds an additional 240 channels. It contains five

double digroups and an optional 660 communications panel located between the third and fourth digroups from the bottom. This bay receives its power and carriers from the primary bay and was alarmed through the bay. The LT-1B primary and secondary bays are shown in Fig. 11.

The third bay is 11 ft 6 in. high and self-contained, with a total of eight double digroups (384 channels). Its layout is similar to the 7-ft primary bay except that between the third and fourth double digroups there is a communications panel, and above the fuse and alarm panel there are three more double digroups.

The channel units are similar in concept to the LT-1 echo cancelers but include four removable circuit modules (daughter boards) containing the signaling circuits. They are completely interchangeable and can be mounted on any of the 12 channel units.

XIV. SUMMARY

This article has described the LT-1 connector design. The original design, intended for 4*ESS* applications, would accommodate E and M and CCIS signaling only. It took maximum advantage of the common technology of D4 and N4, as well as custom integrated circuits. Additional features and signaling capabilities were added to the design for facility interconnect applications. An echo-canceler plug-in was added to improve the grade of service on satellite circuits. Finally, technology developed for international markets was incorporated into the design to interface with an export version of the 4*ESS* switch.

The LT-1 design has been very flexible in meeting the needs of AT&T Communications and the Bell Operating Companies. It economically converts between analog and digital transmission, a critical function as AT&T Communications and the Bell Operating Companies move toward an all-digital network.

REFERENCES

1. D. L. Duttweiler, "A Twelve Channel Digital Echo Canceler," IEEE Trans. Commun., *COM-26*, No. 5 (May 1978), pp. 647–53.
2. R. T. Bobilin and Yau-Chau Ching, "DATS—A New Approach to VF Testing on Digital Carriers," NTC Conference Record, *2* (December 1978), pp. 21.6.1–4.

AUTHORS

George W. Bleisch, B.S.E.E., 1951, University of Rhode Island; AT&T Bell Laboratories, 1951—. After completing the Communications Development Training Program, Mr. Bleisch was involved with circuit development in military systems and systems engineering in data processing studies. Appointed Supervisor in 1961, he has contributed to the N3 carrier terminal, the A6 channel bank, the LMX3 and LMX3E (export) multiplex terminals, and the LT-1 family of transmultiplexers. He is currently responsible for new services development within the Digital Transmission and Services Department. Member, Tau Beta Pi, Phi Kappa Phi, IEEE Communications Society.

Stanley Dodds, B.I.D., 1955, Syracuse University; Defense Research Board of Canada, 1956; AT&T Bell Laboratories, 1961—. For some years Mr. Dodd's principal assignments were in equipment design and station engineering for the Ocean Systems Development Laboratory. Since 1977 he has worked on the physical design of LT transmultiplexers. Member, Tau Sigma Delta, Phi Kappa Phi, Ergonomics Research Society.

William J. Mitchell, B.S.E.E., 1967, Northeastern University; M.S.E.E., 1968, The Massachusetts Institute of Technology; AT&T Bell Laboratories, 1967—. Mr. Mitchell initially worked on the regenerator, timing recovery, and protection for a high-speed digital transmission system. He later was involved with analog multiplex terminals, which led to the development of the LT-1 connector. He is currently Supervisor of the Data Network Hardware Development Group. Member, Tau Beta Pi, Phi Kappa Phi, Eta Kappa Nu.

AT&T Bell Laboratories Technical Journal
Vol. 63, No. 6, July–August 1984
Printed in U.S.A.

Electrical Transmission Lines as Models for Soliton Propagation in Materials: Elementary Aspects of Video Solitons

By G. E. PETERSON*

(Manuscript received September 29, 1983)

Distributed electrical and mechanical transmission lines are useful models for nonlinear wave motion with dispersion in many interesting physical systems. Nonlinear wave motion with dispersion produces solitons in optical fibers. A soliton will propagate along an appropriate transmission line with constant velocity and without change in shape. The shape remains the same because the nonlinearity of the medium creates higher harmonics and a steeper pulse, whereas dispersion tends to broaden the pulse. A balance between the two is reached, and a stable pulse results. Thus, a communication system using solitons might be advantageous. Electrical distributed lines have an obvious direct application to integrated circuit parametric amplifiers, harmonic generators, and shock-wave generators for pulse shaping. They also have applications to secret, or secure, coding systems using two soliton interactions, and to data transmission using solitons.

I. INTRODUCTION

The study of nonlinear wave propagation along distributed electrical and mechanical transmission lines is important because these lines serve as useful models for nonlinear wave motion with dispersion in many interesting physical systems. Recently, nonlinear wave motion with dispersion has been shown to produce solitons in optical fibers.[1]

*AT&T Bell Laboratories.

Copyright © 1984 AT&T. Photo reproduction for noncommercial use is permitted without payment of royalty provided that each reproduction is done without alteration and that the Journal reference and copyright notice are included on the first page. The title and abstract, but no other portions, of this paper may be copied or distributed royalty free by computer-based and other information-service systems without further permission. Permission to reproduce or republish any other portion of this paper must be obtained from the Editor.

To design devices with exotic properties, one often needs exotic materials. It is very costly in time and money to try to produce these by strictly trial and error methods. Thus the usefulness of models becomes clear. In addition, they permit us to check quickly the accuracy of our computer solutions to certain partial differential equations that describe propagation in nonlinear materials.

Of course, the electrical distributed lines have an obvious direct application to integrated circuit parametric amplifiers, harmonic generators, and shock-wave generators for pulse shaping.[2] They also have applications to secret, or secure, coding systems using two soliton interactions, and to data transmission using solitons.[3,4,5] In this paper we study soliton propagation in materials by means of electrical and mechanical models, and numerical solutions to the appropriate, nonlinear, partial differential equations. Particular attention is paid to multisoliton interactions and the Fermi, Pasta, and Ulam problem.

To a large extent, the material considered in this paper is that which seems appropriate to the materials scientist, and we extract liberally from the literature. This paper is largely concerned with elementary videosolitons, while a proposed paper, with modulated waves in nonlinear dispersive media, is related to the interesting works of Hasegawa and Tappert,[6,7] and to more advanced videosoliton topics.

1.1 The Fermi, Pasta, and Ulam study of nonlinear problems

In 1955 Fermi and co-workers Pasta and Ulam did a remarkable analysis of nonlinear problems. They studied a one-dimensional dynamical system of 64 particles with nonlinear forces between neighbors. In particular, they examined quadratric, cubic, and broken linear types of forces. The behavior of the system was studied for times long compared to the oscillation periods of the related linear problem. Their primary aim was to establish, by means of a computer analysis, the rate of approach to equipartition of energy among the various modes. The nonlinear terms they chose were quite small compared to the linear ones, usually about 10 percent smaller. Basically, they had a string with fixed ends, whose restoring force contained higher-order terms.

For the familiar linear problem, if the initial position of the string is sinusoidal, it will oscillate in this mode forever. Their interest was to watch the string get into complicated shapes because of the nonlinear forces, and eventually, after a sufficient time, get into shapes where all the Fourier modes would be equally important. We now quote from their paper:

> Let us say here that the results of our computations show features which were, from the beginning, surprising to us. Instead of a gradual, continuous flow of energy from the first mode to the higher modes, all of the problems show an entirely different behavior. Starting in one problem with a quadratic force and a pure sine

wave as the initial position of the string, we indeed observe initially a gradual increase of energy in the higher modes as predicted (e.g., by Rayleigh in an infinitesimal analysis). Mode 2 starts increasing first, followed by mode 3, and so on. Later on, however, this gradual sharing of energy among successive modes ceases. Instead, it is one or the other mode that predominates. For example, mode 2 decides, as it were, to increase rather rapidly at the cost of all other modes and becomes predominant. At one time, it has more energy than all the others put together! Then mode 3 undertakes this role. It is only the first few modes which exchange energy among themselves and they do this in a rather regular fashion. Finally, at a later time mode 1 comes back to within one percent of its initial value so that the system seems to be almost periodic. All our problems have at least this one feature in common. Instead of gradual increase of all the higher modes, the energy is exchanged, essentially, among only a certain few. It is, therefore, very hard to observe the rate of 'thermalization' or mixing in our problem, and this was the initial purpose of the calculation.[8]

Figure 1a is taken from this remarkable paper. The horizontal axis is time, the vertical axes is energy, and the number specifies a particular mode. Certainly there is little, if any, tendency towards equipartition of energy among the modes at a given time, and thus there is no mixing.

Figure 1b, which is also taken from the same paper, shows the actual shapes of the string at various cycles of oscillation. (The number is the total number of oscillation cycles.) The initial displacement, as before, is sinusoidal. What is interesting here is that after many, many cycles the sinusoidal shape again appears.

Again we quote:

It is not easy to summarize the results of the various special cases. One feature which they have in common is familiar from certain problems in mechanics of systems with a few degrees of freedom. In the compound pendulum problem one has a transformation of energy from one degree of freedom to another and back again, and not a continually increasing sharing of energy between the two. What is perhaps surprising in our problem is that this kind of behavior still appears in systems with, say, 16 or more degrees of freedom.[8]

Actually, the motion is stranger than that just described. Further work by Tuck and Menzel[9] has shown that the return of the string to its original state is not complete on the first return cycle, because 1 or 2 percent of the energy remains in higher modes. After eight return cycles the deviation is 8 percent, or worse than a single return cycle. Strangely enough, after 16 return cycles it is nearly in the original state!

1.2 The observation of Scott-Russell

J. Scott-Russell in 1844 published a paper entitled "Report on Waves" in the Proceedings of the Royal Society of Edinburgh. We quote from his paper:

I was observing the motion of a boat which was rapidly drawn along a narrow channel by a pair of horses, when the boat suddenly stopped—not so the mass of water in the channel which it had put in motion; it accumulated round the prow of

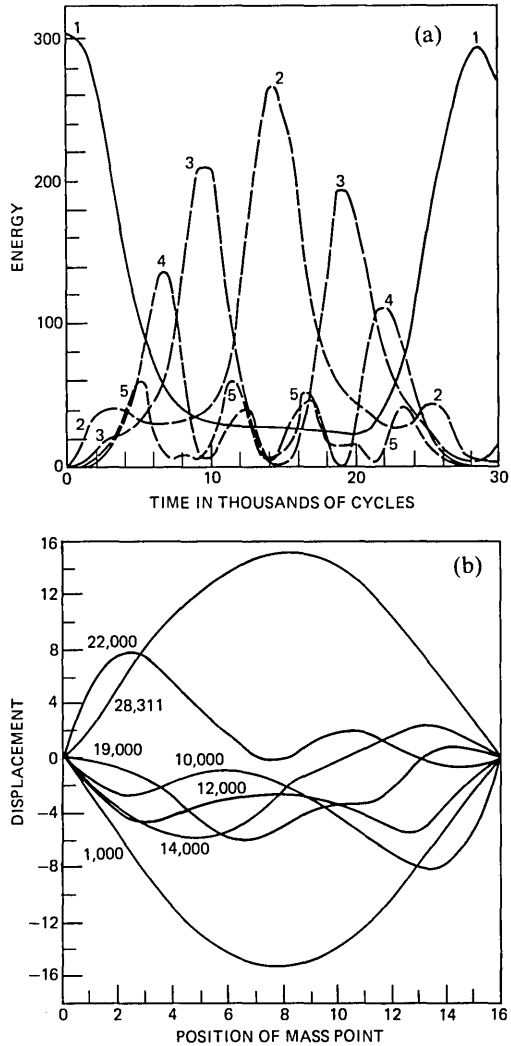

Fig. 1—(a) Energy in each of the first five modes. Initial form of string was single sine wave. Higher modes never exceed 20 units in energy. (b) Actual shape of string at various times.

> the vessel in a state of violent agitation, then suddenly leaving it behind, rolled forward with great velocity, assuming the form of a large solitary elevation, a rounded, smooth and well-defined heap of water, which continued its course along the channel apparently without change of form or diminution of speed. I followed it on horseback, and overtook it still rolling on at a rate of some eight or nine miles an hour, preserving its original figure some thirty feet long and a foot to a foot and a half in height. Its height gradually diminished, and after a chase of one or two miles I lost it in the windings of the channel. Such, in the month of August 1834, was my first chance interview with that singular and beautiful phenomenon . . . .[10]

Thus, we have another example of the remarkable properties of

nonlinear wave motion. In 1895 Korteweg and deVries[11] developed their famous equation for shallow-water waves. This equation includes both nonlinear and dispersive effects. One form of it is[12]

$$U_t - 6UU_x + U_{xxx} = 0. \tag{1}$$

This very important wave equation, commonly called the K-dV equation, appears in many branches of physics, including plasma physics, fluid dynamics, and solid-state physics. Solutions to the K-dV equation are the solitary waves described by Scott-Russell.

The variable U represents the perturbation of a physical quantity from its equilibrium value. Its change in time, U_t, is influenced by dispersion, U_{xxx}, which distorts and spreads it, and by nonlinearity, UU_x, which sharpens and steepens it. If these terms balance, we have a soliton solution. This is clearly a special solution to the partial differential equation. Surprisingly, this solution, or soliton, is fairly easy to launch.

II. SOLITONS

We can introduce the concept of a soliton by considering the giant solitary wave described so eloquently by Scott-Russell. We look for traveling-wave solutions to the Korteweg and deVries equation of the form[12]

$$U(x, t) = U(x - ct) = U(\xi). \tag{2}$$

This corresponds to going to a steady moving reference frame with velocity c.

It is clear that

$$\frac{\partial}{\partial x} = \frac{d}{d\xi} \tag{3}$$

and

$$\frac{\partial}{\partial t} = -c\,\frac{d}{d\xi}. \tag{4}$$

Thus we find that

$$U_{\xi\xi\xi} - (6U - c)U_\xi = 0. \tag{5}$$

We see that the partial differential equation has been reduced to an ordinary differential equation. The soliton waves are given by

$$U(x, t) = -\tfrac{1}{2}a^2\mathrm{sech}^2[\tfrac{1}{2}a(x - x_o - a^2t)], \tag{6}$$

which can be checked by substitution. In this expression, x_o is the location of the symmetrical wave at $t = 0$. We note that this wave moves to the right with a velocity a^2. We also note that the amplitude of the wave is proportional to a^2 and that the width is proportional to

a. Since the speed of the wave depends upon its amplitude, a taller wave can overtake a shorter one moving in the same direction.

One might expect that when the two waves interact, because of the nonlinearity, there will be a massive altering of their shapes and speeds after the collison. This is not the case! The surprising result is that they emerge from the interaction completely preserved in shape and speed, with only a shift in position relative to where they would have been had no interaction taken place. Thus, in ferreting out solitons, we first determine whether a solitary wave exists, then we see if these waves retain their shape and velocity after a collision. Scott[13] has given some working definitions for solitary waves and solitons.

Definition: A solitary wave, $\phi_{st}(\xi)$, is a localized traveling wave. More precisely, a traveling wave whose transition from one constant asymptotic state—as $\xi \to -\infty$ (possibly), another as $\xi \to +\infty$—is essentially localized in ξ.

Definition: A soliton $\phi_x(x - ct)$ is a solitary-wave solution of a wave equation that asymptotically preserves its shape and velocity upon collision with other solitary waves. That is, given any solution $\phi(x, t)$ composed only of solitary waves for large negative time,

$$\phi(x, t) \sim \sum_j \phi_{st}(\xi_j) \quad \text{as} \quad t \to -\infty, \tag{7}$$

where $\xi = x - c_j t$. Such solitary waves will be called solitons if they emerge from the interaction with no more than a phase shift.
We see that

$$\phi(x, t) \sim \sum_j \phi_{st}(\bar{\xi}_j) \quad \text{as} \quad t \to +\infty, \tag{8}$$

and

$$\bar{\xi}_j = x - c_j t + \delta_j, \tag{9}$$

with

$$\delta_j = \text{constant}. \tag{10}$$

There are, of course, quite a few nonlinear partial differential equations that are interesting from the point of view of soliton theory. We list a few of these, along with the Lagrangian density, L, from which they can be derived. The Lagrangian density is useful because it allows us to calculate certain conserved densities.

1. The generalized K-dV equation:

$$U_t + \alpha U U_x + U_{xxx} = 0 \tag{11}$$

$$L = \frac{1}{2} W_x W_t + \frac{\alpha}{6} W_x^3 + W_x V_x + \frac{1}{2} V^2, \tag{12}$$

where

$$W_x = U \quad \text{and} \quad W_{xx} = V. \tag{13}$$

A two-interacting-soliton solution is the following:[13,14]

$$U(x, t) = \frac{216 + 288 \cosh(2x - 8t) + 72 \cosh(4x - 64t)}{\alpha[3 \cosh(x - 28t) + \cosh(3x - 36t)]^2}. \tag{14}$$

2. The sine Gordon equation:[15]

$$U_{tt} - U_{xx} + \sin U = 0 \tag{15}$$

$$L = \frac{1}{2}(U_x^2) - \cos U. \tag{16}$$

The quantity U often has the meaning of an angle. The following solution represents solitons, U_+, and antisolitons, U_-:

$$U_\pm = 4 \tan^{-1}\left\{\exp\left(\pm \frac{x - ct}{\sqrt{1 - c^2}}\right)\right\}. \tag{17}$$

3. The Nonlinear Schrodinger equation:[1,6,7,16]

$$U_{xx} + iU_t + K|U^2|U = 0 \tag{18}$$

$$L = i/2(UU_t^* - U^*U_t) + |U_x|^2 - \frac{K}{2}|U|^4. \tag{19}$$

4. The Born and Infeld equation:[17]

$$(1 - U_t^2)U_{xx} + 2U_xU_tU_{xt} - (1 + U_x^2)U_{tt} = 0 \tag{20}$$

$$L = (1 + U_x^2 - U_t^2)^{1/2}. \tag{21}$$

We should point out that the simplest partial differential equation that has soliton solutions is

$$U_{xx} - 1/c^2U_{tt} = 0. \tag{22}$$

It is dispersionless and linear in contrast to those described earlier, which contained dispersion and nonlinear terms. It is important to realize that if the propagating medium is linear and dispersive, or nonlinear and dispersionless, solitons cannot exist.

2.1 The Toda lattice[18–22]

We are, of course, all familiar with a one-dimensional lattice of mass points. For a vibronic analysis these points are imagined to be connected by springs. In the case of large vibrations they can show nonlinearities. Toda considered a one-dimensional lattice with a potential of the form

$$\frac{a}{b}[\exp(y_j - y_{j-1})] + a(y_j - y_{j-1}) - \frac{a}{b}. \tag{23}$$

Subsequently, Flaschka[23,24] showed that this lattice was a finite-dimensional analogue of the K-dV equation. Also, certain integrals of the Toda equations are the counterparts of the conserved quantities of the K-dV equation.

The Toda-lattice equations can be written as

$$m\frac{d^2y_n}{dt^2} = a[\exp(-br_n) - \exp(-br_{n+1})], \tag{24}$$

where

$$r_n = y_n - y_{n-1}. \tag{25}$$

The Lagrangian is

$$L = \sum_n \frac{m}{2}\dot{y}_a^2 - \frac{a}{b}\exp(-br_n) + \frac{a}{b}\exp(-br_{n+1}). \tag{26}$$

We should remark that a series of mass points coupled by springs has the electrical analogy of a series of inductor-capacitor, low-pass circuits.

Toda obtained analytical solutions to the equations of motion and discovered lattice solitons, i.e., solitons in a nonlinear lattice. He proved that these solitons passed through one another without losing their identity. The solitary-wave solution he found was

$$\phi = \frac{1}{4}\frac{m}{ab}p^2\text{sech}^2\left[\frac{1}{2}(Kn - \beta t) + \delta\right], \tag{27}$$

where ϕ is the force between mass points, K and δ are constants, and

$$\beta^2 = (4ab/m)\sin h^2(K/2). \tag{28}$$

2.2 Solitons in the Morse and other lattices[25–28]

The Morse potential is of the form

$$[\exp(y_j - y_{j-1}) - 1]^2. \tag{29}$$

Rolfe et al.[25] have studied solitons in this lattice by numerical methods. The shape of the solitons is nearly Gaussian. An initial pulse very quickly separates into pairs of pulses that travel in opposite directions and appear to propagate indefinitely. That they are indeed solitons can be verified by studying the collisions between the pulses. As required, there is no change except for a phase shift. In general, the Morse-soliton shape is well approximated by the Toda-soliton shape.

Another family of lattice potentials is the power-law family, which can be specified as M-N, where M is the attractive power and N the

repulsive power. For example, 6–12 is the well-known Lennard-Jones potential, which is 6-power attractive and 12-power repulsive. Another one is the 6–32, or "screw", lattice.

It is very striking that the soliton shapes and behavior are all very nearly the same. Thus the Toda soliton is ubiquitous! This may be because of the similarity of the repulsive walls.

III. LINEAR TRANSMISSION LINES

Consider the transmission line shown in Fig. 2. We have all endlessly analyzed this circuit or variations of it in elementary physics, mathematics, or electronics courses. We recognize immediately that the inductance, L, and the capacitance, C, are analogous to mass, M, and force constant, K, of a lattice. Sometimes we look upon such a line as having an inductance-per-unit length, L, and a capacitance-per-unit length, C. Then, instead of a sequence of low-pass filters, we have something akin to a coaxial cable. Likewise, in the mechanical case, instead of a one-dimensional lattice we have a string. We might also say that we have a string with point masses on it, which in the limit becomes a uniform string. It is important to realize that a uniform vibrating string supports an infinity of modes, while a string with point masses on it "gets into trouble" if the frequency is too high. The same is true in the electrical case.

The partial differential equation of a uniform[29] distributed line is

$$-V_x = LI_t \tag{30}$$

$$-I_x = CV_t \tag{31}$$

or

$$V_{xx} = LCV_{tt}, \tag{32}$$

with solutions of the form[29]

$$V = f(\sqrt{LC}\, x \pm t). \tag{33}$$

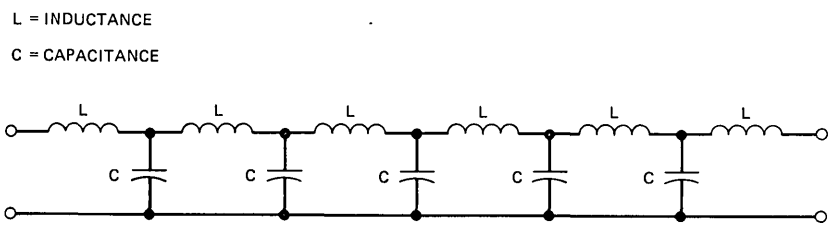

Fig. 2—Linear transmission line consisting of a sequence of inductors, L, and capacitors, C.

This is so familiar that it need not be pursued further. If, however, the capacitance or inductance is nonlinear, then new phenomena arise, for example, shock waves.

3.1 Shock waves in nonlinear transmission lines

Shock waves are familiar to all of us. We need only think about the sonic boom of the Concord supersonic jet or the firing of a rifle. In fact, even the noise caused by an auto collision on a high-speed highway is a shock wave.

Consider now the nonlinear transmission line shown in Fig. 3. Here the capacitance of c is a function of voltage. Let us again consider the capacitance and inductance to be distributed. Then the partial differential equation becomes

$$-V_x = -LI_t \tag{34}$$

$$-I_x = -C(v)V_t. \tag{35}$$

In analogy, with the solution of the linear line, we guess that the following is the solution:

$$V = f(\sqrt{LC(v)}\ x \pm t). \tag{36}$$

This can be shown to be correct.[30] Thus, we see that the velocity of a disturbance is a function of its amplitude. In fact, we expect that the higher-voltage parts will travel at a different speed than the lower-voltage parts.

One form of a nonlinear capacitance is the reversed bias p-n diode. In this case the larger the voltage, the lower the capacitance. This implies that the higher voltage peak of a waveform will travel faster than the lower voltage bottom. Thus, given enough distance or time, the peak can overtake the bottom and a voltage shock can develop.

Shock-wave formation is one of the more interesting phenomena found in the study of wave propagation through nonlinear media. There are quite a few papers in the literature describing shocks on

L = INDUCTANCE

C(v) = VOLTAGE-DEPENDENT CAPACITANCE

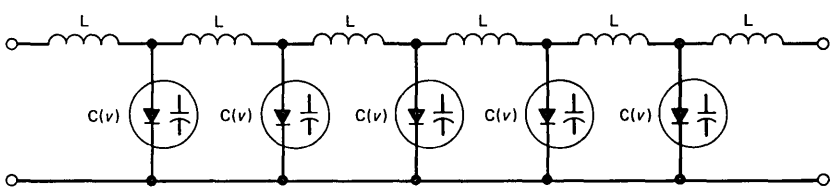

Fig. 3—Nonlinear transmission line, with capacitor, C, a function of voltage.

nonlinear, and nonlinear and dispersive, transmission lines.[31] In fact, there are even books devoted entirely to this topic. One way of looking at shock waves is to imagine that the nonlinearities are constantly building up higher and higher harmonics of the propagating wave.

One of the problems involved in shock-wave studies on transmission lines, and in other nonlinear systems as well, is impedance matching. In general, a line with only one nonlinearity, inductive or capacitive, generates a reflected wave, which reduces the shock amplitude. However, if both the inductance and capacitance are nonlinear functions, and, in particular, if $L(\xi) = \text{constant} \times C(\xi)$, then the characteristic impedance is a constant.

Fallside et al. have described a line with[31,32]

$$C = \frac{C_o}{\sqrt{|V|}} \tag{37}$$

and

$$L = \frac{L_o}{\sqrt{|I|}}. \tag{38}$$

In a region of forward simple waves this line has a constant impedance Z_o, given by

$$Z_o = (L_o/C_o)^{2/3} \tag{39}$$

and phase velocity, U, given by

$$U = \sqrt{|V|}\, L_o^{2/3}/C_o^{1/3}. \tag{40}$$

Figure 4 shows typical shock waves formed by this line. We note in particular the sharpness of the shock-wave front.

Our experience with linear transmission lines suggests that the nonlinear partial differential equations should represent forward-traveling and backward-traveling waves. Because of the nonlinearity, the principle of superposition cannot be applied. A very powerful way to solve those partial differential equations is the method of character-

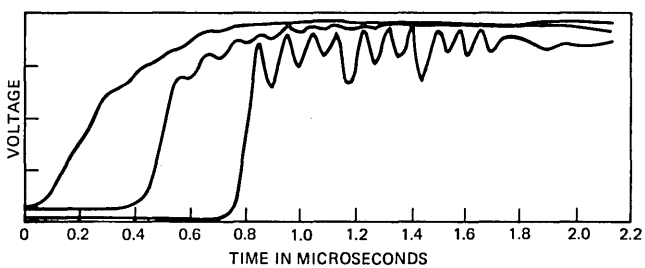

Fig. 4—Typical shock waves on transmission line of Fallside et al.

istics.[33] It is widely used in the study of gas dynamics, and the procedure can be found in the literature.

3.2 Solitons on transmission lines[34–40]

Figure 5 shows four types of wave-propagating media. In a linear-dispersionless media, solitary waves can exist. In a nonlinear-dispersionless media, shock waves exist. In a nonlinear media with dispersion, solitons and solitary waves exist. In a linear media with dispersion, broadening pulses exist. Let us now focus our attention on the electrical analogue of the Toda lattice.

This network consists of a sequence of LC networks with nonlinear capacitors; and the circuit is dispersive. The K-dV equation, as mentioned earlier, is an asymptotic equation for a weakly nonlinear lattice. A beautiful analysis of the K-dV equation, by Zabusky and Kruskal,[40] gives us insight into what we will see on our transmission line. The expected phenomena can be broken into four time intervals.

1. Initially, the first two terms of the K-dV equation dominate, i.e.:

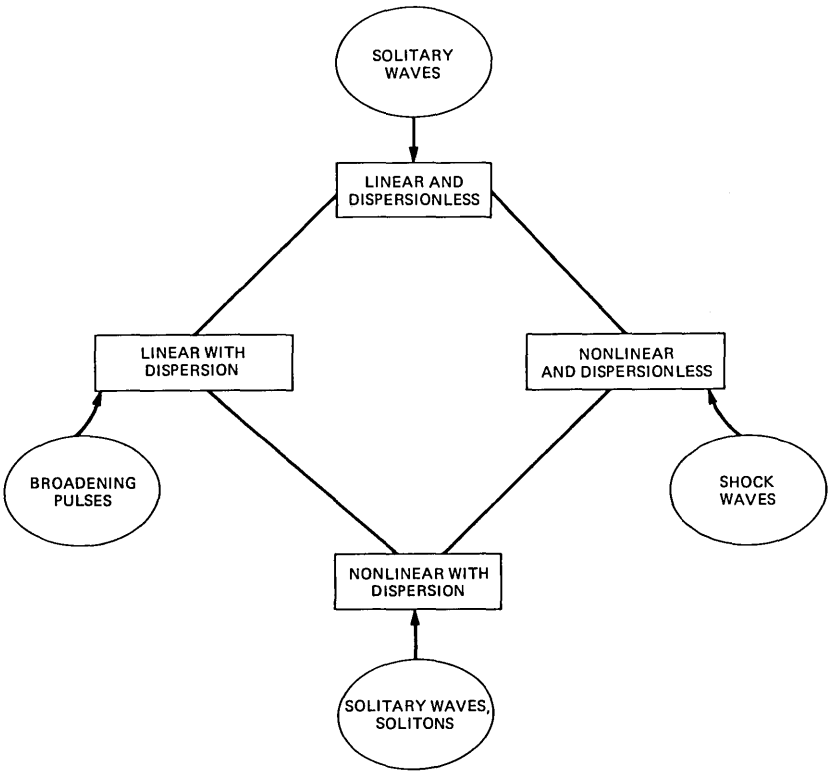

Fig. 5—Four types of wave-propagating media and the types of waves to be expected.

$$U_t + UU_x. \tag{41}$$

A shock starts to develop, and U steepens in regions where it has a negative slope.

2. After U has become quite steep, the third term comes into play and prevents a discontinuity:

$$U_t + U_{xxx}. \tag{42}$$

Oscillations then develop.

3. Solitons are "shaken off", and each propagates with a velocity proportional to its amplitude.

4. After a sufficient length of time, all the solitons come together with a phase that can almost reconstruct the initial waveform.

The propagation equations for the networks are:[35]

$$\frac{\partial}{\partial t} LI_n(t) = V_n(t) - V_{n+1}(t), \tag{43}$$

$$\frac{\partial}{\partial t} Q_n(t) = I_{n-1}(t) - I_n(t), \tag{44}$$

and

$$Q_n(t) = C(V_n(t))\ V_n(t). \tag{45}$$

Here V_n is the voltage across the nth nonlinear capacitor, and I_n is the current through the nth inductor.

3.3 Experiments with a Toda-lattice transmission line

Hirota[35] has reported his experiments with a transmission line having $L = 22\ \mu$H, and $C(v) = 27v^{-0.48}$ pf. Figure 6 shows that applying a pulse to the line results in a train of solitons. In addition, there is a low-amplitude oscillatory tail formed. It is clear from eq. (43) that

$$\int_{-\infty}^{+\infty} V_n(t)dt = \text{constant, independent of } n. \tag{46}$$

Thus, the area under the pulse and the area under the solitons should be the same. This is found to be true to about 2 percent.

Let us now consider the case of two solitons of different amplitudes moving in the same direction on the nonlinear transmission line. The larger one moves faster than the smaller one and eventually swallows it up. The amplitude *decreases* during the overlap period. Finally, the larger soliton emits the smaller one, which then proceeds on its way unaltered.

Suppose we now consider two solitons moving towards each other on the transmission line. In this case both solitons have the same amplitude. During the overlap the amplitude *increases* rather than

decreases as in the previous case. After the collision both solitons proceed on their way essentially unaltered.

The Fermi, Pasta, and Ulam phenomena can easily be observed on the Toda-lattice transmission line. A sinusoidal signal is introduced onto the line. By observing the waveform at various points along the line, we can examine the influence of nonlinearity and dispersion on the signal. These results are shown in Fig. 7. Figure 7a shows the input sine wave. In Figs. 7b and c the signal is progressively decom-

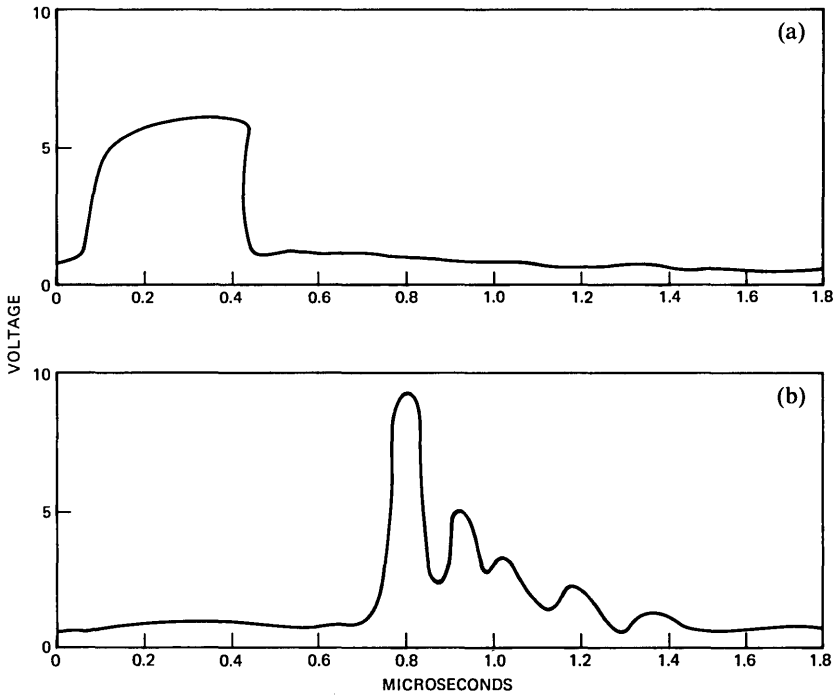

Fig. 6—Decomposition of a pulse into a finite train of solitons.

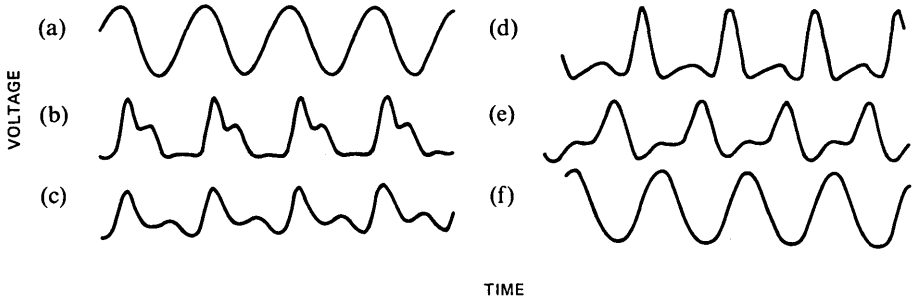

Fig. 7—Fermi, Pasta, and Ulam recurrence phenomena.

posed into higher harmonics, or solitons. In Figs. 7d and e the decomposition is reversing itself. Finally, Fig. 7f is reached, where the original sinusoidal signal has been reconstructed. The recurrence period (or distance) depends very strongly on the amplitude and frequency of the input sine wave. The higher the frequency and amplitude, the shorter the recurrence distance.

3.4 Other transmission lines

Besides the Toda-lattice transmission line, there are a variety of other electrical transmission lines on which solitons can readily be studied. Figure 8 shows four such transmission lines. Two of these have nonlinear inductances, and two have nonlinear capacitances. By a proper choice of parameters, we can simulate the dispersion relations for the electron wave functions in the Kronig and Penney band theory of semiconductors, ion acoustic waves in plasmas, or Trivelpiece and Gould waves.[41] Recently, Jäger and Tegude[42] have reported a nonlinear transmission line that has a cutoff frequency of about 500 mHz. This permits very interesting studies to be performed on a short length of line.

It seems quite clear that analogues can be made for other partial differential equations besides the K-dV and the Toda lattice. For example, Scott[43] has given both electrical and mechanical transmission lines that simulate the Klein and Gordon equation. This equation is particularly interesting because it describes the motion of a block wall between ferromagnetic domains, motion of a slide dislocation in a

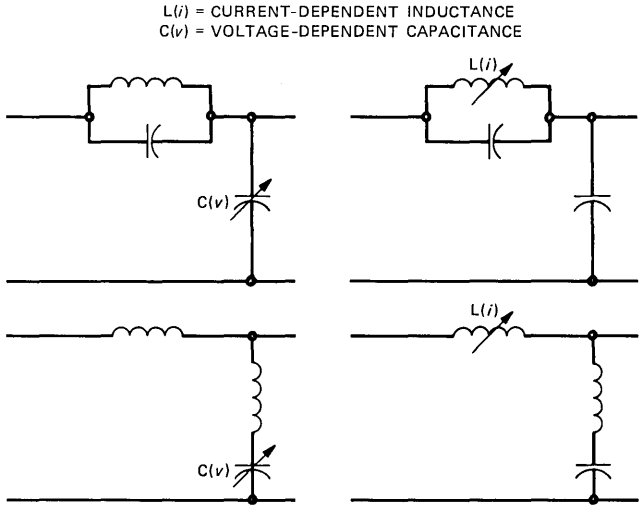

Fig. 8—Nonlinear transmission lines where solitons can propagate.

crystalline structure, and one-dimensional models for elementary particles.

IV. APPLICATIONS OF SOLITONS TO COMMUNICATION SYSTEMS[44–47]

Since a soliton will propagate along an appropriate transmission line with constant velocity and without change in shape, a communication system using solitons might be advantageous. We remind the reader that the shape remains the same because the nonlinearity of the medium is creating higher harmonics and a steeper pulse, whereas dispersion is constraining the harmonics and tending to broaden the pulse. A balance between the two is reached, and stable pulse results.

Chu and Whitbread[46] have reported their experiments on a Pulse Code Modulation (PCM) system using solitons. A soliton is excited by a rectangular pulse in the transmitter. In the receiver the incoming pulse is sent directly to a threshold detector. *No equalizer is needed,* because a soliton suffers no distortion.

One problem involved in a soliton transmission system is that the soliton sometimes has an oscillatory tail, which influences the velocity of the soliton following it. For an optimum system this tail should be suppressed. Another problem with such a system is impedance matching of the nonlinear transmission line. Chu and Whitbread solve this problem by terminating the line with a piecewise simulation of a nonlinear resistance. Figure 9 shows a block diagram of their system. They conclude that:

1. It is practical to use solitons as signal carriers in a PCM communication system.
2. The main source of jitter is an oscillatory tail, which can be removed.
3. A properly designed system would incur a lower bit error rate

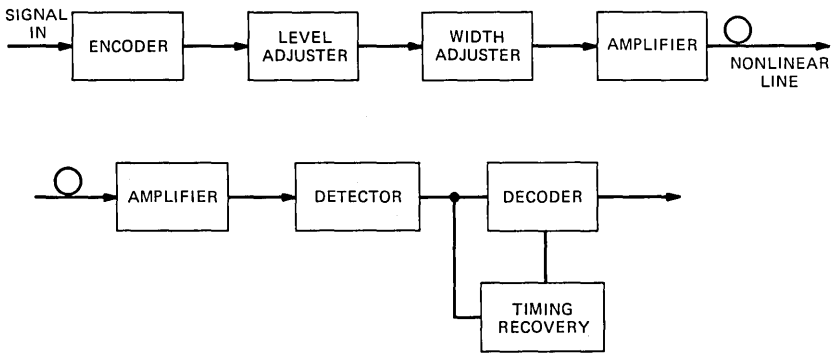

Fig. 9—Pulse code modulation transmission system employing solitons.

than the corresponding system using a linear, dispersive transmission line.

Suzuki, Hirota, and Yoshikawa[44,45] have described a multiplex system based upon the unique properties of solitons. If a sinusoidal signal is introduced into an electrical equivalent of the Toda lattice, it is converted into solitons. Proper choice of lattice and frequency will produce two solitons of different amplitudes. These individual solitons can then be amplitude- or phase-modulated.

Suppose now these two *modulated* solitons are introduced into a nonlinear network. The solitons meet, overlap, and combine into a single carrier, which can be transmitted. This is just an example of the Fermi, Pasta, and Ulam phenomena. The modulation on the combined signal appears to be quite arbitrary, and it is very difficult to distinguish the two original modulating signals that comprise it.

If the receiver is equipped with the same nonlinear network, the signal is converted back into the original pair of separately modulated soliton trains. Strange as it seems, the feasibility of this multiplex system has been successfully demonstrated.

The proposed paper will discuss modulated waves in nonlinear dispersive media—for example, the work of Karpman and Krushkal.[47] In addition, some of the more advanced video soliton topics will be examined.

REFERENCES

1. L. F. Mollenauer, R. H. Stolen, and J. P. Gordon, "Experimental Observation of Picosecond Pulse Narrowing and Solitons in Optical Fibers," Phys. Rev. Lett., *45* (September 1980), pp. 1095–8.
2. D. Jäger and F. J. Tegude, "Nonlinear Wave Propagation Along Periodic-Loaded Transmission Line," Appl. Phys., *15* (April 1978), pp. 393–7.
3. P. L. Chu and T. Whitbread, "Application of Solitons to Communication System," Electron. Lett., *14* (1978), p. 531.
4. K. Suzuki, R. Hirota, and K. Yoshikawa, "Amplitude-Modulated Soliton Trains and Coding-Decoding Applications," Int. J. Electron., *34*, No. 6 (1973), pp. 777–84.
5. K. Suzuki, R. Hirota, and K. Yoshikawa, "The Properties of Phase Modulated Soliton Trains," Jap. J. Appl. Phys., *12* (March 1973), pp. 361–5.
6. A. Hasegawa and F. Tappert, "Transmission of Stationary Nonlinear Optical Pulses in Dispersive Dielectric Fibers. I. Anomalous Dispersion," Appl. Phys. Lett., *23* (August 1973), pp. 142–4.
7. A. Hasegawa and F. Tappert, "Transmission of Stationary Nonlinear Optical Pulses in Dispersive Dielectric Fibers. II. Normal Dispersion," Appl. Phys. Lett., *23* (August 1973), pp. 171–2.
8. E. Fermi, J. R. Pasta, and S. M. Ulam, "Studies of Nonlinear Problems," in *Collected Papers of Enrico Fermi*, Vol. 2, Chicago: Univ. of Chicago Press, 1965, pp. 978–88.
9. J. Tuck and M. Menzel, in *Collected Papers of Enrico Fermi*, Vol. 2, Chicago: Univ. of Chicago Press, 1965, p. 978.
10. J. Scott-Russell, "Report on Waves," Proc. Roy. Soc. Edinburgh (1844), pp. 319–20.
11. D. J. Korteweg and G. deVries, "On the Change of Form of Long Waves Advancing in a Rectangular Canal, and on a New Type of Long Stationary Waves," Phil. Mag., *39* (1895), pp. 422–43.
12. R. M. Miura, "The Korteweg-deVries Equation: A Survey of Results," SIAM Review, *18* (July 1976), pp. 412–59.

13. A. C. Scott, F. Y. F. Chu, and D. W. McLaughlin, "The Soliton: A New Concept in Applied Science," Proc. IEEE, *61* (October 1973), pp. 1443–83.
14. N. J. Zabusky, "Solitons and Bound States of the Time-Independent Schrödinger Equation," Phys. Rev., *168* (April 1968), pp. 124–8.
15. P. L. E. Uslenghi, "An Introduction to Some Mathematical Techniques for Nonlinear Problems," in *Nonlinear Electromagnetics*, P. L. E. Uslenghi, Ed., Academic Press, 1980, p. 28.
16. V. I. Karpman and E. M. Krushkal, "Modulated Waves in Nonlinear Dispersive Media," Sov. Phys. JETP, *28* (February 1969), pp. 277–81.
17. M. Born and L. Infeld, "Foundations of a New Field Theory," Proc. Roy. Soc. London, *144A* (1934), pp. 425–57.
18. M. Toda, "Vibration of a Chain With Nonlinear Interaction," J. Phys. Soc. Jap., *22* (February 1967), pp. 431–6.
19. M. Toda, "Wave Propagation in Anharmonic Lattices," J. Phys. Soc. Jap., *23* (September 1967), pp. 501–6.
20. M. Toda, "Waves in Nonlinear Lattice," Suppl. Progr. Theor. Phys., *45* (1970), p. 174.
21. N. Ooyama and N. Saito, "On the Stability of Lattice Solitons," Suppl. Progr. Theor. Phys., *45* (1970), pp. 201–8.
22. M. Toda and M. Wadati, "Soliton and Two Solitons in an Exponential Lattice and Related Equations," J. Phys. Soc. Jap., *34* (January 1973), pp. 18–25.
23. H. Flaschka, "The Toda Lattice. II. Existence of Integrals," Phys. Rev., B, *9* (February 1974), p. 1924.
24. M. Henon, "Integrals of the Toda Lattice," Phys. Rev., B, *9* (February 1974), pp. 1921–3.
25. T. J. Rolfe, S. A. Rice, and J. Dancz, "A Numerical Study of Large Amplitude Motion on a Chain of Coupled Nonlinear Oscillators," J. Chem. Phys., *70* (January 1979), pp. 26–33.
26. C. Dancz and S. A. Rice, "Large Amplitude Vibrational Motion in a One Dimensional Chain: Coherent State Representation," J. Chem. Phys., *67* (August 1977), pp. 1418–26.
27. T. J. Rolfe and S. A. Rice, "Simulation Studies of the Scattering of a Solitary Wave by a Mass Impurity in a Chain of Nonlinear Oscillators," Physica, *1D* (December 1980), pp. 375–82.
28. M. A. Collins, "A Quasicontinuum Approximation for Solitons in an Atomic Chain," Chem. Phys. Lett., *77* (January 1981), pp. 342–7.
29. J. L. Stewart, *Circuit Analysis of Transmission Lines*, New York: Wiley 1958, p. 12.
30. A. Scott, *Active and Nonlinear Wave Propagation in Electronics*, New York: Wiley-Interscience, 1970, p. 226.
31. F. Fallside, "Shock Waves in a Nonlinear Delay Line," Electron. Lett., *2* (January 1966), pp. 5–7.
32. F. Fallside and D. T. Bickley, "Nonlinear Delay Line With a Constant Characteristic Impedance," Proc. IEE, *113* (February 1966), pp. 263–70.
33. F. A. Benson and J. D. Last, "Nonlinear-Transmission-Line Harmonic Generator," Proc. IEE, *112* (April 1965), pp. 635–43.
34. R. Hirota and K. Suzuki, "Studies and Lattice Solitons by Using Electrical Networks," J. Phys. Soc. Jap., *28* (May 1970), pp. 1366–7.
35. R. Hirota and K. Suzuki, "Theoretical and Experimental Studies of Lattice Solitons in Nonlinear Lumped Networks," Proc. IEEE, *61* (October 1973), pp. 1483–91.
36. A. Noguchii, "Solitons in a Nonlinear Transmission Line," Electron. Commun. Jap., *57-A* (February 1974), pp. 9–13.
37. J. Kolosick et al., "Experimental Study of Solitary Waves in a Nonlinear Transmission Line," Appl. Phys., *2* (September 1973), pp. 129–31.
38. J. Kolosick et al., "Properties of Solitary Waves as Observed on a Nonlinear Dispersive Transmission Line," Proc. IEEE, *62* (May 1974), pp. 578–81.
39. D. Jäger, "Soliton Propagation Along Periodic-Loaded Transmission Line," Appl. Phys., *16* (1978), p. 36.
40. N. J. Zabusky and M. D. Kruskal, "Interaction of Solitons in a Collisionless Plasma and the Recurrence of Initial States," Phys. Rev. Lett., *15* (August 1965), pp. 240–3.
41. D. L. Landt et al., "An Experimental Simulation of Waves in Plasmas," Amer. J. Phys., *40* (October 1972), pp. 1493–7.
42. D. Jäger and F. J. Tegude, "Nonlinear Wave Propagation Along a Periodic-Loaded Transmission Line," Appl. Phys., *15* (April 1978), pp. 393–7.
43. A. C. Scott, "A Nonlinear Klein-Gordon Equation," Amer. J. Phys., *37* (January 1969), pp. 52–61.

44. K. Suzuki, R. Hirota, and K. Yoshikawa, "The Properties of Phase Modulated Soliton Trains," Jap. J. Appl. Phys., *12* (March 1973), pp. 361–5.
45. K. Suzuki, R. Hirota, and K. Yoshikawa, "Amplitude-Modulated Soliton Trains and Coding-Decoding Applications," Int. J. Electron., *34*, No. 6 (1973), pp. 777–84.
46. P. L. Chu and T. Whitbread, "Application of Solitons to Communication System," Electron. Lett., *14* (August 1978), pp. 531–2.
47. V. I. Karpman and E. M. Krushkal, "Modulated Waves in Nonlinear Dispersive Media," Sov. Phys. JETP, *28* (February 1969), pp. 277–81.

AUTHOR

George E. Peterson, B.S. (Physics), 1956, Ph.D. (Solid State Physics), 1961, University of Pittsburgh; AT&T Bell Laboratories, 1961—. At AT&T Bell Laboratories, Mr. Peterson initially was engaged in studies on low-noise amplifiers. He then studied laser crystals, nonlinear optic materials, and glass structure. Presently he is studying propagation of light in optical waveguides. Member, American Physical Society, American Ceramic Society, Society for Glass Technology, and the America Crystallographic Association.

AT&T Bell Laboratories Technical Journal
Vol. 63, No. 6, July–August 1984
Printed in U.S.A.

800-MHz Attenuation Measured In and Around Suburban Houses

By D. C. COX,* R. R. MURRAY,* and A. W. NORRIS†

(Manuscript received December 1, 1983)

The signal levels around and within eight suburban houses were measured at 800 MHz. These measurements are needed in refining the requirements for portable-radio communication systems that can accommodate low-power radiotelephone sets. The measurements were made from an instrumentation van having an erectable 27-foot-high antenna. Large-scale distributions of the small-scale signal medians are approximately log normal. The decrease in median signal level with distance ranges from d^{-3} to $d^{-6.2}$ for the eight houses. Signal decreases as $d^{-4.5}$ for the overall data set. At 1000 feet, regressions to signal levels range from 12.5 to 37.1 dB below free-space propagation levels for locations outside and locations inside on first and second floors. In basements, regression levels at 1000 feet range from 29 to 48.2 dB below free space. For the overall data set, regression signal levels at 1000 feet are 27.7 dB below free space. For all the basements, this value is 39.6 dB. Other signal statistics are given in this paper.

I. INTRODUCTION

Portable radiotelephones that are small, sophisticated, and low power are feasible because of advances in solid-state integrated-circuit technology. The performance of systems that operate with such radiotelephones strongly depends on the attenuation of radio signals propagating into buildings. Portable radiotelephone systems may operate at frequencies near 800 MHz.

* AT&T Bell Laboratories; present affiliation Bell Communications Research, Inc., † AT&T Bell Laboratories.

Copyright © 1984 AT&T. Photo reproduction for noncommercial use is permitted without payment of royalty provided that each reproduction is done without alteration and that the Journal reference and copyright notice are included on the first page. The title and abstract, but no other portions, of this paper may be copied or distributed royalty free by computer-based and other information-service systems without further permission. Permission to reproduce or republish any other portion of this paper must be obtained from the Editor.

Suburban residential areas, characterized by discrete houses with densities ranging from less than one house per acre to several houses per acre, comprise an important environment for portable radiotelephones. In the residential environment, fixed radio terminals that communicate with portable handsets could be placed outside houses at convenient locations. Such fixed terminals are referred to as portable radiotelephone terminals (PORTs).

Measurements of attenuation in and around three small buildings and a house were described in an earlier paper.[1] This paper describes attenuation measured in and around eight suburban houses. The measurements were made from an instrumentation van parked at different locations ranging from 250 to 2500 feet from the houses. A 27-foot-high erectable antenna on the van simulated an unobtrusive PORT antenna. Signal levels were received and recorded in the van from a portable signal source moved in and around the houses. Figure 1 depicts the measurement configuration.

Section II of this paper describes the instrumentation and measurement procedures. Section III contains the statistical results from the measurements.

II. THE EXPERIMENT

2.1 Instrumentation

2.1.1 Signal source

The portable signal source is the transmit section of a modified 815-MHz* handie-talkie. The transmitting antenna is a half-wavelength coaxial sleeve dipole attached to the top of the hand-held unit. Dc power is provided by a self-contained nickel-cadmium battery through a series voltage regulator. The regulator minimizes the output power drift due to normal battery discharge. The transmitter output is 0.8 watt. The output varies less than 0.3 dB and 700 Hz over continuous 1-hour periods that include ambient temperature changes of 0°C to 25°C.

2.1.2 Instrumentation van

The instrumentation van (movable PORT) is a modified motor home, containing a 5-kW ac generator. An uninterruptible power supply isolates the instrumentation from generator voltage fluctuations that otherwise could affect measurement accuracy. The van is shown in Fig. 2.

Two 27-foot antenna masts are installed in pivoting mounts so they

* The actual frequency of the measurements is 815 MHz; however, the statistical results are not sensitive to small changes in frequency. Therefore, when frequency is referred to relative to the measurements, it will be rounded to 800 MHz.

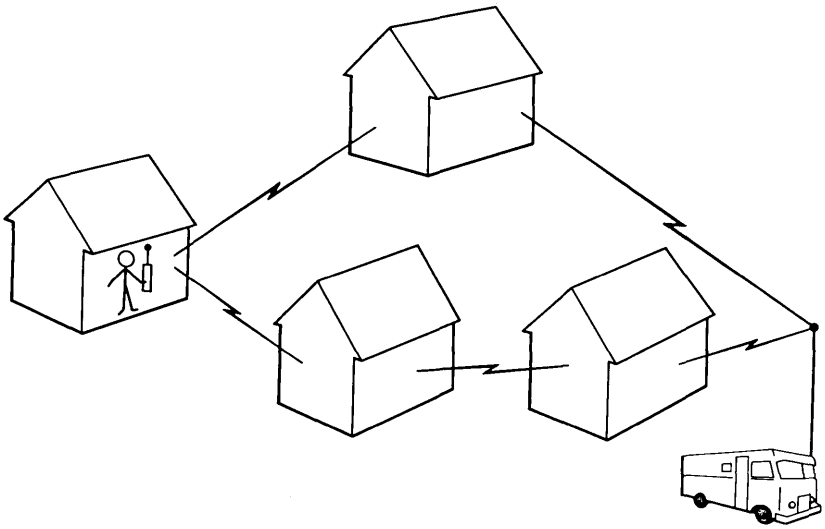

Fig. 1—Pictorial representation of the measurements.

can be stored horizontally for transport and easily erected at the test site. They are 14.2 feet apart and are adjusted to vertical using built-in bubble levels. An 815-MHz collinear receiving antenna is mounted on one mast. A bracket on the other mast holds the 815-MHz signal source at the same height to provide a reference signal for calibration purposes. The centers of the two antennas are at the same height when erected.

2.1.3 Measuring receiver

The measuring receiver is an 815-MHz FM communications receiver modified to detect the received signal envelope. The receiving antenna is a collinear array (4 dipole elements, 5.8-dB gain over dipole, 18-degree vertical beamwidth) mounted vertically at the top of the tilt-over mast on the instrumentation van. In the receiver modification, as shown in Fig. 3, an 11.7-MHz Intermediate Frequency (IF) output is extracted before the limiter, converted down to 13 kHz, bandpass filtered (BW_{3dB} = 8 kHz), and linearly detected. Figure 4 shows the modified receiver input/output characteristics. The modified receiver has a −123 dBm sensitivity for 0-dB output signal-to-noise ratio (s/n) from the linear envelope detector and a 45-dB measuring range between levels 6 dB above the noise level and 3 dB below saturation. This characteristic is linear within ± 1 dB over 35 dB. The input/output characteristics were measured before and after the field measurements to show the long-term variations in receiver performance. The standard deviation of the receiver noise level is also shown. The

Fig. 2—The instrumentation van with the receiving antenna mast and the reference signal mast erected. The center of the four-element collinear receiving antenna is 27 feet above ground at the top of the mast mounted on the right side of the van near the front. The signal source is at the top of its reference mast mounted on the left side near the rear. The center of the signal-source dipole is also 27 feet above ground.

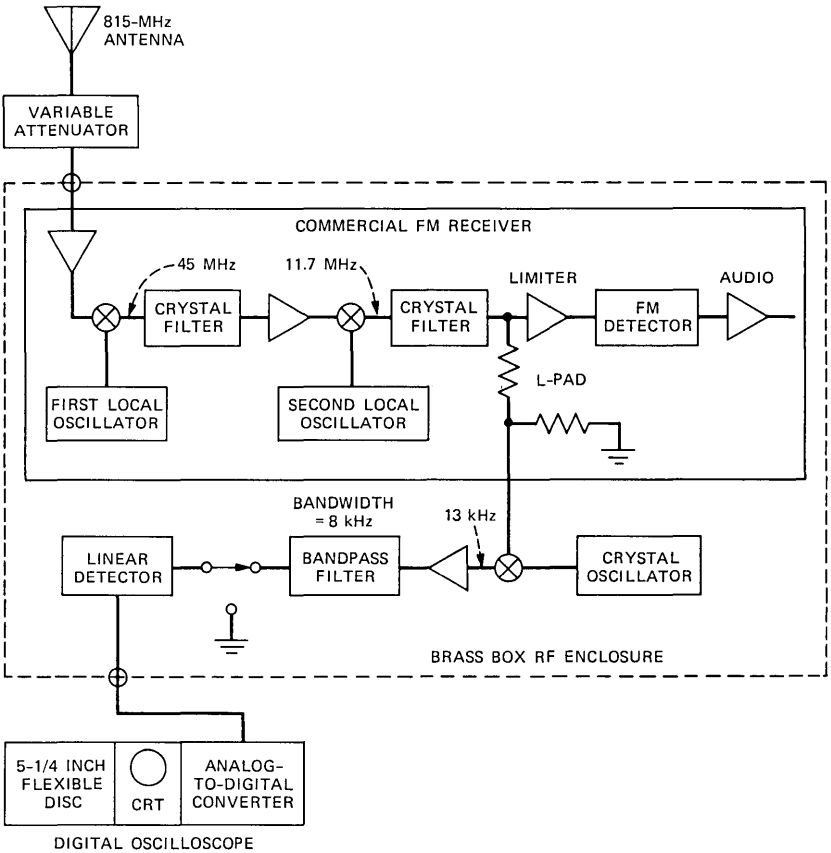

Fig. 3—Block diagram of the measuring receiver illustrating the modification to the commercial FM receiver. Also shown is the storage oscilloscope with the integral flexible-disk drive used for data acquisition.

entire receiver is enclosed in a sealed brass box to provide Radio Frequency (RF) isolation. A variable RF attenuator (see Fig. 3) reduces the input signal level in 1-dB steps to prevent overloading of the receiver.

2.1.4 Data acquisition

The analog receiver output drives a 12-bit resolution digital-storage oscilloscope and an integral 5-1/4 inch flexible disc drive for data storage. The oscilloscope is set to record 2048 samples in a 20-second measurement period. On each disc are recorded 16 tracks of 2048 samples each. Data for each parked position of the van, i.e., one PORT location, are stored on a separate disc.

The recorded data are transferred to a desktop computer. At the

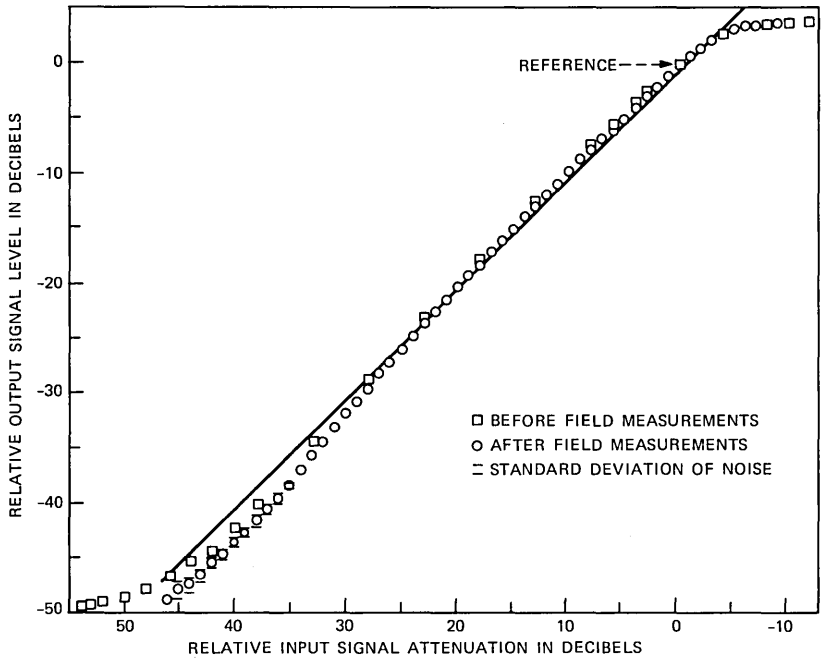

Fig. 4—Input-to-output characteristic of the modified receiver. The data from after the field measurements include the analog-to-digital conversion in the digital-storage oscilloscope. The data from before the field measurements were measured with an analog voltmeter at the output of the linear detector.

time of transfer the following steps are performed: (1) Hand-recorded log information is appended to the signal-strength data. The log information includes such items as the address of the house, the position of the van, the path azimuth, the path length, and the received input attenuator setting. (2) The data are scaled to convert the recorded signal voltages to decibels relative to 0 dB at the reference location 14.2 feet from the receiving antenna. The scaling takes into account recorded dc offsets, recorded reference levels and the received input attenuator settings. (3) Medians and cumulative distributions of signal level are calculated from the scaled data. (4) The scaled data are stored on flexible discs within the computer for further analysis.

2.2 Signal reference

For calibration purposes, both pivoting masts on the instrumentation van are used. The received signal level from the source at the reference distance is used as a calibration level to which all subsequent data measurements are referenced. The distance represents a realistic compromise between near-field antenna interactions and physical limitations on reference mast mounting.

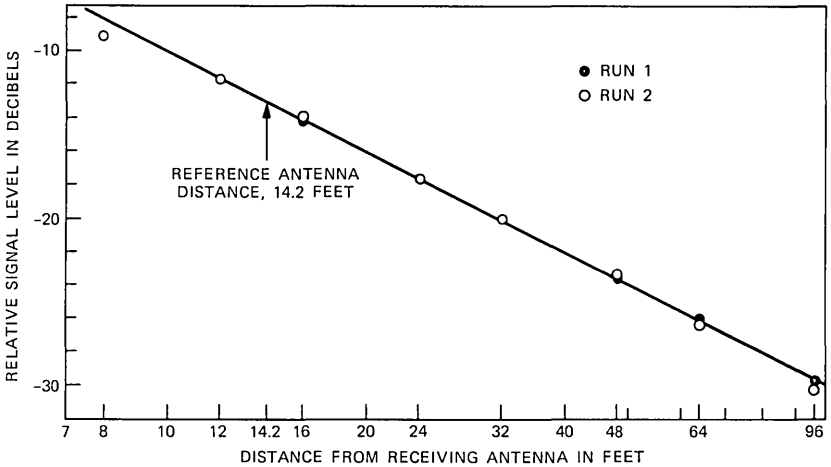

Fig. 5—Relative received signal level as a function of distance, d, between the signal source on top of a building and the receiving antenna mounted on the 27-foot van mast shown in Fig. 2. The measurements were made in an open area free of obstructions.

Relative ratio of signal level to distance from the receiving antenna is plotted in Fig. 5. The van with the receiving antenna erected was moved away from a fixed point supporting the signal source. Both antennas were at the same height. At the reference antenna distance, the received signal decreases at the $1/d^2$ rate of free-space propagation. The rate of change of the signal departs from $1/d^2$ at shorter distances because of near-field effects. At longer distances, ground reflection becomes significant.

2.3 Procedure

Van locations were selected using tax maps covering the immediate vicinity of the houses. Points were chosen approximately equally spaced in azimuth around each house for each of three radii at about 400, 800, and 1600 feet. Road layout and terrain irregularities influenced the final choices of vehicle placement.

Measurements were coordinated between the van and the measurement location over a 450-MHz voice link. The voice link comprises a 25-watt FM transceiver in the van and a 2-watt handie-talkie carried by the person making the measurements.

A typical procedure for measuring a house starts with the van parked at an appropriate position. The van location must be fairly level. If necessary, wooden ramps are put under wheels to aid in leveling. The portable transmitter is installed on its mast as a local reference source. The mast is erected and is plumbed to vertical. Similarly, the receiving antenna on the opposite side of the vehicle is erected and plumbed. Keeping both masts plumbed on the level van assures a fixed distance

between the reference and receiving antennas for calibration purposes. The linear detector Intermediate Frequency (IF) input is grounded, and the dc level is adjusted and recorded on a disc track. Next, the detector input is ungrounded and the receiver RF attenuator is adjusted so the RF reference level is within the receiver operating range. This level, which serves as a calibration reference at the fixed 14.2-foot distance, is then recorded.

The signal source is removed from the mast and taken to the house for signal level measurements. The unit is hand-held[2] at arm's length for a scan height of 4.5 feet. At a selected location either outside or within the house, a 20-second raster scan[2] is made by moving the transmitter in a horizontal plane at 2.5 ft/s. The 4-foot-square scanned area consists of 12 parallel linear scans separated by 4-inch increments. During the scan period, 2048 data points are taken at a rate of 100 samples per second.

During that period, the oscilloscope is monitored to see that signal amplitudes are within the receiver operating range. If they are not, the RF input attenuation is adjusted and the scan is repeated. The remaining locations within the house and immediately outside are similarly scanned and recorded. Upon completion of the measurements, the transmitter is reinstalled on the reference mast, erected and plumbed, and the dc level and RF-signal reference level are again recorded. The closure error between beginning and ending reference-level recordings is usually less than 0.5 dB. If the closure error exceeds 1 dB, the measurements are repeated. Such high closure error occasionally occurs when the transmitter battery has discharged below the regulation limit of the voltage regulator.

2.4 Received signal characteristics and definitions

Motion of the continuous wave (CW) signal source through the 4-foot-square areas inside and outside of houses results in small-scale signal variations. The variations are caused by multipath propagation.[2,3] Inside houses and in areas shadowed from the van, where propagation is dominated by reflection and scattering, the variations in the received signal envelope are approximately Rayleigh distributed.[1,2,4,5] Received signal minima are separated by the order of one-half wavelength.[2] The medians (or means) of these small-scale variations are approximately stationary over the small areas, but the medians for areas in different rooms in a house or in different houses can be significantly different. Thus, the signal statistics can be modeled as a combination of a small-scale quasi-stationary process (multipath) superimposed on a large-scale process (shadowing). This model is like the models used for mobile radio propagation.[3,6]

The received signal $y_c(t)$ can be represented as

$$y_c(t) = L(t)R(t)e^{j\omega_c t + j\phi(t)}, \tag{1}$$

where $\omega_c = 2\pi \times 815$ MHz and t is time. Since a number of paths that are many wavelengths long are involved, as in mobile radio, it is reasonable to expect any value of $\phi(t)$ to be equally likely, i.e., $\phi(t)$ is uniformly distributed from 0 to 2π.

The envelope $R(t)$ is Rayleigh distributed with a stationary mean (or median) over small-scale areas. The median of $R(t)$ is normalized to unity.[1,2,4,5] From Ref. 1, small areas for which $R(t)$ departs significantly from Rayleigh are those with strong signal, often with no houses between the van and the measurement areas. These are areas for which $L(t)$ is large. However, low signals are the ones that limit radio system performance and are thus of most concern. Therefore, departures from Rayleigh for large signal areas will not affect the accuracy of the model for most system-analysis applications.

The large-scale random variable $L(t)$ varies from room to room, from house to house and from van location to van location. Reference 1 and Section III show that the distribution of the random variable $U(t)$, defined by

$$U(t) = 10 \log_{10} L^2(t), \tag{2}$$

can be approximated by a Gaussian (normal) distribution for most random collections of small areas; that is, $L(t)$ is log-normally distributed. Thus, the probability density of $U(t)$ is

$$f_U(u) = \frac{1}{\sigma\sqrt{2\pi}} \exp[-(u - m)^2/2\sigma^2], \tag{3}$$

where the standard deviation, σ, is in decibels. Reference 1 and Section III also show that the mean, m, varies with distance, d, between the van and the small area as

$$m \propto 10 \log_{10}(d^n), \tag{4}$$

where n is the distance dependence exponent.

Only a single parameter is needed to describe the small-scale Rayleigh-distributed signal variation. The median can be determined if somewhat over half of the samples are above the measurement threshold. The mean, however, is biased by the receiver noise level unless significantly more than half the samples are above the threshold. Therefore, medians of received signal variations for the 4-foot-square areas characterize the small-scale signal variations at different measurement locations. The lowest median signal measured was 17 dB above the receiver noise level for the data presented in Section III. The second- and third-lowest median signals measured were 19 dB

and 19.5 dB above the receiver noise. All other medians were more than 20 dB above, with most around 40 dB above the noise.

III. THE MEASUREMENT RESULTS

3.1 Measurement areas

Characteristics of the houses measured are summarized in Table I. A brief description of the houses follows.

Figure 6 shows the first house, on Rambling Brook Drive. It is a 2-story English Tudor style with a full basement. The house is centrally located on a level 250- by 200-foot lot. House densities in this area are generally one per acre. This house is 5 years old, has aluminum siding on three sides, and has nonmetallic composition siding on the front. Aluminum combination storm window and screens are on all window and door openings. The metal screen covers only one-half of the area of each window opening. This house has full, foil-backed insulation in the walls. Outside this house are numerous low foundation trees. There is a dense row of 15-foot-high evergreens along the west property line, and a few large trees within an 800-foot radius. These measurements were made in April 1982.

Figure 7 shows the second house, on Winding Brook Way. It is located on a slightly raised mound on a 1-acre lot. It is a bilevel ranch house. The basement is half above ground and is part of the living area. The house has all wood siding and nonmetallic wall insulation. House densities in this area are one per acre. This house is 15 years old. Most trees and plantings in this area are the same age. The foundation plantings are medium density, with the exception of several large evergreens on the corners and in the rear near the property line. Metal screening covers all the window openings halfway. These measurements were made in May 1982.

House number 3, on Valley Point Drive, and shown in Fig. 8, is a very large, new, 2-story colonial with vinyl siding covering foil-faced sheathing. All windows are full-metal screened with the exception of sliding glass doors located in the rear. This house has a full concrete block basement and is located on a mostly level 1-acre lot. There are very large trees completely covering the rear property line, which drops off sharply into a ravine. The ravine is filled with large trees. All other houses in this area, although different in style, are constructed on 1-acre lots. For the most part, there are very few trees, except for the dense woods running behind the house and adjacent houses. These measurements were made in late May to mid-June 1982.

Figure 9 shows the fourth house, on Courtland Lane. It is an L-shaped ranch house without a basement. It is on a 75- by 100-foot lot. All surrounding lots and houses are similar, with a housing density of

Table I—Characteristics of houses in study

House	Lot Size (ft)	House Densities in Area	Exterior-Side Material	Density of Foundation Plants	Large Shrubs or Trees in Area	Metal-Window Screening	Wall-Insulation Backing
Rambling Brook	250 by 200	1 per acre	3 aluminum 1 composition	Avg.	Few	Half	Foil
Winding Brook	200 by 200	1 per acre	Wood	Avg.	Avg.	Half	Paper
Valley Point Drive	200 by 200	1 per acre	Vinyl over foil	Avg.	Many in rear	Full*	Foil
Courtland Lane	75 by 100	5 per acre	3 asbestos 1 wood	Avg. to high	Avg.	Half	Paper
Alden Lane	175 by 250	1 per acre	All brick	Avg. to low	Few, some large	Half	Paper
Monmouth Ave.	100 by 200	0.5 to 2 per acre	All brick	Avg.	Few, very large	None	Metal lath under plaster
Tallen Drive	75 by 110	5 per acre	3 asbestos 1 wood/brick	Avg.	Few	Full	Paper
Rutledge Drive	50 by 150	1 to 5 per acre	All wood	Avg.	Few	Half	Unknown

* No metal screens on rear sliding doors.

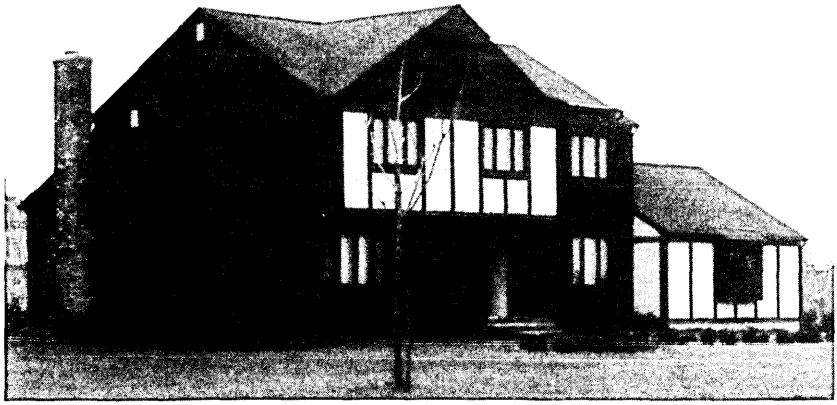

Fig. 6—The house on Rambling Brook Drive.

Fig. 7—The house on Winding Brook Way.

Fig. 8—The house on Valley Point Drive.

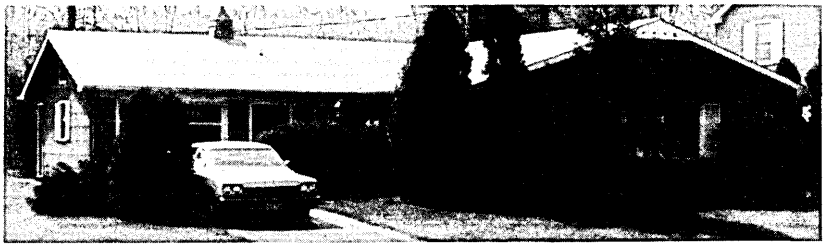

Fig. 9—The house on Courtland Lane.

Fig. 10—The house on Alden Lane.

about five per acre. This house has wood siding on the front and composition siding on three sides. Half of each window opening is covered with a metal screen. Wall insulation is nonfoil glass wool. There are some fairly large shrubs along the foundation and some medium-sized trees on the lot. These measurements were made in August 1982.

Figure 10 shows house number 5, on Alden Lane. It is an all-brick construction with a full basement. It is centrally located on a level lot. This house does not have foil-backed insulation and has metal half-screened windows throughout the house. It has two large, unscreened windows, one front and one rear. House densities in this area are generally one per acre. There are medium-height foundation plantings and some medium to large trees near the house. There is a large open area behind a 100-foot strip of heavy woods to the back. This strip is perpendicular to the lot. These measurements were made in late August to early September 1982.

Figure 11 shows house number 6, on Monmouth Ave. It is a large, all-brick, 2-story colonial with a full basement and is on a half-acre lot. This is an older house with metal-lath plaster walls. Vegetation density is medium around the house. The property has numerous large trees in the rear and one or two large trees in the front. Most streets in the area are tree-lined with older shade trees. This house has full-metal screening on its average-sized windows, but two very large front first-floor windows are unscreened. House densities in this area vary

Fig. 11—The house on Monmouth Avenue.

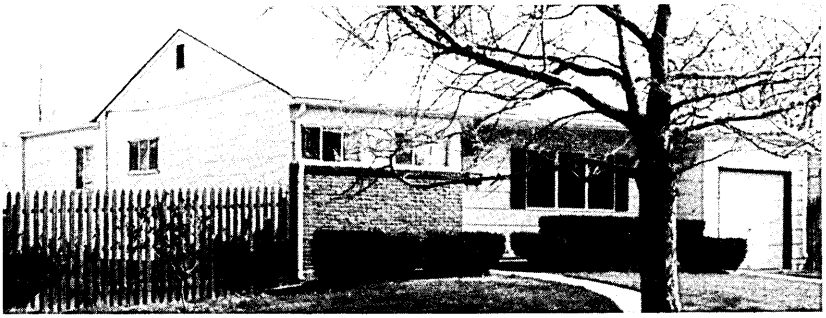

Fig. 12—The house on Tallen Drive.

considerably, but generally run from one-half to two per acre. These measurements were made in October 1982.

Figure 12 shows house 7, on Tallen Drive. It is located on a 75- by 110-foot lot in an area of homes that are all on quarter-acre lots. Siding on this house is wood and masonry on the front and asbestos on three sides. This house has full-metal screening on the front windows and partial screening on the few side windows. Wall insulation has no foil backing. Most of the foundation plantings are average-sized, and there are a few trees across the rear property line. The surrounding properties generally have a few medium-sized trees, which had just dropped their leaves. These measurements were made in mid-November 1982.

The last house measured, on Rutledge Drive, is shown in Fig. 13.

Fig. 13—The house on Rutledge Drive.

This is a very old house located on a 50- by 150-foot lot. It is a wood-sided 2-story colonial with a partial basement. Wall insulation material is unknown, but there are suggestions that the newer two-thirds of this house may have foil-backed insulation. Window sizes in this house are average and all are covered halfway with metal screening. House densities in this area are generally two or three per acre. This house has medium-to-large foundation plantings. It also has a few large trees on the property and in the area. There are two 30-foot evergreens, very dense, directly in front and a large wooden 2-car garage directly across the back of the house. These measurements were made in mid-December 1982 to January 1983.

3.2 Large-scale statistics of small-scale medians for individual houses

The data points in Figs. 14 through 21 are the medians of the measured signal envelopes from small-scale areas for each of the eight houses. That is, the data points are samples of the random variable $L(t)$ in eq. (1). Each data point represents the median level of 2048 samples of $R(t)$ taken within a 4-foot-square area at a particular location. The signal levels are in decibels relative to 0 dB at the van reference. The medians are plotted versus the distance between the van antenna and the area. Note that the independent variable, distance, is on the ordinate. The dotted line on each figure represents free-space (FS) propagation (d^{-2}) relative to 0 dB at the van reference. The measurement locations are outside (OS) the houses, in rooms on the first (1) and second (2) floors, and in the basements (B), as indicated by the different symbols on the figures. The outside locations are about 5 to 10 feet in front of the midpoints of the four outside walls of the houses.

A strong dependence of signal level on distance is evident in the data in all the figures. The straight lines, except for the free-space line, are linear-least-squares regression lines through the different groups of data as indicated. The regression lines are determined using distance as the independent variable. These lines are a good quantitative measure of the strong distance-dependent trends. The regression slopes yield the distance-dependence exponents, n, in eq. (4). One average of the median signal level for each grouping of data is given by the level at 1000 feet taken from each regression line. The distance-dependence exponents and the levels at 1000 feet are indicated on each figure. The exponents and the 1000-foot levels with the −37 dB free-space level removed are summarized in Table II.

Table II—Parameters for individual houses (vertically polarized, 27-foot antenna height)

Floor	Distance Exponent	1000 ft to Relative Free Space (dB)	1000-ft Building Attenuation (dB)	σ (dB)	F	No. of Points
Rambling Brook Drive						
OS*	−4.6	−12.5	—	8.8	51	35
1	−4.0	−18.6	6.1	7.3	54	36
2	−3.0	−16.6	4.1	4.8	54	27
B†	−3.2	−29.0	16.5	5.4	13	9
Winding Brook Way						
OS	−3.4	−20.7	—	6.2	55	40
1	−3.7	−24.0	3.3	5.4	42	20
2	−3.3	−21.4	0.7	6.0	55	40
Valley Point Drive						
OS	−5.3	−16.4	—	9.9	37	20
1	−6.2	−28.5	12.1	7.3	65	15
2	−5.7	−26.6	10.2	6.4	104	21
B	−5.5	−37.7	21.3	6.3	16	5
Courtland Lane						
OS	−6.1	−31.6	—	5.5	220	36
1	−6.0	−34.6	3.0	5.3	341	54
Alden Lane						
OS	−5.8	−32.7	—	6.0	260	40
1	−5.8	−37.1	4.4	6.6	251	50
B	−6.2	−48.2	15.5	5.0	89	10
Monmouth Avenue						
OS	−4.8	−27.6	—	5.5	115	36
1	−4.6	−32.9	5.3	6.7	34	18
2	−5.2	−35.4	7.8	6.3	77	27
B	−4.2	−42.6	15.0	6.0	16	9
Tallen Drive						
OS	−4.7	−27.7	—	5.1	165	40
1	−4.7	−30.5	2.8	4.6	202	40
B	−4.7	−39.7	12.0	4.1	121	20
Rutledge Drive						
OS	−4.1	−23.5	—	5.1	91	35
1	−4.2	−29.1	5.6	4.3	107	27
2	−3.8	−24.6	1.1	5.7	32	18
B	−4.3	−38.7	15.2	3.6	44	9

*OS = Outside.
†B = Basement.

An average attenuation at 1000 feet attributable to a building can be defined as the difference between the regression-line value outside and the regression-line value for the particular grouping of the data inside. For example, from Fig. 14 and Table II, the signal level outside at 1000 feet is −49.5 dB and the level inside for the first floor is −55.6 dB. Thus, the building attenuation for the first floor for the house on Rambling Brook Drive is 6.1 dB. Building attenuation values are also summarized in Table II.

After the regression-level trend values are subtracted from each data point in Figs. 14 through 21, there is still considerable scatter in the resulting signal-level residuals. The standard deviations, σ, of the residuals after removal of the trends are listed in Table II.

The distance dependences and signal levels are different for each floor of the same house and are significantly different between houses. Because of these differences and the considerable scatter in the data, it is reasonable to question whether the regression lines are meaningful or are only a manifestation of statistical fluctuation. This question is addressed in the next section.

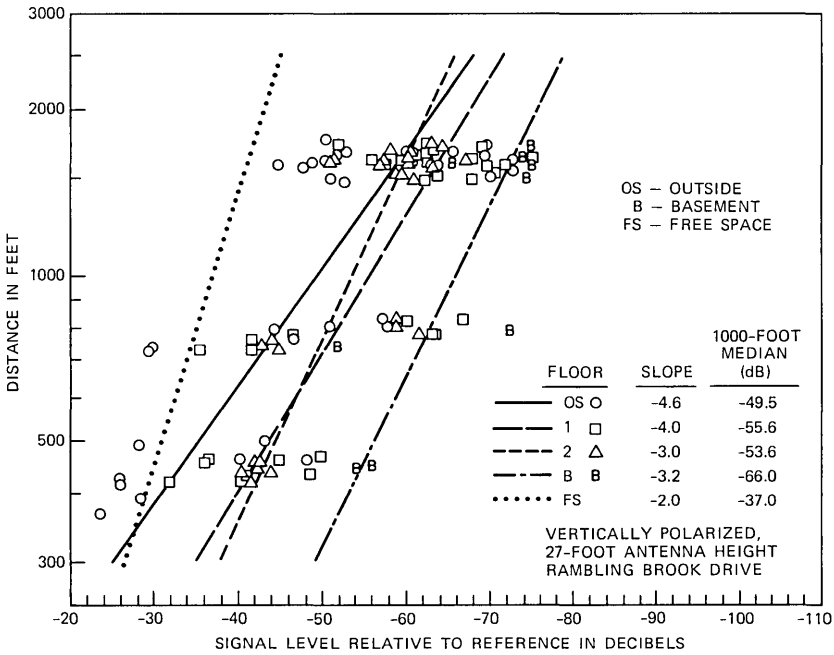

Fig. 14—Medians of the small-scale signal envelope variations for different measurement locations plotted versus distances between the locations and the van antenna. The locations are inside and outside a house on Rambling Brook Drive.

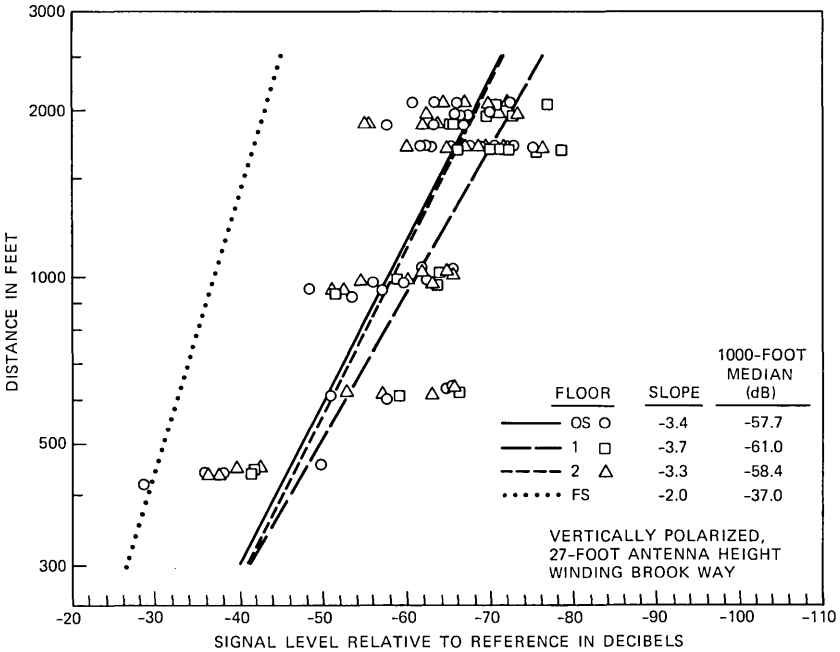

Fig. 15—Signal envelope medians and regression lines for the house on Winding Brook Way similar to those in Fig. 14.

3.2.1 Statistical significance

The statistical significance of the regression lines can be assessed using the well-known "F" test. The F values determined during the regression calculation indicate the likelihood that the line could be the result of statistical fluctuation in a sample of the same number of points taken from uncorrelated data, i.e., that the result is due to chance. In general, the larger the F number, the more significant the result. Also, for larger numbers of points, the result has the same significance at lower F numbers. Values of F and the number of data points (medians) included in the regression are also shown in Table II.

All of the F values in Table II have a very high degree of significance, except for three of the basements. The likelihood of the result being due to chance is much less than 0.1 percent for all but the three basement cases, i.e., they are significant at 0.1 percent or better. The results are significant at 0.5, 1, and 5 percent for the basements on Monmouth Avenue, Rambling Brook Drive, and Valley Point Drive, respectively. The lower significance for these three basements is largely due to the smaller number of measurements taken in them. Thus, in general the regression lines are statistically significant, that is, if more measurements were made in the same houses from different

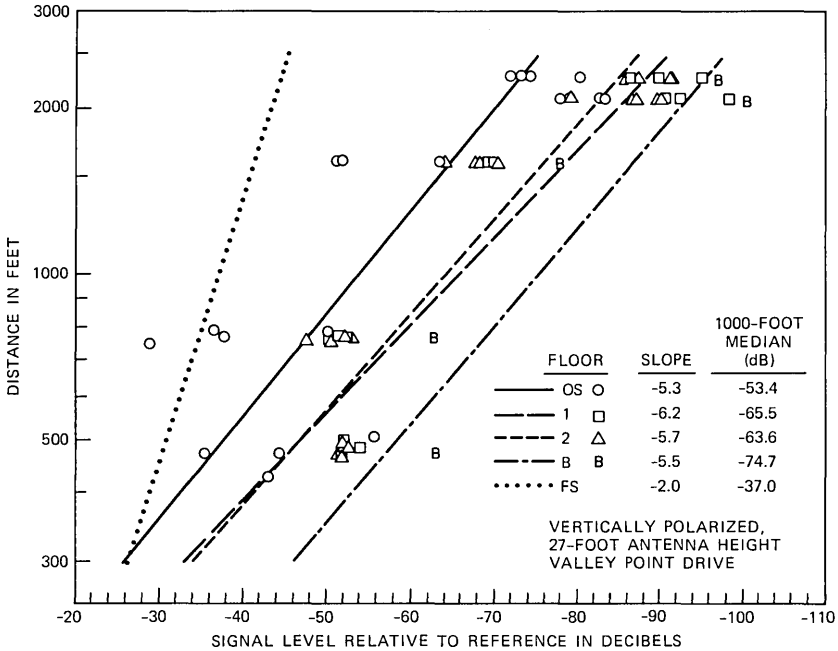

Fig. 16—Signal envelope medians and regression lines for the house on Valley Point Drive similar to those in Fig. 14.

van locations or in similar houses in similar areas, the regression lines would remain essentially the same. The differences in the parameters for the different houses must then result from actual differences in construction and in the environments around the houses. This situation indicates that the combined statistics from the eight houses will be nonhomogeneous and will depend on the number of measurements included from each kind of house and environment. It also indicates that portable-radiotelephone systems should have coverage-area sizes and possibly frequency-reuse factors tailored to fit the particular environments that are encountered. However, to make overall estimates of these system parameters, combined statistics for the eight houses are still useful.

3.2.2 The effect of the ground

Most of the distance-dependence exponents in Table II are less than −4. However, in free space the signal level would decrease as d^{-2}. Some of the additional rate of decrease can be accounted for by the presence of the ground.

For the distances involved here, the earth's curvature is negligible. At 800 MHz, the reflection coefficient phase is approximately 180 degrees for all polarizations for small angles between the propagation

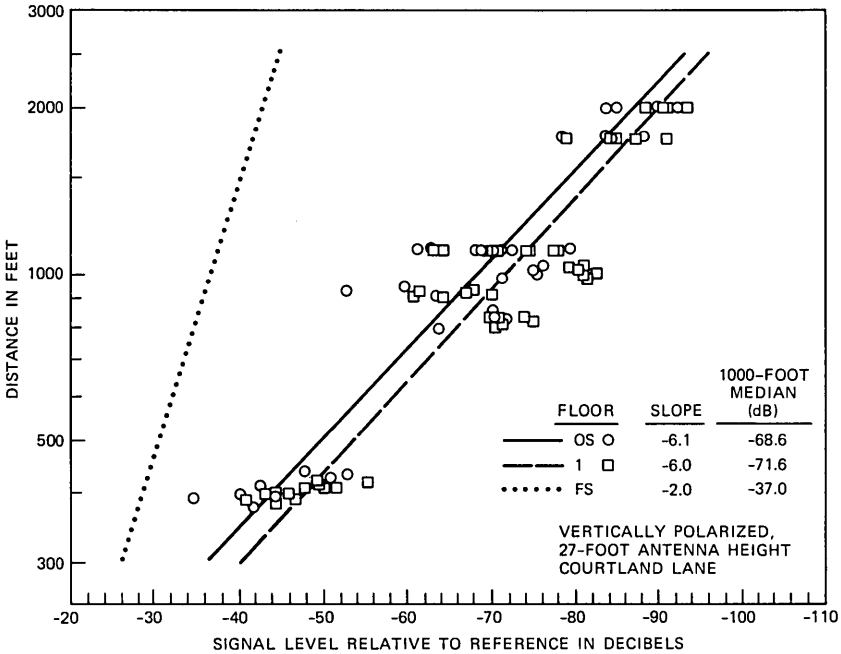

Fig. 17—Signal envelope medians and regression lines for the house on Courtland Lane similar to those in Fig. 14.

direction and the ground.[7] For propagation between two points separated a distance d and at heights h_r and h_t above flat ground, the field amplitude at one point E_r relative to the transmitted field amplitude E_t is given by[7]

$$\frac{E_r}{E_t} = \frac{2}{d} \sin \left[\frac{2\pi h_r h_t}{\lambda d} \right], \tag{5}$$

where λ is the wavelength. For large d, this approaches $E_r/E_t \; a \; d^{-2}$ or, for power, this becomes $P_r/P_t \; a \; d^{-4}$. The approximation d^{-4} is good for the parameters $h_t = 4.5$ feet, $h_r = 27$ feet, $d \gtrsim 1000$ feet, and a frequency of 800 MHz. These parameters are appropriate for the measurements outside houses and on some of the first floors. The effective exponent becomes a little greater than -4 for distances less than 1000 feet. For second floors and for short distances, not only does the approximation of the sine with its argument break down, but also the reflection coefficient angle may depart significantly from 180 degrees for some ground conditions.

All of the outside and first floor exponents in Table II are less than -4 except for one. The house on Winding Brook Way is a little higher than some of the surrounding ground. Thus, even its outside measure-

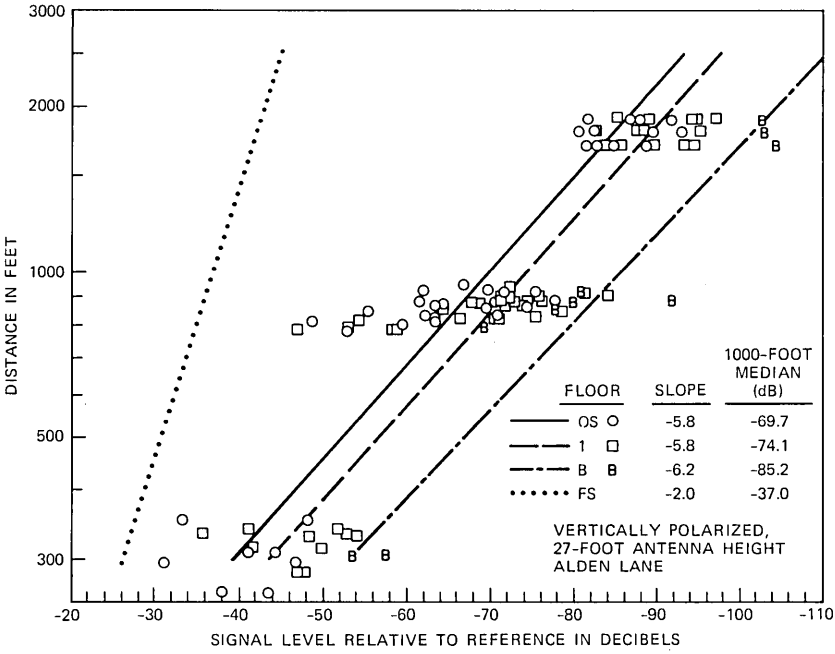

Fig. 18—Signal envelope medians and regression lines for the house on Alden Lane similar to those in Fig. 14.

ments could be more than 4.5 feet above ground. The first floor of this house is at ground level at the back side and underground at the front. For some directions, the first floor is more like a basement. Thus, the trends in the distance-dependence exponents for all the houses are consistent with the presence of the ground. The medians that are above the free-space level on some of the figures are also consistent with the presence of the ground. [Note the factor of 2, i.e., 6 dB, in eq. (5)]. The fact that some of the exponents are considerably less than −4 is probably due to the additional attenuation experienced in reflecting from and propagating through intervening houses and trees.

3.2.3 Discussion

From Table II and Figs. 14 through 21 it is evident that the attenuations into basements are significantly greater ($\approx$ 10 *dB*) than the attenuations into first and second floors. This suggests that, if basements are to be served by a portable radiotelephone system, the attenuations into basements will dominate the radio-link gain requirements.

Attenuations into the houses generally follow expectations based on the metallic content of the walls and other wall construction features. The house on Valley Point Drive, with aluminum foil in the walls and

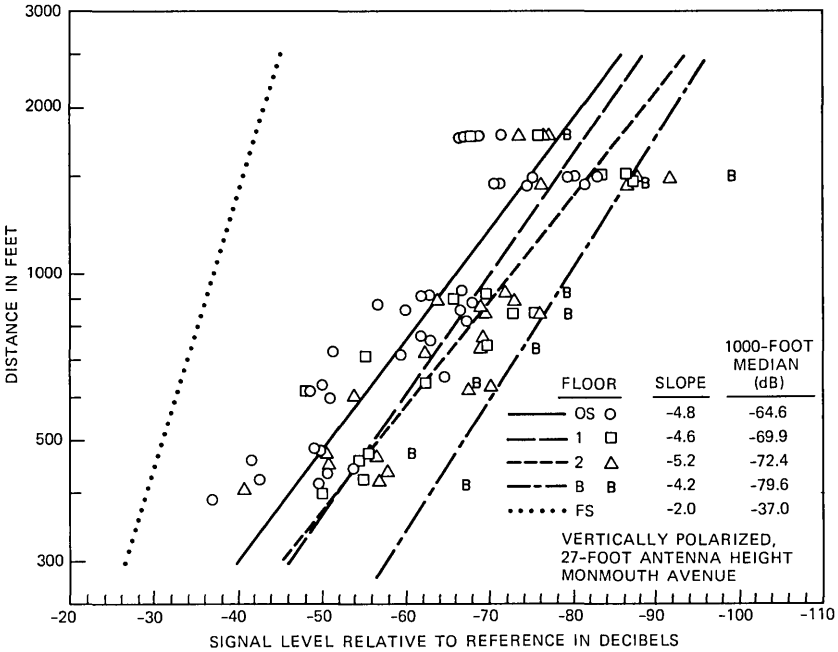

Fig. 19—Signal envelope medians and regression lines for the house on Monmouth Avenue similar to those in Fig. 14.

full metal screens, has the largest attenuations for all floors. The houses on Rambling Brook Drive, Rutledge Drive, and Monmouth Avenue form an attenuation grouping with about 6 dB less attenuation into the first floors. Two of these houses definitely have metal in their walls, with Rambling Brook having half metal screens, and Monmouth Avenue having full screens except for two very large, unscreened picture windows. Uncertainty in the construction of the older house on Rutledge Drive does not help in the attempt to explain its higher attenuation. The second-floor and basement attenuations generally follow the first-floor trends, except for the somewhat higher second-floor attenuation on Monmouth Avenue, and a somewhat higher basement attenuation on Alden Lane. All of the second-floor windows at the Monmouth Avenue address have full metal screens except for two unscreened windows in two sundeck doors. The Alden Lane basement appears to be lower in the ground than the other basements. These factors probably account for the higher attenuations. The attenuation for the first floor of the partially-screened brick house at Alden Lane is about midway between the attenuations for the metallic-walled houses and for the wooden- and composition-walled houses. The dense brick walls seem consistent with this observation. The three houses with wooden and composition walls on Winding Brook Way,

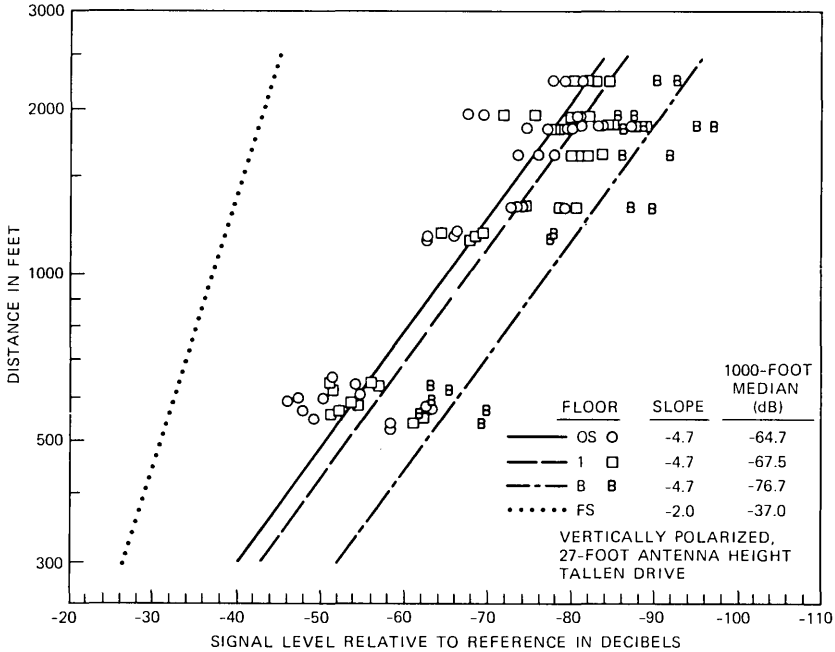

Fig. 20—Signal envelope medians and regression lines for the house on Tallen Drive similar to those in Fig. 14.

Courtland Lane, and Tallen Drive form a low attenuation group with only about 3-dB attenuation into the first floors. The second-floor attenuation on Winding Brook Way and the basement attenuation at Tallen Drive are also lower than the similar attenuations for the other houses.

The median signal levels at 1000 feet both outside and inside are not well correlated with the attenuations into the houses, i.e., with the differences between outside and inside levels. External environmental factors appear to affect the signal levels as much or more than the house constructions. For example, signal levels were lowest at Alden Lane, the brick house with only moderate attenuation. Signal levels were highest at Rambling Brook Drive, the second-highest attenuation house. The two houses in high-density housing areas, the Courtland Lane, and Tallen Drive locations, have low-signal levels. The houses with the higher-signal levels are generally in the least dense housing areas that are not heavily wooded. The significance of these general trends is difficult to assess with a small sample of eight quite different housing environments. It appears reasonable, however, that attenuation would be greater (signal levels lower) for propagation through areas with greater house densities.

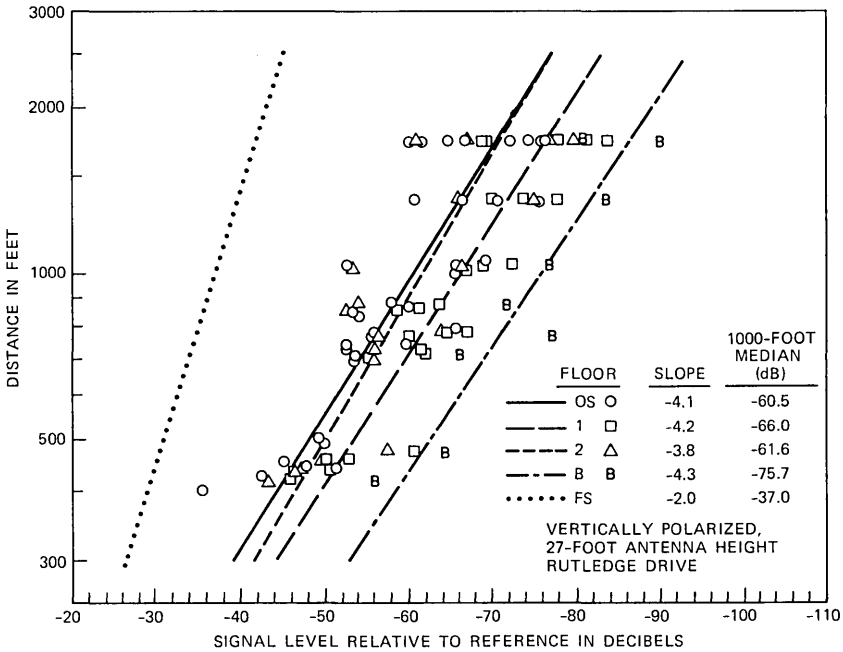

Fig. 21—Signal envelope medians and regression lines for the house on Rutledge Drive similar to those in Fig. 14.

3.3 Large-scale statistics of small-scale medians for all eight houses for different groupings of the data

3.3.1 Parameters for groupings by floors

The signal medians and distances from Figs. 14 through 21 are combined and separated into groups for outside, first floors, second floors, and basements in Figs. 22 through 25. Each symbol of these figures represents data from one of the houses, as indicated in Table III. The straight solid lines are the least-squares regression lines for all the data on a given figure. The longer dashed lines are regression lines for all the data between distances of 250 and 1250 feet. Similarly, the shorter dashed lines are regression lines for all the data between distances of 690 and 2300 feet. The dotted lines are, again, free-space lines. A regression for all the first- and second-floor data for all distances, i.e., from 250 to 2300 feet, is plotted as a long and short dashed line and a dashed and dotted line on Figs. 23 and 24 for comparison with the line for the individual floors. The nonhomogeneity of the data discussed in Section III is evident in Figs. 22 through 25.

The distance-dependence exponents, the signal levels at 1000 feet and the building attenuation at 1000 feet are listed in Table IV for the

Table III—Symbol legend for Figs. 22 through 25

Symbol	House under test
○	Rambling Brook Drive
□	Winding Brook Way
△	Valley Point Drive
*	Courtland Lane
●	Alden Lane
■	Monmouth Avenue
▲	Tallen Drive
+	Rutledge Drive

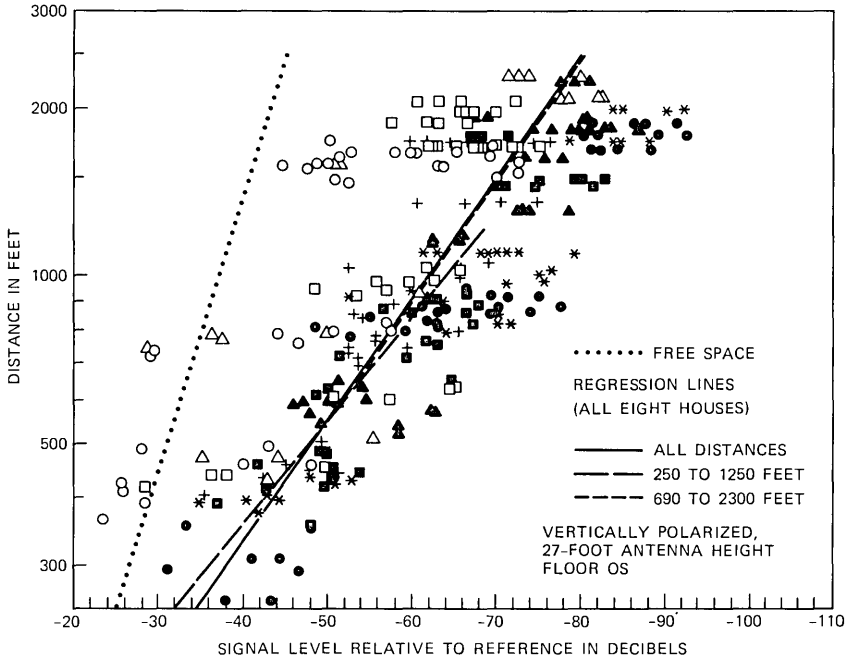

Fig. 22—Medians of the small-scale signal envelope variations for different measurement locations plotted versus distances between the locations and the van antenna. The locations are outside of the eight houses. Signal levels are with respect to 0 dB at the signal reference. Regression lines are drawn for all the outside data from all eight houses for all distances and for two subsets of the outside data.

regression lines in Figs. 22 through 25. The small negative values for building attenuation at 1000 feet for the second floors merely indicate that the average of the median signal levels for the second floors were slightly larger than the average of the levels outside at 4.5 feet above ground. This is reasonable since the second floors are less obstructed by intervening houses and are affected somewhat differently by the ground [see eq.(5)]. The F parameter and number of data points in

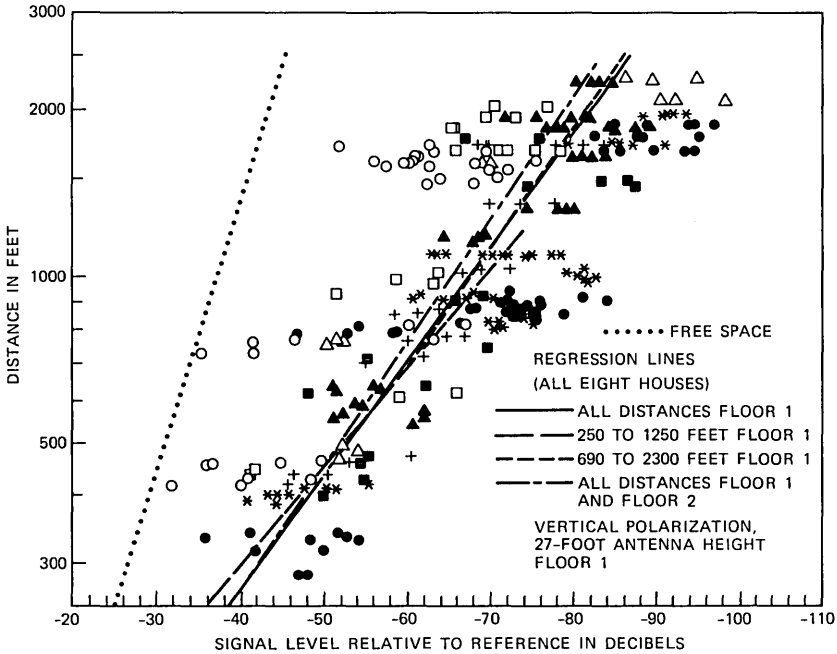

Fig. 23—Signal envelope medians and regression lines for the data from the first floors for all eight houses similar to those in Fig. 22. In addition, the regression line is included for all the first- and second-floor data combined.

each regression are also listed in the table. For these data groupings by floors, the regression is significant well below the 0.1-percent level readily available in F tables.[8] Thus, even though the data sets are nonhomogeneous, the regressions to the data appear very good. Table IV also includes the standard deviations, σ, of the residual signal levels after subtracting out the regression-line values at the same distances, i.e., after removing the trends.

All the signal medians for all houses and all floors (including outside data) are plotted in Fig. 26. Because of the high density of points, no attempt has been made to separate any of the data groupings in that figure. The solid regression line is for all the data. The dashed line is for all of the floors for distances between 250 and 1250 feet. The regression line for all floors and for distances between 690 and 2300 feet is indistinguishable from the solid line for all the data. Parameters for all the floors combined are also listed in Table IV. The F values for these data groupings are also significant well below 0.1 percent.

The distance-dependence exponents are generally less than −4 and range down to −5.5. The overall value for all the data is −4.5. In general, for all the groupings by floors, the signal levels decrease faster with distance for the first few hundred feet than for the greater

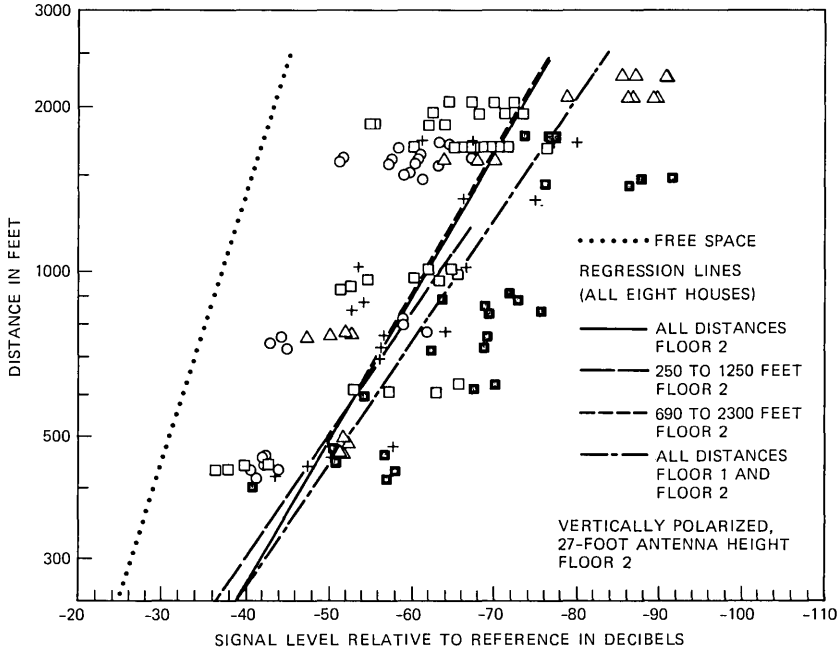

Fig. 24—Signal envelope medians and regression lines for the data from the second floors for the five houses that have second floors. The figure is similar to Fig. 22. In addition, the regression line is included from Fig. 23 for all the first- and second-floor data combined.

distances. This is reasonable since there are few, if any, intervening houses and trees in the first few hundred feet from a house. After several hundred feet there are many intervening houses and trees.

It is evident from Table IV and also generally from Table II that the signal levels and building attenuations for the various floors are different. As we discussed earlier, the second floors generally experience higher signal levels and lower attenuations than the first floors. The basements experience much lower signal levels and much higher attenuations than first floors. In fact, the basement attenuation is so much greater that basements will probably need to be treated separately in considering portable-radio-system performance.

The standard deviations of the residual signal levels are generally between 7.5 dB and 10.5 dB for the groupings in Table IV. The purpose of removing the trends for the data groupings is to reduce the standard deviations of the scatter in the signal levels, and thus, to permit tighter estimates of system performance. In general, removal of the regression line trends from these groupings significantly reduces the standard deviations. For example, before the trend is removed from the group containing all the data, the standard deviation was 14.9 dB. After removal of the trend it is the 10 dB listed in Table IV. This significant

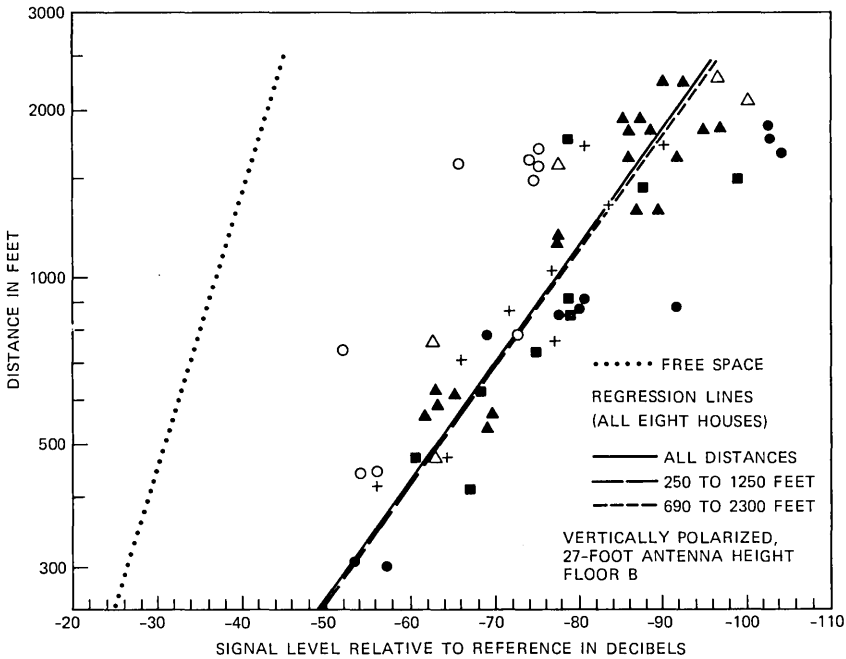

Fig. 25—Signal envelope medians and regression lines for the data from the basements for the six houses that have basements. The figure is similar to Fig. 22.

reduction in standard deviation is essentially the fact indicated by high significance of the F parameter.

3.3.2 Cumulative distributions for different floors and distance groupings

The solid lines in Figs. 27 through 30 are the cumulative distributions of the residuals for all houses and all distances for the floor groupings indicated. The residuals are the levels remaining when the regression-line trends are removed from the signal medians, as we discussed earlier.

Also plotted in Figs. 27 through 30 are distributions for two other distance groupings of the data. These other two groupings contain the residuals for the shortest distances, i.e., between 250 feet and 690 feet, and for the longest distances, i.e., between 1250 feet and 2300 feet. For these distance groupings, and for the intermediate distances of 690 feet to 1250 feet, the distance-dependence trends removed were those trends determined for all distances for the appropriate floor groupings. That is, the trends removed were the solid lines on Figs. 22, 25, and 26 for outside, for basements and for all data and the dashed and dotted lines on Figs. 23 and 24 for first and second floors combined. The straight lines drawn on Figs. 27 through 30 represent log-normal distributions having the standard deviations of the various

Table IV—Parameters for all eight houses (vertically polarized, 27-ft antenna height)

Floor	Distance Exponent	1000 ft Relative to Free Space (dB)	1000-ft Building Attenuation (dB)	σ (dB)	F	No. of Points
All Distances						
OS	−4.5	−24.4	—	9.4	381	282
1	−4.8	−30.2	5.8	8.7	463	260
2	−3.7	−24.5	0.1	9.0	126	132
B	−4.6	−39.6	15.2	7.6	129	62
1 and 2	−4.4	−28.2	3.8	9.3	504	392
OS, 1, 2, B	−4.5	−27.7	3.3	10.0	844	736
250 to 1250 ft						
OS	−5.6	−27.0	—	8.4	179	158
1	−5.5	−32.0	5.0	7.6	217	153
2	−4.4	−26.0	−1.0	7.6	39	66
B	−4.7	−40.0	13.0	6.0	44	33
1 and 2	−5.3	−30.5	3.5	7.8	247	219
OS, 1, 2, B	−5.3	−29.9	2.9	8.8	373	410
690 to 2300 ft						
OS	−4.2	−25.0	—	9.8	94	215
1	−4.5	−30.7	5.7	9.3	113	199
2	−3.8	−24.2	−0.8	9.5	39	101
B	−4.6	−39.7	14.7	8.5	33	46
1 and 2	−4.1	−28.7	3.7	10.0	124	300
OS, 1, 2, B	−4.2	−28.1	3.1	10.6	217	561

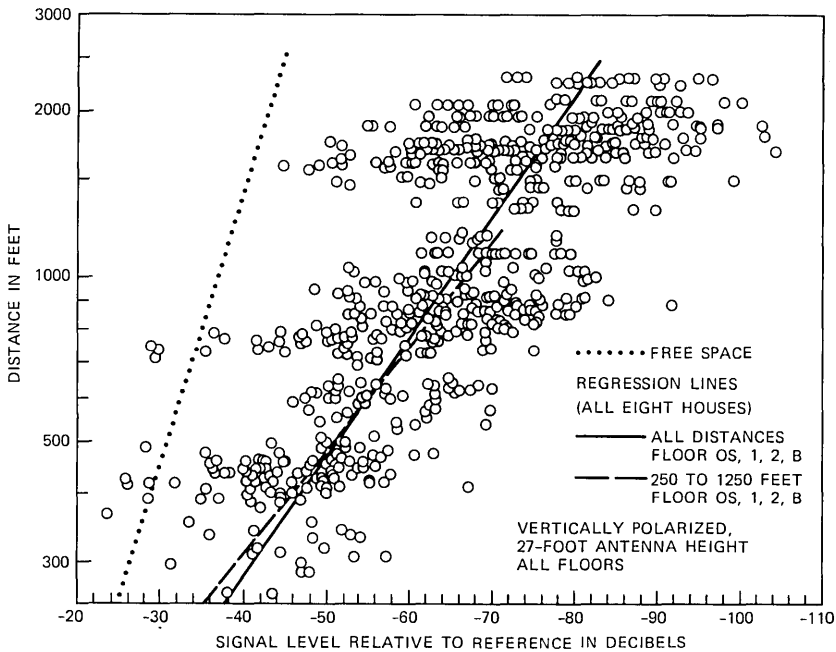

Fig. 26—Signal envelope medians and regression lines for all the data from all the houses for all the floors and outside combined. All the medians are plotted as "o" with no distinction as to house.

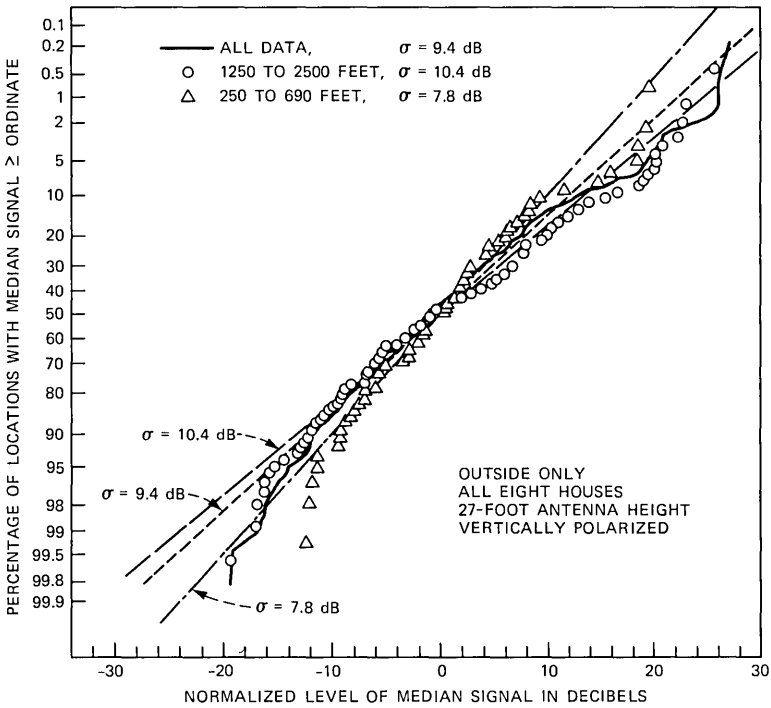

Fig. 27—Cumulative distributions of the medians of the small-scale signal envelope variations for outside locations after the trend values for the solid regression line in Fig. 22 are subtracted out.

data groupings. Standard deviations for the three distance groupings with the overall trends removed are listed in Table V.

The mean value will be zero for the residuals of a data set after removal of the regression trend for that particular data set. The mean of the residuals of a subset of a data set after removal of the trend of the entire set will not necessarily be zero. The closeness of the mean of the subset residuals to zero is an indication of how well the trend of the entire set represents the trend remaining in the subset. The means of the various distance groupings (subsets) after removal of the trend for all distances (sets) are also listed in Table V. Most of the means are less than 1 dB, with the largest being 1.5 dB. Considering the much larger standard deviations, these small means indicate that the overall trends are quite applicable to the distance groupings also.

The cumulative distributions of the measured data in Figs. 27 through 30 are all within ±2 dB of the associated log-normal distribution with the same standard deviation for the range from 10 percent to 90 percent. Most of the measured distributions are within ±1 dB over the 10-percent to 90-percent range. The fit of the measured distributions is worse in the tails, where statistical fluctuations are

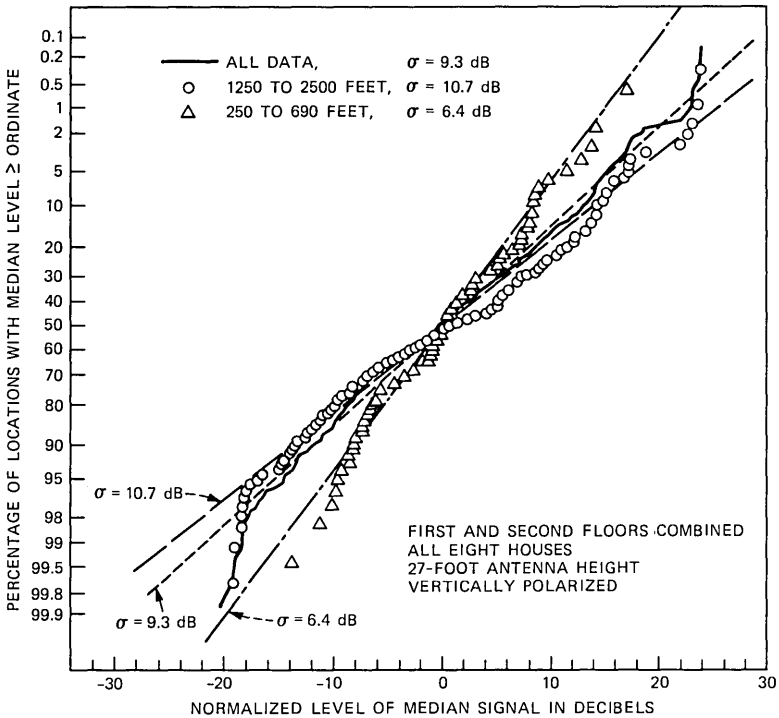

Fig. 28—Cumulative distributions for first- and second-floor locations combined similar to those in Fig. 27. The regression trend removed was the dashed and dotted line in Figs. 23 and 24.

expected to be worse, because of the small number of samples. Thus, log-normal distributions are good descriptions for the various groupings of the data.

For the different distance groupings in Table V, the standard deviations for all the groupings by floors increase with increasing distance. The increase is small but is very consistent across all the different groupings. Therefore, increase in standard deviation with distance probably represents an actual characteristic of the propagation environment.

IV. SUMMARY

Signal levels were measured within and around eight suburban houses from various locations of an instrumentation van. The van locations ranged from 250 to 2500 feet from the houses. Median signal levels were determined for the small-scale signal variations in 4-foot-square areas. Parameters describing the variation of these small-scale medians over large-scale changes for the eight individual houses are summarized in Table II. Parameters describing large-scale changes for

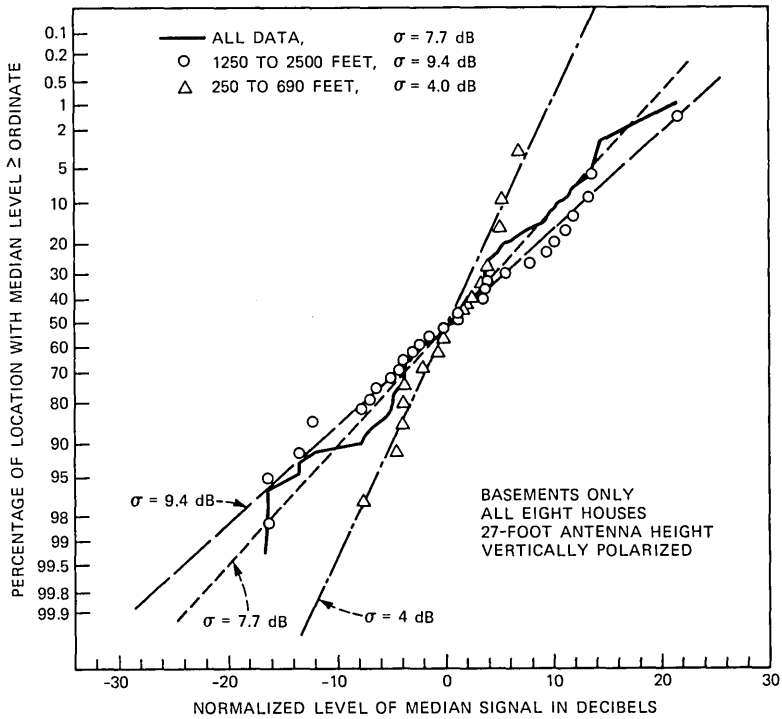

Fig. 29—Cumulative distributions for basement locations similar to those in Fig. 27. The regression trend removed was the solid line in Fig. 25.

Table V—Parameters for all eight houses (vertically polarized, 27-foot antenna height)

Floor	σ Trend Removed (dB)	Mean Trend Removed (dB)	No. of Points
250 to 690 ft			
OS	7.8	0.4	67
1	6.1	0.6	61
2	7.2	−0.7	31
B	3.9	0.2	16
1 and 2	6.4	0.4	92
OS, 1, 2, B	8.0	0.3	175
690 to 1250 ft			
OS	9.0	−1.5	91
1	8.5	−1.5	92
2	8.0	−0.2	35
B	7.4	−0.5	17
1 and 2	8.8	−1.5	127
OS, 1, 2, B	9.5	−1.3	235
1250 to 2300 ft			
OS	10.3	0.9	124
1	9.8	0.9	107
2	10.3	0.4	66
B	9.0	0.2	29
1 and 2	10.7	0.9	173
OS, 1, 2, B	11.2	0.8	326

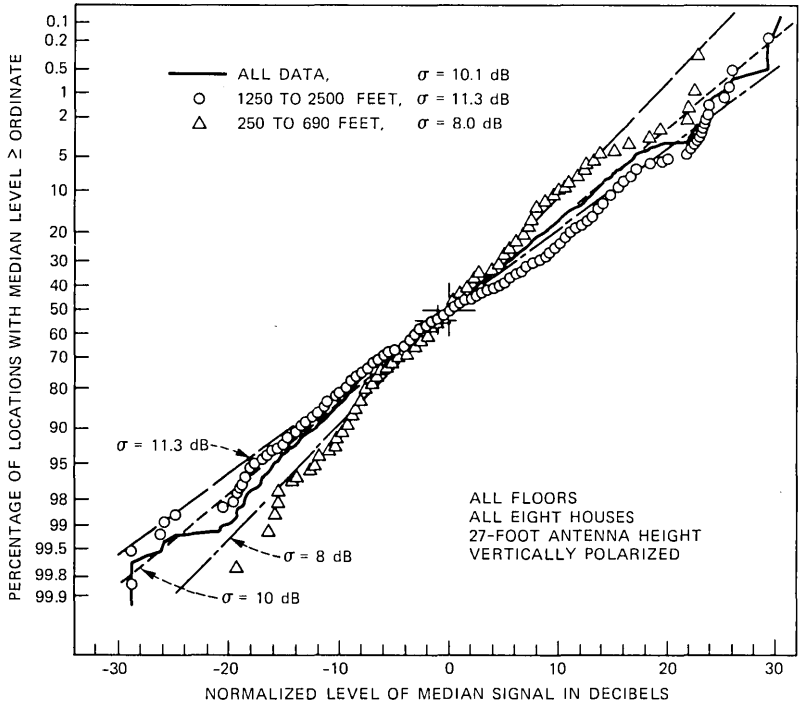

Fig. 30—Cumulative distributions for all floors and outside combined similar to those in Fig. 27. The regression trend removed was the solid line in Fig. 26.

different groupings of the data from all eight houses are summarized in Tables IV and V. Effects of house construction and the environment are discussed in Section 3.2.2.

V. ACKNOWLEDGMENTS

We wish to thank those people who allowed us to make the measurements in their houses that are reported in this paper; without their patience and tolerance this needed set of data could not have been obtained. The continued support of L. J. Greenstein and D. O. Reudink is also greatly appreciated.

REFERENCES

1. D. C. Cox, R. R. Murray, and A. W. Norris, "Measurements of 800-MHz Radio Transmission Into Buildings with Metallic Walls," B.S.T.J., *62*, No. 9, Part 1 (November 1983), pp. 2695–717.
2. H. H. Hoffman and D. C. Cox, "Attenuation of 900-MHz Radio Waves Propagating into a Metal Building," IEEE Trans. Ant. Propag., *AP-30* (July 1982), pp. 808–11.
3. W. C. Jakes, *Microwave Mobile Communications*, New York: Wiley, 1974.
4. S. E. Alexander, "Radio Propagation Within Buildings at 900 MHz," Electron. Lett., *18* (October 14, 1982), pp. 913-4.

5. S. E. Alexander and G. Pugliese, "Cordless Communication Within Buildings: Results of Measurements at 900 MHz and 60 GHz," British Telecom Technology, *1* (July 1983), pp. 99–105.
6. D. C. Cox, "Multipath Delay Spread and Path Loss Correlation for 910 MHZ Urban Mobile Radio Propagation," IEEE Trans. Veh. Technol., *VT-26* (November 1977), pp. 340–4.
7. P. A. Matthews, *Radio Wave Propagation, VHF and Above,*" London: Chapman and Hall, Ltd., 1965, Chapter 2.
8. M. Abramowitz and I. A. Stegun, *Handbook of Mathematical Functions*, National Bureau of Standards Applied Mathematics, Series 55, U.S. Government Printing Office, Washington, Third Printing, March 1965.

AUTHORS

Donald C. Cox, B. S., M. S., University of Nebraska, Lincoln, 1959 and 1960, respectively, both in Electrical Engineering; Ph.D. (Electrical Engineering), Stanford University, 1968; Honorary Dr. of Science, University of Nebraska, Lincoln, 1983; U.S. Air Force Officer, 1960–1963; Stanford University, 1963–1968; AT&T Bell Laboratories, 1968–1984; Bell Communications Research Inc., 1984—. Mr. Cox worked on microwave communications system design at Wright-Patterson AFB, Ohio. From 1963 to 1968 he was at Stanford University doing tunnel diode amplifier design and research on microwave propagation in the troposphere. From 1968 to 1973 he was a Member of Technical Staff at Bell Laboratories, doing research in mobile-radio propagation and on high-capacity mobile-radio systems. From 1973 to 1983 Mr. Cox was Supervisor of a group that did propagation and systems research for portable-radio telephony and for millimeter-wave satellite communications. In 1983 he became Head of the Radio and Satellite Systems Research Department, which became a division in Bell Communications Research on January 1, 1984. He is now Division Manager of that Research Division. Fellow, IEEE; Recipient of International Marconi Prize in Electromagnetic Wave Propagation (Italy), 1983. Member, AAAS; URSI Interunion Group on Time Domain Measurements; Commissions B, C, and F of USNC/URSI; Sigma Xi; Sigma Tau; Eta Kappa Nu; and Pi Mu Epsilon; Associate Editor, IEEE Transactions on Antennas and Propagation; Registered Professional Engineer, Ohio and Nebraska.

Roy R. Murray, B.S. (Electronic Engineering), 1975, Monmouth College; AT&T Bell Laboratories, 1965–1983; Bell Communications Research Inc., 1984—. Mr. Murray has worked on research techniques for improving mobile-radio-systems operation, co-phasing techniques for satellite TDMA-phased array antennas, and high-speed multilevel digital modulators. More recently, he has worked on UHF radio propagation into buildings. Currently, he is a member of the Radio and Satellite Systems Research Division. Member, Eta Kappa Nu.

AT&T Bell Laboratories Technical Journal
Vol. 63, No. 6, July–August 1984
Printed in U.S.A.

Transmission Errors in Companded PCM Over Gaussian and Rayleigh Fading Channels

By R. STEELE,* C.-E. SUNDBERG,† and W. C. WONG‡

(Manuscript received January 9, 1984)

Transmission errors in μ-law pulse-code-modulated systems are capable of inflicting considerable distortion in the recovered analog signals. We analyze this distortion when the transmission is over radio channels, and when either noncoherent frequency shift keying or coherent phase shift keying (CPSK) modulation is employed. We consider both Gaussian and Rayleigh fading channels, and for the latter we investigate the effect of bit scrambling prior to transmission and two types of diversity. We determined the gain in overall signal-to-noise ratio due to using the minimum distance code compared to the conventional folded binary code for low values of input signal power. In addition to the theoretical results, we present computer simulations of μ-law pulse-code-modulated encoded speech transmitted over the same channels, using CPSK modulation, bit scrambling, and diversity where appropriate, i.e., for the same conditions as employed in the derivation of our theory.

I. INTRODUCTION

Pulse Code Modulation (PCM) is well entrenched in the telephone networks as a means of conveying speech in a digital format,[1] and its impairments are therefore worthy of serious investigation. The distortion in the recovered speech signal arises from noise in the encoding process, and the presence of digital transmission errors. By employing logarithmic companded PCM at bit rates of 56 kb/s or 64 kb/s, and

* University of Southampton, England. † University of Lund, Sweden. ‡ AT&T Bell Laboratories.

Copyright © 1984 AT&T. Photo reproduction for noncommercial use is permitted without payment of royalty provided that each reproduction is done without alteration and that the Journal reference and copyright notice are included on the first page. The title and abstract, but no other portions, of this paper may be copied or distributed royalty free by computer-based and other information-service systems without further permission. Permission to reproduce or republish any other portion of this paper must be obtained from the Editor.

by operating at a Bit Error Rate (BER) less than 10^{-5}, we obtain so-called toll-quality speech.[2] For channels where the BER significantly exceeds 10^{-5}, for example, radio channels, the distortion in the recovered speech due to transmission errors becomes significant, dominating the encoder noise. The distortion due to transmission errors is known as digital noise,[3,4] and can be combatted by means of channel coding,[5,6] weighting the amplitude of the binary bits prior to transmission,[7–9] or by post-enhancement procedures.[10–12]

In this study we are concerned with determining the digital noise power in μ-law PCM radio transmission systems. We examine this power for different radio channels, methods of Radio Frequency (RF) modulation, types of binary encoding, bit scrambling, and the application of diversity. In Section II we quantify digital noise power, while in Section III we state our objective performance criterion. We examine two types of channels, the Gaussian in Section IV, and the Rayleigh fading channel in Section V. In the latter case we investigate the effect of scrambling the μ-law PCM bit stream prior to transmission, and the advantages of diversity. The modulation methods considered are Noncoherent Frequency Shift Keying (NCFSK) and Coherent Phase Shift Keying (CFSK). The minimum distance code designed for low-level speech is described in Section VI. In Section VII we discuss the performance of the various μ-law PCM radio systems, where our theoretical formulae are presented in graphical formats, along with simulation results for speech signals, and show the experimental results for μ-law PCM speech transmitted over a mobile radio channel. In the last section we summarize our discourse and draw conclusions.

II. DIGITAL ERRORS IN PCM SYSTEMS

Figure 1 shows a schematic form of the basic companded PCM system. The input sequence $\{x\}$, having a Probability Density Function (PDF) $p_X(x)$, has its amplitude compressed according to the function $f(x)$, and is then uniformly quantized. The combination of the function $f(x)$ and the uniform quantizer produces an effective nonlinear quantizer, as shown in Fig. 2, where $f(x)$ and the number of quantization levels have been selected arbitrarily for the purpose of illustration. The voltage ranges of the input and quantized signals are normalized for convenience to $[-1, 1]$, and the quantized levels are uniformly spaced apart as a result of the uniform quantizer. However, the range of input amplitudes that are quantized to a particular value increases with the magnitude of the input levels. Thus all input amplitudes approximately in the ranges $x_i \pm (\delta_i/2)$ and $x_{i+1} \pm (\delta_{i+1}/2)$ are quantized to y_i and y_{i+1}, respectively, where $\delta_{i+1} > \delta_i$.

Suppose the input signal is sampled at a rate in excess of the

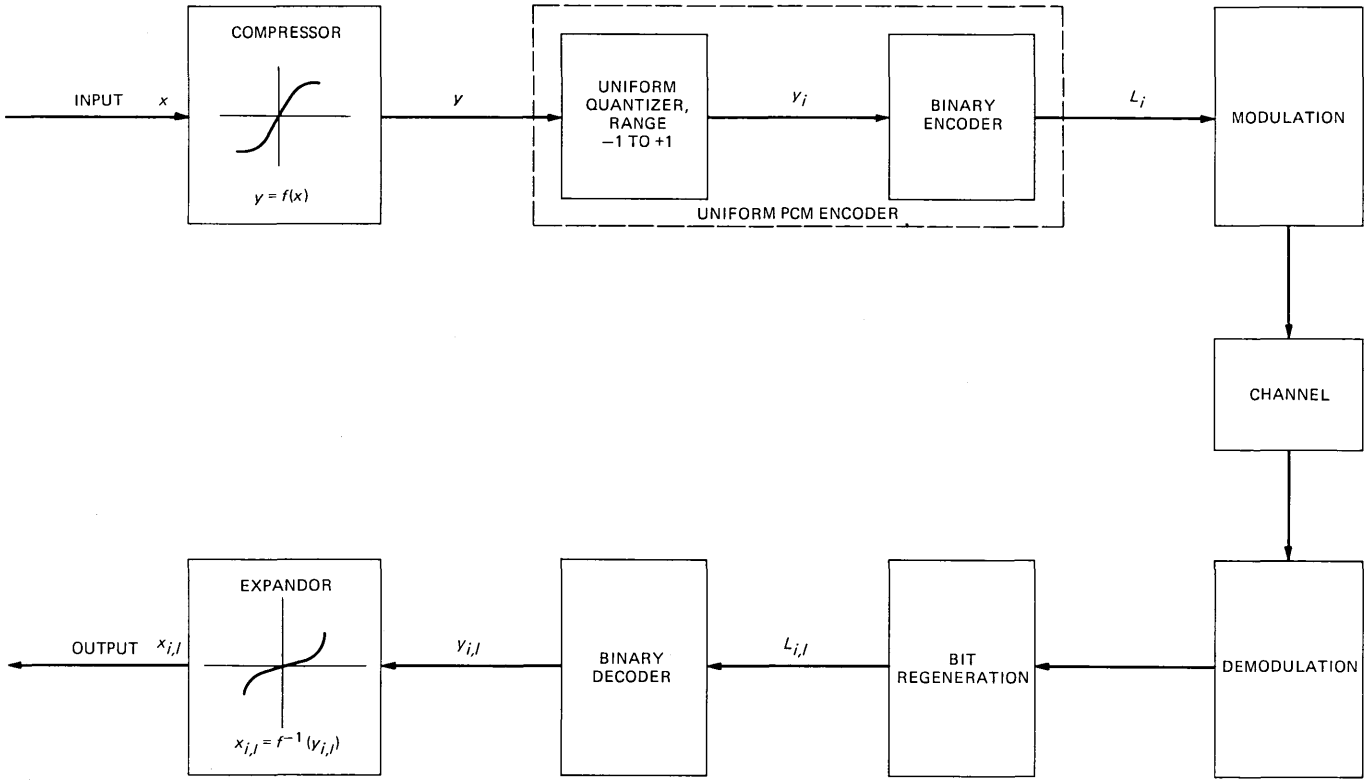

Fig. 1—The basic companded PCM system.

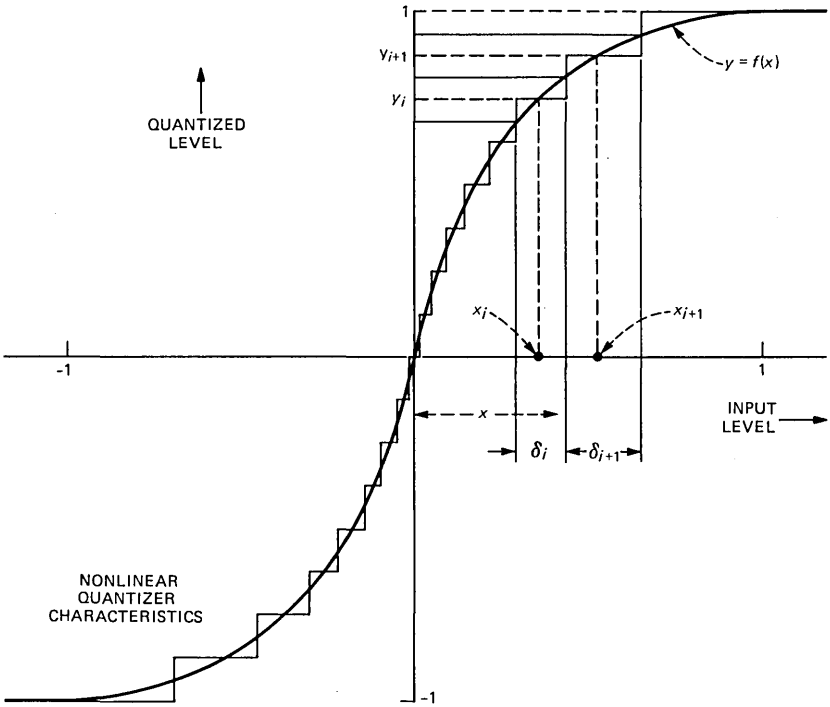

Fig. 2—Exemplary nonlinear quantizer; arbitrary $f(x)$ and number of quantization levels.

Nyquist rate, and the resulting sequence $\{x\}$ is quantized to $\{y\}$. Binary encoding of the quantized sequence ensues to yield $\{L\}$, where each component is an N-bit word. The $\{L\}$ sequence is filtered, modulates a carrier (e.g., using NCFSK), and is transmitted. At the receiver demodulation is performed, and the bits are regenerated. In Fig. 1 we show a particular word L_i at the transmitter, and its regeneration at the receiver as $L_{i,l}$. The word $L_{i,l}$ may be represented by the exclusive-OR ($\oplus$) operation of the binary vectors L_i and e_l,

$$L_{i,l} = L_i \oplus e_l, \tag{1}$$

where $L_{i,l} = L_i$ if no transmission errors occur, and e_l is the lth digital error sequence of length N bits. Whenever the error sequence contains a logical 1 representing the presence of a bit error, the true bit in L_i is inverted, and the error appears in $L_{i,l}$. The N-bit word $L_{i,l}$ is binary decoded to $y_{i,l}$, and the inverse operation of $f(x)$ (i.e., an expansion) is performed to yield the recovered sample,

$$x_{i,l} = f^{-1}(y_{i,l}). \tag{2}$$

The recovered sample $x_{i,l}$ differs from the input sample x, and this

difference is the overall system noise sample. The average noise power in a PCM system is, therefore,

$$\epsilon^2 \triangleq E\{(x - x_{i,l})^2\}, \tag{3}$$

where $E\{(\cdot)\}$ denotes expected value of $(\cdot)$ and is formulated over both source and channel statistics. For the large number of quantization levels considered here, typically 256, the average noise power may be separated into three components, viz:

$$\epsilon^2 = \epsilon_q^2 + \epsilon_c^2 + \epsilon_a^2, \tag{4}$$

where ϵ_q^2, ϵ_c^2, and ϵ_a^2 are the quantization, clipping, and transmission error noise power components, respectively. The noise power generated in the encoder due to the amplitude and time quantization is

$$\epsilon_q^2 + \epsilon_c^2 = E\{(x - x_i)^2\}, \tag{5}$$

where x_i is the recovered sample associated with the quantized sample y_i in the absence of transmission errors, and the expected value is formed over the source statistics. We are more concerned here with the digital noise power, i.e., the noise in the recovered samples due to the presence of digital errors, and we express this power as

$$\epsilon_a^2 = E_{i,l}\{(x_i - x_{i,l})^2\}, \tag{6}$$

where $E_{i,l}(\cdot)$ signifies that the average of $(\cdot)$ is performed over all levels of y_i and all possible error sequences e_l. By observing that the source, e.g., a speech signal and PCM encoder, is independent of the imperfections in the channel, we may express ϵ_a^2 as

$$\epsilon_a^2 = \sum_{l=1}^{2^N-1} \rho_l E_i\{(x_i - x_{i,l})^2\}. \tag{7}$$

The average E_i is formed over all the possible 2^N quantization levels, and ρ_l is the probability of occurrence of the specific error sequence e_l.

At this juncture we introduce the A-factor,[3,4] defined as

$$A_l \triangleq E_i\{(x_i - x_{i,l})^2\}, \tag{8}$$

enabling us to write eq. (7) as

$$\epsilon_a^2 = \sum_{l=1}^{2^N-1} \rho_l A_l. \tag{9}$$

The A-factor A_l is the average noise power at the output of the PCM decoder due to the presence of an error sequence e_l. We have used the notation $e_1, e_2, \cdots, e_N$ to represent the single error bit patterns in the most significant bit (msb), next msb, $\cdots$, least significant bit (lsb), respectively. For example, e_3 is the binary sequence 00100000, implying

the error occurred in the third bit. However, we may have multiple bit errors, and l has integer values that extend to $2^N - 1$, since e_l must contain at least one component that is a logical 1. The number of possible error patterns for w bit errors in an N-bit word is

$$\Omega_w = \binom{N}{w} = \frac{N(N-1)(N-2)\cdots(N-w+1)}{w!}, \tag{10}$$

where the index w is the Hamming weight. When $w = 1$ the N single error bit patterns occur, $w = N$ yields the pattern where every bit in the word is regenerated erroneously, while $\Omega_{N/2}$ is the largest set of error bit patterns. For each error bit pattern there is a unique A-factor, giving $2^N - 1$ different A-factors. For example, the A-factor A_1 applies to a PCM word whose msb bit is erroneously regenerated, and is computed by determining the mean square value of the error $(x_i - x_{i,1})$ over all quantized levels when this particular bit error sequence error is present. The A-factors have a number of attractive properties. They depend only on the source conditions, and not on the channel. Specifically, for the particular number of bits regenerated erroneously in the recovered words and their position in these words, the A-factors depend only on the type of bit allocation, the companding law, and the PDF of x. The A-factors are unaffected by how the bit errors originated. Thus, once we have computed the A-factors for a given source, i.e., input signal and PCM encoder, we can use these factors to calculate the noise due to transmission errors for random channels, fading channels, different modulation schemes, various channel-coding strategies, and so on. Armed with the A-factors we can determine the transmission error power, ϵ_a^2, for any channel that can be characterized by the error sequence probabilities ρ_l, $l = 1$ to $2^N - 1$.

III. PERFORMANCE CRITERION

The objective performance criterion to be used here is the overall signal-to-noise ratio (s/n),

$$\hat{s/n} = \frac{E\{x^2\}}{\epsilon_q^2 + \epsilon_c^2 + \epsilon_a^2} = \frac{\sigma_x^2}{\epsilon^2} \tag{11}$$

where ϵ^2 is the average noise power [see eq. (4)] and $E\{x^2\}$ or σ_x^2 is the average power of the input sequence. We usually express σ_x^2 in decibels relative to the input level at the start of clipping, i.e., relative to a level magnitude of unity.

IV. THE GAUSSIAN CHANNEL

Consider the situation where the channel errors are independent such that any bit may be in error with probability P. The digital noise

power is given by eq. (9) and can be partitioned into noise power components,

$$\epsilon_a^2 = \epsilon_1^2 + \epsilon_2^2 + \cdots + \epsilon_N^2, \tag{12}$$

where $\epsilon_1^2, \epsilon_2^2, \cdots, \epsilon_N^2$ are the noise powers due to 1-, 2-, $\cdots$, N-bit errors per word, respectively. The first component is

$$\epsilon_1^2 = P_1 \sum_{l=1}^{N} A_l, \tag{13}$$

where P_1 is the probability of a word having a single bit error, namely

$$P_1 = P(1 - P)^{N-1}. \tag{14}$$

The number of A-factors associated with a particular number of bit errors per word depends on N. For example, when $N = 8$, there are 8, 28, 56, 70, 56, 28, 8, and 1 A-factors required in the computation of ϵ_1^2, ϵ_2^2, ϵ_3^2, ϵ_4^2, ϵ_5^2, ϵ_6^2, ϵ_7^2, and ϵ_8^2, respectively. Thus the noise power components of ϵ_a^2 are

$$\epsilon_a^2 = P_1 \sum_{l=1}^{N} A_l + P_2 \sum_{l=N+1}^{N+\binom{N}{2}} A_l + \cdots + P_N A_{2^N-1}, \tag{15}$$

and $P_{(\cdot)}$ is the probability that $(\cdot)$ bits in the N-bit word are regenerated erroneously. Rearranging eq. (15) as

$$\epsilon_a^2 = P_w \sum_{l=l_a+1}^{l_b} A_l;\ w = 1, 2, \cdots, N \tag{16}$$

$$= P_w S_w, \tag{17}$$

where

$$l_a = \sum_{k=0}^{w-1} \binom{N}{k} \tag{18}$$

and

$$l_b = \sum_{k=1}^{w} \binom{N}{k}, \tag{19}$$

and expressing P_w in terms of the average bit error probability P, we have

$$\begin{aligned} \epsilon_a^2 &= P(1 - P)^{N-1} S_1 + P^2(1 - P)^{N-2} S_2 + \cdots + P^N S_N \\ &= \sum_{w=1}^{N} P^w (1 - P)^{N-w} S_w. \end{aligned} \tag{20}$$

From eqs. (16) to (19) we observe that S_w is the sum of the A-factors associated with the Ω_w error sequencies $\{e_l\}$ containing w ones.

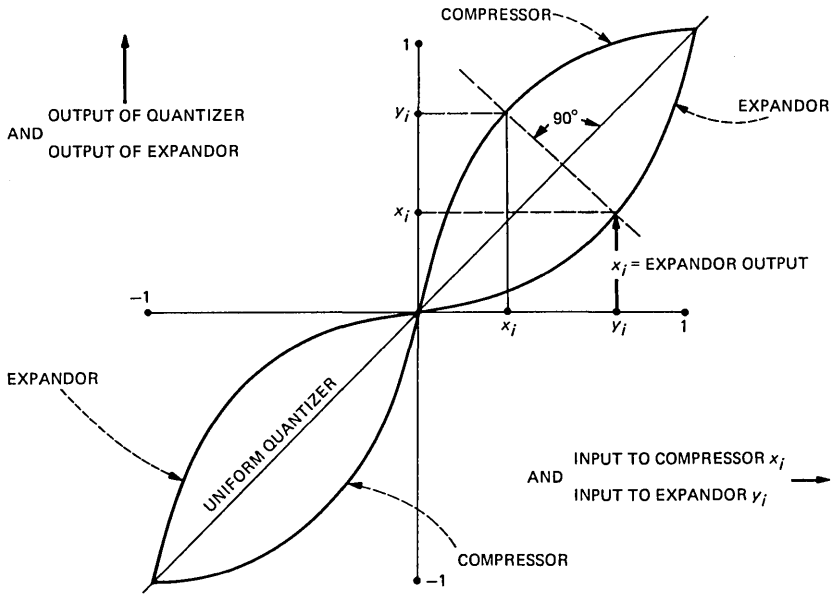

Fig. 3—Compressor and expandor characteristics.

4.1 Determination of the A-factors

Equation (9) shows that the noise power due to transmission errors can be calculated with the aid of a set of A-factors. For the input sequence $\{x\}$ with its PDF $p_X(x)$, the A-factors can be determined using eq. (8), viz:

$$A_l = \sum_{i=0}^{2^N-1} p_X(x_i)\delta_i(x_i - x_{i,l})^2, \tag{21}$$

and the sample x is quantized to y_i if it approximately resides in the range from $x_i - (\delta_i/2)$ to $x_i + (\delta_i/2)$. Figure 3 displays both compressor and expandor characteristics, and we observe that when the quantized level y_i is expanded, the level x_i is recovered. Thus if x falls within δ_i, it is recovered at the receiver as $x_{i,l} = x_i$, assuming no transmission errors occur. If transmission errors are present, the expanded sample at the receiver is $x_{i,l}$. If we assume a large number of quantization levels, the probability density function $p_X(x)$ has an approximately constant value of $p_X(x_i)$ over the interval δ_i. Now the range of the compressor function $f(x)$ is 2, and therefore the N quantized levels are spaced apart by $2/2^N$. Consequently, the slope $f'(x)$ of the compression curve $f(x)$ for an input amplitude x_i is

$$f'(x) = \frac{2^{1-N}}{\delta_i}, \tag{22}$$

and we write eq. (21) as

$$A_l = \sum_{i=0}^{2^N-1} \frac{p_X[f^{-1}(y_i)]2^{1-N}}{f'(f^{-1}(y_i))} [f^{-1}(y_i) - f^{-1}(y_{i,l})]^2 \tag{23}$$

to ease the computation of the A-factors. The values of A_l depend on the PDF of x, the compression characteristic, the bit assignment, and the number and location of the erroneous bits in the PCM word. Thus, we need to determine the A-factors for each PCM system at different input levels.

In this discourse we will perform numerical calculations for the input signal having an exponential PDF,

$$p_X(x) = \frac{1}{\sigma_x \sqrt{2}} \exp\left(-\frac{\sqrt{2}x}{\sigma_x}\right), \tag{24}$$

although our results can be generalized for other PDFs. Unless it is explicitly stated we will assume binary folded PCM is employed, where the msb is the polarity of the quantized sample and the remaining bits represent its magnitude. The PDF $p_X(x)$ of eq. (24) is assumed to be symmetrical about the zero voltage level, and the compandor is an odd function spanning the range from -1 to $+1$.

4.2 Special case of single error A-factors and μ-law companding

To calculate the A-factors for a single bit error in any of the N-bit positions of a PCM word, we express eq. (21) as[6]

$$A_l = \sum_{i=0}^{2^N-1} p_X(x_i)\delta_i a_l(x_i), \tag{25}$$

where

$$a_l(x_i) = (x_i - x_{i,l})^2; \qquad l = 1, 2, \cdots, N, \tag{26}$$

and $l = 1, 2, \cdots, N$ corresponds to a single error in the msb, the next msb, $\cdots$, lsb, respectively. Thus, the $a_l(x_i)$ terms are related to a specific single bit error in the lth bit position, and a specific input signal amplitude x_i. Observe that $a_l(x_i)$ is independent of $p_X(x_i)$, and is a function of the PCM bit code and the compandor rule. By performing the summations in eq. (25) we obtain expressions for the single-error A-factors for a particular PDF $p_X(x_i)$. However, we are concerned here in how the effect of a particular single error varies with x_i, and this we can determine with the aid of the $a_l(x_i)$ functions. Of course, functions of the type of $a_l(x_i)$ can also be derived for any particular multiple-error pattern e_l. The analysis, however, gets increasingly complex.

Before providing a general formula for $a_l(x_i)$, we will consider for

exemplary purposes the case of an error occurring in the second bit position, i.e., $l = 2$. Consider the input sample to have a value x_1, which is compressed to $y_1 = f(x_1)$. Because we are discussing the most significant magnitude bit, an error in this bit will either result in y_1 increasing by 1/2 when a logical 0 is regenerated as a logical 1, or decreasing by a 1/2 when a logical 1 is regenerated as a logical 0. The erroneous decoded y_1 is $f^{-1}[f(x_1) + (1/2)]$ or $f^{-1}[f(x_1) - (1/2)]$, depending on whether the original bit was a logical 0 or 1, respectively. Thus for any x_i we may express $a_2(x_i)$ from eq. (26) as

$$a_2(x_i) = \left[f^{-1}\left[f(x_i) \pm \frac{1}{2}\right] - x_i\right]^2.$$

This method of reasoning enables us to obtain $a_l(x_i)$ for every value of l. For $a_1(x_i)$ we have

$$a_1(x_i) = (2x_i)^2, \qquad 0 \leqslant x_i \leqslant 1, \tag{27}$$

and the general formula for $a_l(x_i)$, $l \geqslant 2$ is

$$a_l(x_i) = \begin{cases} \left\{f^{-1}\left[f(x_i) + \dfrac{1}{2^{(l-1)}}\right] - x_i\right\}^2 & \text{for } f^{-1}\left\{\dfrac{\nu - 1}{2^{(l-1)}}\right\} \\ \qquad \leqslant x_i < f^{-1}\left\{\dfrac{\nu}{2^{(l-1)}}\right\}; & \nu \text{ odd} \\ & \nu = 1, 3, \cdots, 2^{(l-1)} - 1 \\ \left\{f^{-1}\left[f(x_i) - \dfrac{1}{2^{(l-1)}}\right] - x_i\right\}^2 & \text{for } f^{-1}\left\{\dfrac{\nu - 1}{2^{(l-1)}}\right\} \\ \qquad \leqslant x_i < f^{-1}\left\{\dfrac{\nu}{2^{(l-1)}}\right\}; & \nu \text{ even} \\ & \nu = 2, 4, \cdots, 2^{(l-1)}. \end{cases} \tag{28}$$

So far we have not specified the compression function $f(x_i)$, but as it is our intention to subsequently place considerable emphasis on μ-law PCM we provide now the $a_l(x_i)$ terms for this type of compression. The μ-law compression function is specified by[1]

$$f(x_i) = \frac{\log(1 + \mu x_i)}{\log(1 + \mu)}, \qquad 0 \leqslant x_i \leqslant 1, \tag{29}$$

and the corresponding expansion to recover x_i is

$$x_i = f^{-1}(y_i) = \frac{1}{\mu}\{\exp[y_i \log(1 + \mu)] - 1\}, \qquad 0 \leqslant y_i \leqslant 1. \tag{30}$$

Equation (27) is applicable for μ-law PCM, and the general formula

for $l \geqslant 2$ is

$$a_l(x_i) = \begin{cases} f^{-1}\left[\dfrac{1}{2^{(l-1)}}\right]^2 (1 + \mu x_i)^2 & \text{for } f^{-1}\left\{\dfrac{\nu - 1}{2^{(l-1)}}\right\} \\ \quad \leqslant x_i < f^{-1}\left\{\dfrac{\nu}{2^{(l-1)}}\right\}; & \nu \text{ odd} \\ & \nu = 1, 3, \cdots, 2^{(l-1)} - 1 \\ (1 + \mu)^{-\frac{1}{2^{(l-2)}}} \cdot f^{-1}\left[\dfrac{1}{2^{(l-1)}}\right]^2 (1 + \mu x_i)^2 & \text{for } f^{-1}\left\{\dfrac{\nu - 1}{2^{(l-1)}}\right\} \\ \quad \leqslant x_i < f^{-1}\left\{\dfrac{\nu}{2^{(l-1)}}\right\}; & \nu \text{ even} \\ & \nu = 2, 4, \cdots, 2^{(l-1)}. \end{cases} \tag{31}$$

Inserting $a_l(x_i)$ and $p_X(x_i)$ from eqs. (27), (31), and (24), respectively, into eq. (25) enables us to compute the single bit error A-factors for μ-law PCM.

The variation of the $a_l(x_i)$ factors as a function of quantized level x_i, $l = 1, 2, \cdots, 8$, is displayed in Fig. 4 for 8-bit μ-law PCM, $\mu = 255$. As we expected from eq. (27), where $l = 1$, $a_1(x_i)$ is a monotonic function as shown in Fig. 4a. Let us consider the case of $l = 2$ when the single error occurs in the magnitude bit. To provide some insight into $a_2(x_i)$, we note that its value in eq. (28) is

$$a_2(x_i) = \begin{cases} f^{-1}\left[f(x_i) + \dfrac{1}{2}\right] - x_i\Big\}^2; & 0 \leqslant x_i < f^{-1}\left(\dfrac{1}{2}\right) \\ f^{-1}\left[f(x_i) - \dfrac{1}{2}\right] - x_i\Big\}^2; & f^{-1}\left(\dfrac{1}{2}\right) \leqslant x_i \leqslant 1. \end{cases} \tag{32}$$

If we substitute $f(x_i)$ into $a_2(x_i)$, and for the moment confine ourselves to $0 \leqslant x_i < f^{-1}(1/2)$, we have

$$a_2(x_i) = \left\{f^{-1}\left[\frac{\log(1 + \mu x_i)}{\log(1 + \mu)} + \frac{1}{2}\right] - x_i\right\}^2, \tag{33}$$

and on applying eq. (30)

$$\begin{aligned} a_2(x_i) &= \left(\frac{1}{\mu}\left\{\exp[\log(1 + \mu x_i) + \frac{1}{2}\log(1 + \mu)] - 1\right\} - x_i\right)^2 \\ &= \left[\frac{1}{\mu}\left(\sqrt{1 + \mu} - 1\right)\right]^2 (1 + \mu x_i)^2. \end{aligned} \tag{34}$$

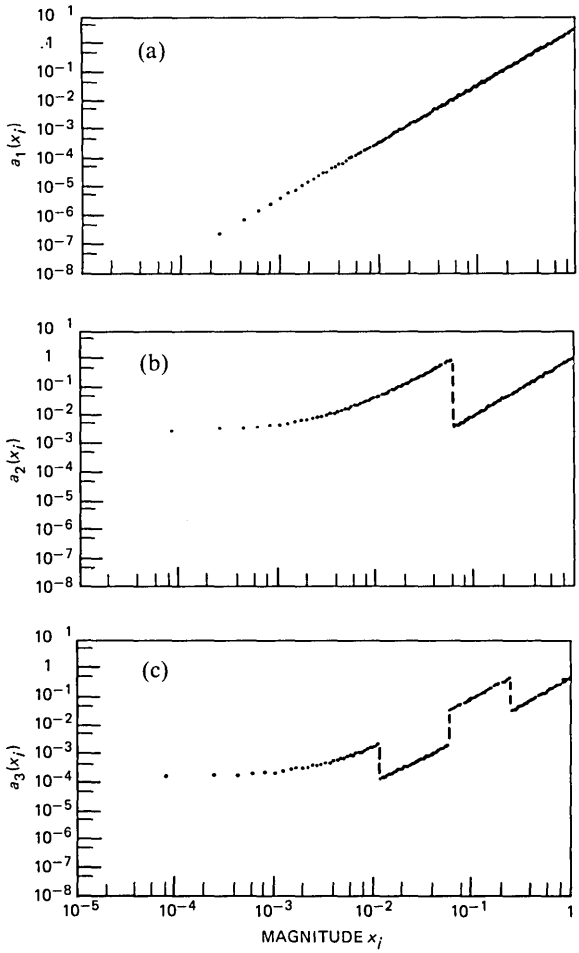

Fig. 4—Variation of $a_l(x_i)$ as a function of x_i for 8-bit μ-law PCM, $\mu = 255$. The subfigures a through h apply for a single bit error in the msb ($l = 1$), the next msb ($l = 2$), $\cdots$, lsb ($l = 8$), respectively.

From eq. (30) the value of x_i when $y_i = 1/2$ is

$$f^{-1}\left(\frac{1}{2}\right) = \frac{1}{\mu}\left[e^{[1/2]\log(1+\mu)} - 1\right]$$

$$= \frac{1}{\mu}\left(\sqrt{1+\mu} - 1\right), \tag{35}$$

and hence we obtain

$$a_2(x_i) = \left[f^{-1}\left(\frac{1}{2}\right)\right]^2 (1 + \mu x_i)^2; \qquad 0 \leq x_i < f^{-1}\left(\frac{1}{2}\right), \tag{36}$$

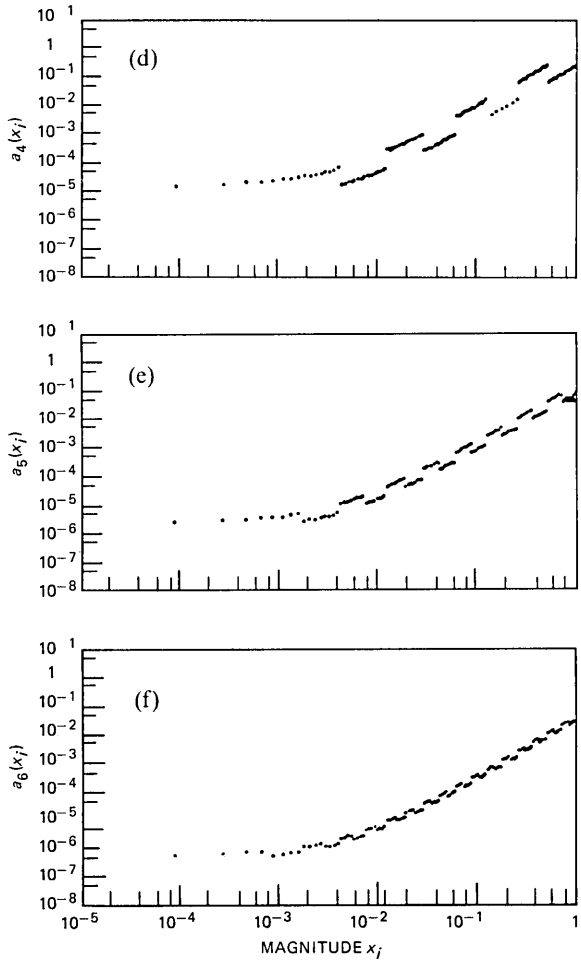

Fig. 4—Continued.

the value given by eq. (31). Observe that $y_i = 1/2$ marks the boundary between the most significant magnitude bit being 0 ($y_i < 1/2$), and being a logical 1 ($y_i \geqslant 1/2$). Consequently, an error in the most significant magnitude bit changes the magnitude of the quantized signal by a 1/2. However, the change in $x_{i,l}$ is not a 1/2, being dependent on the μ-law. Figure 5 illustrates that if the input sample has a small amplitude, x_1 say, and is compressed to y_1, then the effect of an error in the most significant magnitude bit is to cause y_1 to increase by half the range to $y_{1,l}$. The corresponding decoded signal is $x_{1,l}$, having an error E_1 of $\sqrt{a_2(x_1)}$. If the input sample amplitude is larger, say x_2, and the same bit is inverted, $x_{2,l}$ is recovered having an error E_2 of

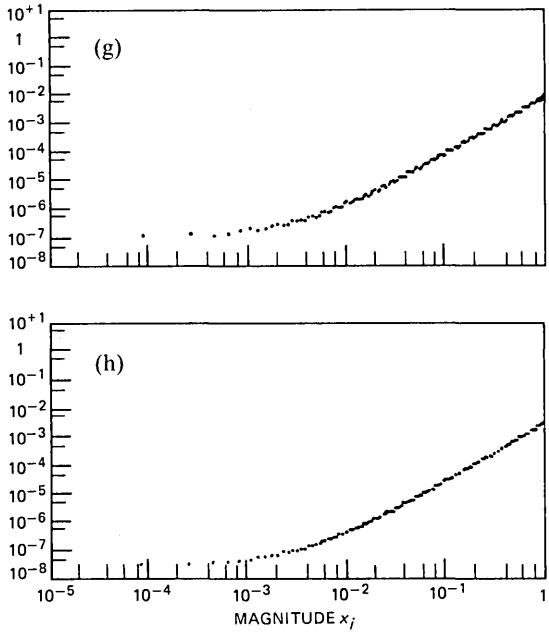

Fig. 4—Continued.

$\sqrt{a_2(x_2)}$ that is significantly larger than E_1. Thus the errors become significantly larger as y_i moves closer to 1/2. The variation of $a_2(x_i)$ over the range of x from zero to f^{-1} (1/2) is shown in Fig. 4b. As we expected from eq. (36), when x_i is very small, $a_2(x_i)$ is a constant equal to $[f^{-1}(1/2)]^2$. As x_i approaches $f^{-1}(1/2)$,

$$a_2(x_i) \simeq [f^{-1}(1/2)]^2 \mu^2 x_i^2 \tag{37}$$

and the variation appears as a straight line in the figure.

Consider the situation when x_i exceeds $f^{-1}(1/2)$. An input x_3 (see Fig. 5), encoded to y_3 and then subjected to an error in the second bit position, is reduced to $x_{3,l}$, and the resulting error E_3 of $\sqrt{a_2(x_3)}$ is less than E_2 and of opposite polarity. We therefore observe in Fig. 4b a discontinuity in $a_2(x_i)$ as x_i just exceeds $f^{-1}(1/2)$, causing it to plummment. By applying similar arguments to those employed in establishing eq. (36), we obtain the result given in eq. (31), namely,

$$a_2(x_i) = \frac{\left[f^{-1}\left(\frac{1}{2}\right)\right]^2}{1+\mu}(1+\mu x_i)^2; \qquad f^{-1}\left(\frac{1}{2}\right) \leqslant x_i \leqslant 1. \tag{38}$$

When $\mu x \gg 1$, $a_2(x_i)$ is proportional to x_i^2, as can be seen in Fig. 4b for $x_i \geqslant f^{-1}$ (1/2).

When errors occur in the third msb, i.e., $l = 3$, we have from eq. (31),

$$a_3(x_i) = \begin{cases} \left[f^{-1}\left(\frac{1}{4}\right)\right]^2 (1 + \mu x_i)^2; & 0 \leqslant x_i < f^{-1}\left(\frac{1}{4}\right) \\ \dfrac{\left[f^{-1}\left(\frac{1}{4}\right)\right]^2}{\sqrt{1+\mu}} (1 + \mu x_i)^2; & f^{-1}\left(\frac{1}{4}\right) \leqslant x_i < f^{-1}\left(\frac{1}{2}\right) \\ \left[f^{-1}\left(\frac{1}{4}\right)\right]^2 (1 + \mu x_i)^2; & f^{-1}\left(\frac{1}{2}\right) \leqslant x_i < f^{-1}\left(\frac{3}{4}\right) \\ \dfrac{\left[f^{-1}\left(\frac{1}{4}\right)\right]^2}{\sqrt{1+\mu}} (1 + \mu x_i)^2; & f^{-1}\left(\frac{3}{4}\right) \leqslant x_i \leqslant f^{-1}(1). \end{cases} \tag{39}$$

From this equation the variation of $a_3(x_i)$ with x_i is evident. The abrupt changes occur at $f^{-1}(1/4)$, $f^{-1}(1/2)$, and $f^{-1}(3/4)$, because the transmission errors cause y_i to change by 1/4. Thus the detailed discussion relating to $a_2(x_i)$ and Fig. 5 are relevant here, but instead of one transition at $f^{-1}(1/2)$ there are three logical transitions for this case of $l = 3$.

For higher values of l there are more transitions in y_i due to transmission errors, and these manifest as more discontinuities in $a_l(x_i)$. For $l = 8$ the logical value of the lsb changes with each succeeding x_i, and as a consequence there are 128 discontinuities in $a_8(x_i)$, although the magnitude of the jumps in $a_8(x_i)$ at the discontinuities are miniscule. The result is that the curve of $a_8(x_i)$, shown in Fig. 4h, appears to be almost smooth.

4.3 Computing the overall s/n

The digital noise power ϵ_a^2 is dependent on the type of digital modulation. For noncoherent frequency shift keying (NCFSK) the bit error probability is[13]

$$P = \frac{1}{2} e^{-\frac{E}{2N_o}}, \tag{40}$$

where E is the bit energy and N_o is the one-sided spectral density function of the white Gaussian noise in the channel. When coherent phase shift keying (CPSK) is employed, the bit error probability is

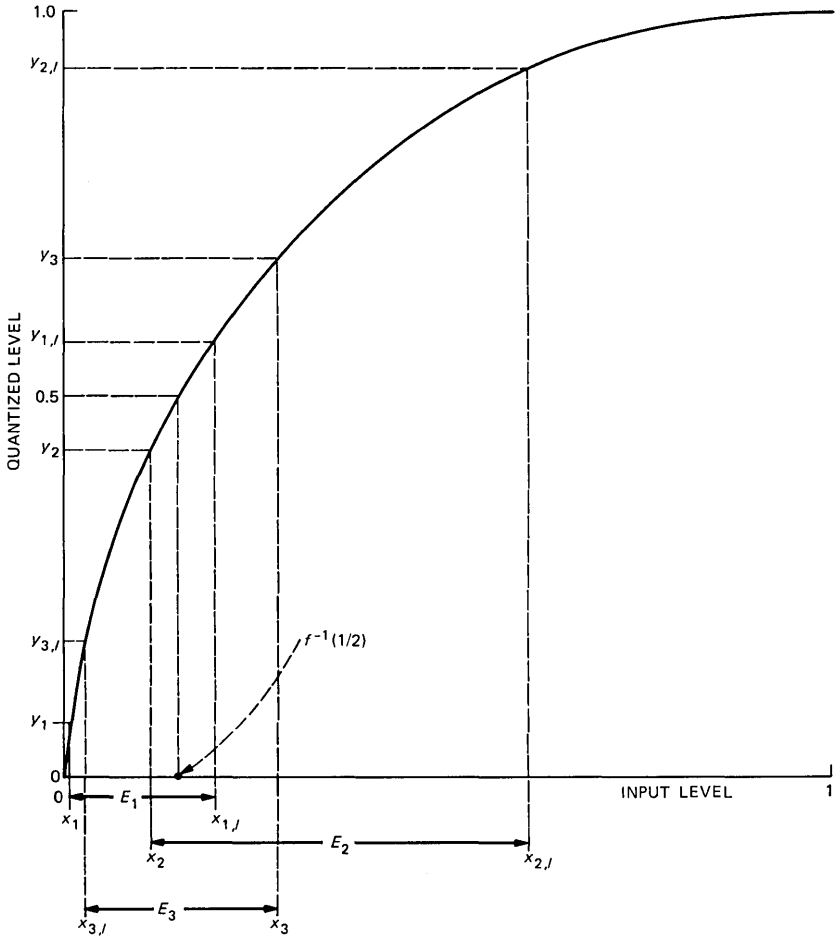

Fig. 5—The nonlinear quantizer characteristic showing how the effect of a transmission error in the second msb ($l = 2$) affects the amplitude of the recovered sample.

given by[13]

$$P = Q\left(\sqrt{\frac{2E}{N_o}}\right). \tag{41}$$

When the values of P given by eq. (40) or eq. (41) are substituted into eq. (20), the digital noise power for NCFSK and CPSK are determined. The knowledge of ϵ_a^2 enables $\hat{s/n}$ to be determined using eq. (11).

V. RAYLEIGH FADING CHANNELS

In Section IV we provide an expression [see eq. (20)] that enables us to calculate the noise power in the recovered signal due to trans-

mission errors in μ-law PCM. The bit errors are considered to be statistically independent. We now turn our attention to transmission channels that contain both additive Gaussian noise and Rayleigh signal fading. Our investigation considers both the effects of scrambling (also called interleaving) and not scrambling the bits prior to transmission, as well as the application of diversity techniques to reduce the digital noise power. We commence by considering the case of NCFSK modulation.

5.1 Digital noise power with NCFSK modulation

5.1.1 Bit scrambling prior to transmission

If the bit stream is scrambled prior to its transmission over a Rayleigh fading channel, and the regenerated bit stream is descrambled at the receiver, then the bit errors will tend to be statistically independent. By the process of scrambling, the burst errors that occur in Rayleigh fading environments are randomized. Because the transmitted signal is subjected to Rayleigh fading, the channel s/n γ is a random variable having a PDF of[13]

$$f(\gamma) = \frac{1}{\Gamma} e^{-\gamma/\Gamma}, \tag{42}$$

where Γ is the average bit signal-to-noise ratio, viz:

$$\Gamma = E\{\gamma\}. \tag{43}$$

The average bit error probability for the Rayleigh fading channel with its additive Gaussian noise is[13]

$$P_F = \int_o^\infty f(\gamma)P(\gamma)d\gamma, \tag{44}$$

where

$$P(\gamma) = \frac{1}{2} e^{-\gamma/2}, \tag{45}$$

resulting in

$$P_F = \frac{1}{2 + \Gamma}. \tag{46}$$

Substituting P_F from eq. (46) as P into eq. (20) yields the digital noise power for bit scrambling, NCFSK, and a Rayleigh fading channel, viz:

$$\epsilon^2_{a,F,S} = \sum_{w=1}^{N} \left(\frac{1}{2 + \Gamma}\right)^w \left(1 - \frac{1}{2 + \Gamma}\right)^{N-w} S_w,$$

or $\epsilon^2_{a,F,S}$ may be expressed as

$$\epsilon^2_{a,F,S} = \sum_{w=1}^{N} \frac{T_w}{(2+\Gamma)^w} = \sum_{w=1}^{N} P_F^w T_w, \tag{47}$$

where the subscripts F and S signify a fading channel and the application of bit scrambling, respectively. The term T_w is

$$T_w = \sum_{j=1}^{w} S_w \binom{N-j}{w-j} (-1)^{w-j}; \qquad w = 1, 2, \cdots, N, \tag{48}$$

and S_w can be determined from eqs. (16) through (19). For $P_F \ll 1$, the only value of w that need be considered is 1, and hence

$$\epsilon^2_a = \frac{T_1}{2+\Gamma} = \frac{S_1}{2+\Gamma}. \tag{49}$$

5.1.2 No bit scrambling prior to transmission

We assume that the fading is sufficiently slow for γ to be constant over an N-bit period, i.e., over the duration of one PCM word. The probability of w bits being erroneously regenerated for a particular value of γ is $P(\gamma)^w[1 - P(\gamma)]^{N-w}$. When the bits are not scrambled the average probability of w bits being regenerated erroneously is

$$P_{w,F,\bar{S}} = \int_0^\infty P(\gamma)^w[1 - P(\gamma)]^{N-w} f(\gamma)d\gamma, \tag{50}$$

where the subscripts w, F, $\bar{S}$, signify w bits in error, a fading situation, and no bit scrambling, respectively. Applying a similar procedure to that used in establishing eq. (20) enables us to determine the digital noise power for the Rayleigh fading channel when no bit scrambling is employed, viz:

$$\begin{aligned}\epsilon_{a,F,\bar{S}} &= S_1 \int_0^\infty P(\gamma)[1 - P(\gamma)]^{N-1} f(\gamma)d\gamma \\ &\quad + S_2 \int_0^\infty P(\gamma)^2[1 - P(\gamma)]^{N-2} f(\gamma)d\gamma \\ &\quad + \cdots + S_8 \int_0^\infty P(\gamma)^N f(\gamma)d\gamma \\ &= \sum_{w=1}^{N} P_{w,F,\bar{S}} S_w. \end{aligned} \tag{51}$$

An alternative representation is

$$\epsilon^2_{a,F,\bar{S}} = \sum_{w=1}^{N} T_w \int_o^\infty f(\gamma)P^w(\gamma)d\gamma, \tag{52}$$

where T_w is given by eq. (48). The integral expression in eq. (52) is, from eqs. (42) and (45),

$$\int_o^\infty f(\gamma)P^w(\gamma)d\gamma = \frac{1}{2^{w-1}(2 + \Gamma w)}, \tag{53}$$

and consequently the digital noise power for a slow fading channel and no bit scrambling is

$$\epsilon^2_{a,F,\bar{S}} = \sum_{w=1}^{N} \frac{T_w}{2^{w-1}(2 + \Gamma w)}. \tag{54}$$

5.1.3 Effect of diversity

The average digital noise power formulae will now be derived when diversity is applied, where the type of diversity, e.g., space, frequency, time, polarization, is immaterial. For M-fold diversity reception with ideal maximal-ratio combining, the PDF of the channel s/n γ is[13]

$$f(\gamma) = \frac{\gamma^{M-1}e^{-\gamma/\Gamma}}{\Gamma^M(M-1)!}. \tag{55}$$

If the receiver selects the diversity branch having the strongest signal level the diversity scheme is known as ideal selection combining for which the PDF is[13]

$$f(\gamma) = \frac{M}{\Gamma} e^{-\gamma/\Gamma}(1 - e^{-\gamma/\Gamma})^{(M-1)}. \tag{56}$$

5.1.3.1 Bit scrambling employed. Substituting $f(\gamma)$ from eq. (55) and $P(\gamma)$ from eq. (45) into eq. (44) gives the average bit error probability. When this probability is substituted in eq. (47) the digital noise for the ideal maximal-ratio combining becomes

$$\epsilon^2_{a,F,S,D} = \sum_{w=1}^{N} T_w \left[\frac{2^{M-1}}{(2 + \Gamma)^M}\right]^w, \tag{57}$$

where the subscript D signifies the application of diversity reception.

When the process is repeated using $f(\gamma)$ from eq. (56), the digital noise power for ideal selection combining is obtained, viz:

$$\epsilon^2_{a,F,S,D} = \left[\sum_{w=1}^{N} T_w \quad \frac{M}{2\Gamma} \sum_{j=0}^{M-1} (-1)^j \binom{M-1}{j} \frac{1}{\left(\frac{1}{\Gamma} + \frac{j}{\Gamma} + \frac{1}{2}\right)}\right]^w. \tag{58}$$

5.1.3.2 No bit scrambling prior to transmission. When ideal maximal-ratio combining is employed, application of eqs. (45) and (55) yields

$$\int_o^\infty P^w(\gamma)f(\gamma)d\gamma = \frac{2^{M-w}}{(2 + \Gamma w)^M} \tag{59}$$

for NCFSK modulation. The digital noise power is then determined to be

$$\epsilon^2_{a,F,\bar{S},D} = \sum_{w=1}^{N} T_w \frac{2^{M-w}}{(2 + \Gamma w)^M}. \tag{60}$$

For ideal selection combining the expression

$$\int_o^\infty P^w(\gamma) f(\gamma) d\gamma = \frac{M}{\Gamma 2^w} \sum_{j=0}^{M-1} (-1)^j \binom{M-1}{j} \frac{1}{\left(\frac{1}{\Gamma} + \frac{j}{\Gamma} + \frac{w}{2}\right)} \tag{61}$$

is established by means of eqs. (45) and (56) and the application of the technique described in Ref. 14. The digital noise power for the situation described here is

$$\epsilon^2_{a,F,\bar{S},D} = \sum_{w=1}^{N} \frac{MT_w}{\Gamma 2^w} \sum_{j=0}^{M-1} (-1)^j \binom{M-1}{j} \frac{1}{\left(\frac{1}{\Gamma} + \frac{j}{\Gamma} + \frac{w}{2}\right)}. \tag{62}$$

5.2 Digital noise power with CPSK modulation

The differences in the digital noise power of the PCM system using CPSK and NCFSK modulation are due to the differences of their probability of bit error. For CPSK the probability of bit error as a function of channel s/n is[15]

$$P(\gamma) = Q(\sqrt{2\gamma}). \tag{63}$$

The distribution functions for the channel s/n's are given by eqs. (55) and (56) for the case of maximal-ratio-combining diversity and ideal selection-combining diversity, respectively. When bit scrambling is performed prior to transmission, the average bit error probability is computed using eq. (44), where $P(\gamma)$ is given by eq. (63), and $f(\gamma)$ is selected from either eq. (55) or (56). This average bit error probability is substituted into eq. (47) to give the digital noise power, from which, with the aid of eq. (11) $\widehat{s/n}$ is formulated.

When the bits are not scrambled, the digital noise power is found by substituting $P(\gamma)$ from eq. (63), and $f(\gamma)$ from either eq. (55) or (56) directly into eq. (52). With the aid of eqs. (52) and (11), $\widehat{s/n}$ is determined.

VI. MINIMUM DISTANCE CODE PCM

The folded binary PCM code has its msb as the polarity of the encoded sample, while the remaining bits constitute the magnitude of the sample. In natural binary code the most negative sample is given an all-zero pattern, and binary numbering of progressively more pos-

itive samples ensues until the most positive sample is reached, which is assigned an all-one code. A single error in these codes can produce large errors in the recovered samples. The Gray code is also vulnerable to transmission errors, although the magnitude of the errors is not as large as those encountered when the folded binary and natural binary codes are employed.

The Minimum Distance Code (MDC) was conceived by Rydbeck and Sundberg.[3] The word distance in this code name refers to the difference between a recovered sample correctly received and its value when subjected to a single bit error. The MDC has the property of asymptotic minimum digital noise for low-level speech samples, and the abbreviation may also be taken as minimum digital noise code. The structure of the code is based on the error sequencies discussed in Section II. The msb represents the polarity of the quantized sample, being logical 0 for positive samples and logical 1 for negative samples. Table I shows the seven-bit magnitude code for 8-bit PCM. For quantized level number y_i of zero we have an all-zero word. The code words for $y_i = 1$ to 7 are the single error patterns when the Hamming weight w is unity. The next group is the double error ($w = 2$) patterns having 21 components extending from $y_i = 8$ to 28 inclusive. The code progresses, having 35 triple-error sequencies, $w = 3$, and so on until the final all logical 1 code when $w = 7$. The number code words in each group represented by the Hamming weight w are

$$\binom{N-1}{w}.$$

The MDC code is specifically designed to accommodate low-level input signals. When single bit errors occur the code can only change to an adjacent group. Changes involving half the magnitude range that occurs in folded binary PCM are forbidden. However, errors in the least significant bits will in general cause much larger errors in the recovered sample than in folded binary. We therefore trade the large erroneous spikes in the recovered signal that occur in folded binary PCM for smaller spikes that happen more frequently in MDC.

VII. PERFORMANCE

The input range of the quantizer was from −1 to +1, and in our theoretical calculations the input signal was assumed to have an exponential PDF with standard deviation of either $\sqrt{2}/10$ (−17 dB), or 0.01 (−40 dB). The 8-bit μ-law PCM encoder, $\mu = 255$, was arranged to operate at input signal powers of −17 dB and −40 dB, the former being indicative of high-level speech and the latter of low-level speech. Three binary codes were considered initially—Natural Binary Code

Table I—The MDC code for 8-bit PCM (the polarity bit is not shown)

Quantized Level Number	Magnitude Code of MDC							w
127	1	1	1	1	1	1	1	7
126	1	1	1	1	1	1	0	6
125	1	1	1	1	1	0	1	6
124	1	1	1	1	0	1	1	6
123	1	1	1	0	1	1	1	6
122	1	1	0	1	1	1	1	6
121	1	0	1	1	1	1	1	6
120	0	1	1	1	1	1	1	6
119	1	1	1	1	1	0	0	5
118	1	1	1	1	0	1	0	5
117	1	1	1	0	1	1	0	5
116	1	1	0	1	1	1	0	5
115	1	0	1	1	1	1	0	5
114	0	1	1	1	1	1	0	5
113	1	1	1	1	0	0	1	5
112	1	1	1	0	1	0	1	5
111	1	1	0	1	1	0	1	5
110	1	0	1	1	1	0	1	5
109	0	1	1	1	1	0	1	5
108	1	1	1	0	0	1	1	5
107	1	1	0	1	0	1	1	5
106	1	0	1	1	0	1	1	5
105	0	1	1	1	0	1	1	5
104	1	1	0	0	1	1	1	5
103	1	0	1	0	1	1	1	5
102	0	1	1	0	1	1	1	5
101	1	0	0	1	1	1	1	5
100	0	1	0	1	1	1	1	5
99	0	0	1	1	1	1	1	5
98	1	1	1	1	0	0	0	4
97	1	1	1	0	1	0	0	4
96	1	1	0	1	1	0	0	4
95	1	0	1	1	1	0	0	4
94	0	1	1	1	1	0	0	4
93	1	1	1	0	0	1	0	4
92	1	1	0	1	0	1	0	4
91	1	0	1	1	0	1	0	4
90	0	1	1	1	0	1	0	4
89	1	1	0	0	1	1	0	4
88	1	0	1	0	1	1	0	4
87	0	1	1	0	1	1	0	4
86	1	0	0	1	1	1	0	4
85	0	1	0	1	1	1	0	4
84	0	0	1	1	1	1	0	4
83	1	1	1	0	0	0	1	4
82	1	1	0	1	0	0	1	4
81	1	0	1	1	0	0	1	4
80	0	1	1	1	0	0	1	4
79	1	1	0	0	1	0	1	4
78	1	0	1	0	1	0	1	4
77	0	1	1	0	1	0	1	4
76	1	0	0	1	1	0	1	4
75	0	1	0	1	1	0	1	4
74	0	0	1	1	1	0	1	4
73	1	1	0	0	0	1	1	4
72	1	0	1	0	0	1	1	4
71	0	1	1	0	0	1	1	4
70	1	0	0	1	0	1	1	4
69	0	1	0	1	0	1	1	4
68	0	0	1	1	0	1	1	4
67	1	0	0	0	1	1	1	4
66	0	1	0	0	1	1	1	4
65	0	0	1	0	1	1	1	4
64	0	0	0	1	1	1	1	4
63	1	1	1	0	0	0	0	3
62	1	1	0	1	0	0	0	3
61	1	0	1	1	0	0	0	3
60	0	1	1	1	0	0	0	3
59	1	1	0	0	1	0	0	3
58	1	0	1	0	1	0	0	3
57	0	1	1	0	1	0	0	3
56	1	0	0	1	1	0	0	3
55	0	1	0	1	1	0	0	3
54	0	0	1	1	1	0	0	3
53	1	1	0	0	0	1	0	3
52	1	0	1	0	0	1	0	3
51	0	1	1	0	0	1	0	3
50	1	0	0	1	0	1	0	3
49	0	1	0	1	0	1	0	3
48	0	0	1	1	0	1	0	3
47	1	0	0	0	1	1	0	3
46	0	1	0	0	1	1	0	3
45	0	0	1	0	1	1	0	3
44	0	0	0	1	1	1	0	3
43	1	1	0	0	0	0	1	3
42	1	0	1	0	0	0	1	3
41	0	1	1	0	0	0	1	3
40	1	0	0	1	0	0	1	3
39	0	1	0	1	0	0	1	3
38	0	0	1	1	0	0	1	3
37	1	0	0	0	1	0	1	3
36	0	1	0	0	1	0	1	3
35	0	0	1	0	1	0	1	3
34	0	0	0	1	1	0	1	3
33	1	0	0	0	0	1	1	3
32	0	1	0	0	0	1	1	3
31	0	0	1	0	0	1	1	3
30	0	0	0	1	0	1	1	3
29	0	0	0	0	1	1	1	3
28	1	1	0	0	0	0	0	2
27	1	0	1	0	0	0	0	2
26	0	1	1	0	0	0	0	2
25	1	0	0	1	0	0	0	2
24	0	1	0	1	0	0	0	2
23	0	0	1	1	0	0	0	2
22	1	0	0	0	1	0	0	2
21	0	1	0	0	1	0	0	2
20	0	0	1	0	1	0	0	2
19	0	0	0	1	1	0	0	2
18	1	0	0	0	0	1	0	2
17	0	1	0	0	0	1	0	2
16	0	0	1	0	0	1	0	2
15	0	0	0	1	0	1	0	2

Table I—*Continued*

Quantized Level Number	Magnitude Code of MDC							w	Quantized Level Number	Magnitude Code of MDC							w
14	0	0	0	0	1	1	0	2	6	0	1	0	0	0	0	0	1
13	1	0	0	0	0	0	1	2	5	0	0	1	0	0	0	0	1
12	0	1	0	0	0	0	1	2	4	0	0	0	1	0	0	0	1
11	0	0	1	0	0	0	1	2	3	0	0	0	0	1	0	0	1
10	0	0	0	1	0	0	1	2	2	0	0	0	0	0	1	0	1
9	0	0	0	0	1	0	1	2	1	0	0	0	0	0	0	1	1
8	0	0	0	0	0	1	1	2	0	0	0	0	0	0	0	0	0
7	1	0	0	0	0	0	0	1									

(NBC), Folded Binary Code (FBC), and Minimum Distance Code (MDC)—but it soon transpired that NBC was considerably inferior to the others and was abandoned. In Table II we display the single-error A-factors and the T-factors of eqs. (25) and (48), respectively. The input signal has an exponential PDF specified by eq. (24), and the codec is 8-bit μ-law PCM, $\mu = 255$. The factors $A_1, A_2, \cdots, A_8$ are associated with single errors in the first, second, $\cdots$, lsb, respectively. The entries in the table illustrate that the variation between the A-factors is significantly smaller for MDC than for FBC. Consequently, the digital noise power due to single bit errors per word when the MDC code is used is similar for all bit locations in the words. This situation is radically different when FBC is employed. For low-level speech the factor T_1 for MDC is significantly smaller than its counterpart with FBC. When the input level is high, the T_1 factors are approximately the same. Unlike the case of linear PCM with FBC, where T_3 to T_8 are zero,[16] the T-factors with companded PCM are nonzero.

The types of modulation employed in our analysis were NCFSK and CPSK. The quantization noise power ϵ_q^2 and clipping noise power ϵ_c^2 were determined for the input powers of -17 and -40 dB in the absence of transmission errors. The digital noise power ϵ_a^2 was computed using the equations in Sections IV and V. Armed with knowledge of these noise powers we were able to compute the theoretical overall s/n, namely $\widehat{s/n}$, as expressed by eq. (11). As ϵ_a^2 is a function of channel s/n, the variation of $\widehat{s/n}$ with channel s/n was determined.

In addition to presenting these theoretical variations of $\widehat{s/n}$, we also conducted simulations using speech signals. In our experiments we used four concatenated sentences: "Glue the sheet to the dark blue background," "Rice is often served in round bowls," "Four hours of steady work faced us," and "The box was thrown beside the parked truck." The first two sentences were spoken by females, the others by males. The speech was bandlimited between 200 and 3200 Hz, and sampled at 8 kHz to give the speech sequence used in our simulations.

Table II—The single error A- and T-factors for 8-bit μ-law PCM, $\mu = 255$; the input PDF is exponential

	A_1	A_2	A_3	A_4	A_5	A_6	A_7	A_8
−40 dB/FBC	3.954e-4	3.783e-2	6.375e-4	1.105e-4	2.184e-5	5.176e-6	1.277e-6	3.181e-7
−40 dB/MDC	3.954e-4	2.486e-3	2.220e-3	1.982e-3	1.632e-3	1.161e-3	5.833e-4	1.389e-4
−17 dB/FBC	0.07906	0.1391	0.08739	0.01331	2.644e-3	6.281e-4	1.550e-4	3.863e-5
−17 dB/MDC	0.07906	0.05214	0.04879	0.04554	0.04118	0.3434	0.02405	0.01009
	T_1	T_2	T_3	T_4	T_5	T_6	T_7	T_8
−40 dB/FBC	0.03900	0.2871	4.914e-3	−4.108e-2	2.155e-4	6.056e-5	3.576e-7	−1.788e-7
−40 dB/MDC	0.01060	0.3019	0.3811	−1.024	0.9891	−0.4009	0.03743	−4.965e-3
−17 dB/FBC	0.3223	−0.1182	−0.2133	0.06660	0.003221	−1.976e-4	2.980e-7	−1.192e-7
−17 dB/MDC	0.3352	−0.06155	−0.7784	1.480	−1.660	1.052	−0.4118	0.1041

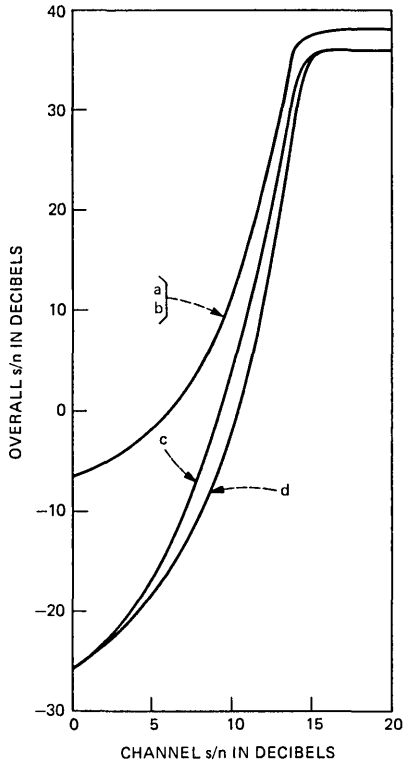

Fig. 6—Gaussian channel. Theoretical curves of overall s/n against channel s/n for NCFSK modulation (a) −17 dB input power, MDC; (b) −17 dB input power, FBC; (c) −40 dB input power, MDC; and (d) −40 dB input power, FBC.

7.1 Gaussian channel

The theoretical curves of $\hat{s}/n$ versus channel s/n when NCFSK modulation was employed are displayed in Fig. 6. When the input signal power was −17 dB there was negligible difference between the curves corresponding to FBC and MDC binary codes. Reducing the input signal power to −40 dB revealed differences in the two codes, with MDC producing a gain in $\hat{s}/n$ compared to FBC of up to 4 dB for a given channel s/n.

The theoretical results for CPSK, shown in Fig. 7, are essentially the same as for NCFSK, except that the curves are shifted by approximately 4 dB to lower values of channel s/n. When speech was used in the simulation, the modulation being CPSK, the results are those shown in Fig. 8. The curves in this figure were shifted by approximately 2.5 dB to higher values of channel s/n compared to the theoretical curves. The deterioration in performance compared to the theoretical curves occurs because of the diverse nature of speech with its voiced

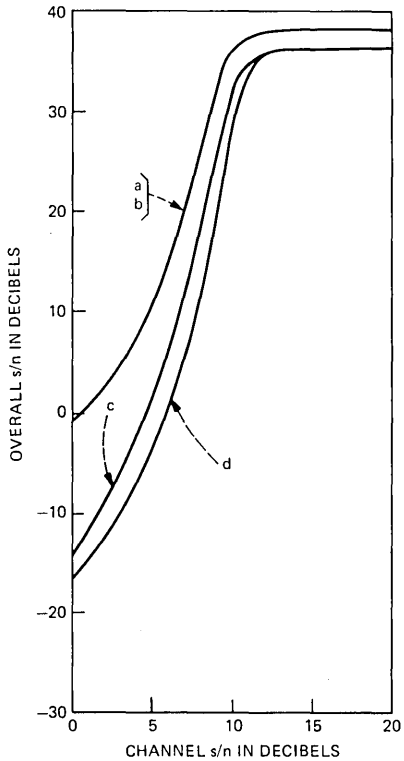

Fig. 7—Gaussian channel. Theoretical curves of overall s/n against channel s/n for CPSK modulation (a) −17 dB input power, MDC; (b) −17 dB input power, FBC; (c) −40 dB input power, MDC; and (d) −40 dB input power, FBC.

and unvoiced sections, and its intraword and interword silences. The theoretical curves apply to input signals having exponential PDFs, while speech is notorious for its nonstationary statistics. Nevertheless, sources having exponential PDFs are often used to represent speech, and clearly the theoretical and speech curves do have similar shapes, albeit their difference in absolute $\hat{s}/n$ for a given channel s/n. This curve similarity is particularly evident when we compare the performances of FBC and MDC at input levels of −17 and −40 dB.

7.2 Rayleigh fading channel

Figure 9 shows the variation of $\hat{s}/n$ as a function of channel s/n for a Rayleigh fading channel and for CPSK modulation. The theoretical curves in this figure relate to a number of conditions. For each of the two input power levels of −17 dB and −40 dB, we computed the curves for FBC and MDC when the bits were scrambled prior to transmission and when no scrambling was performed. The four curves, a, b, c, and

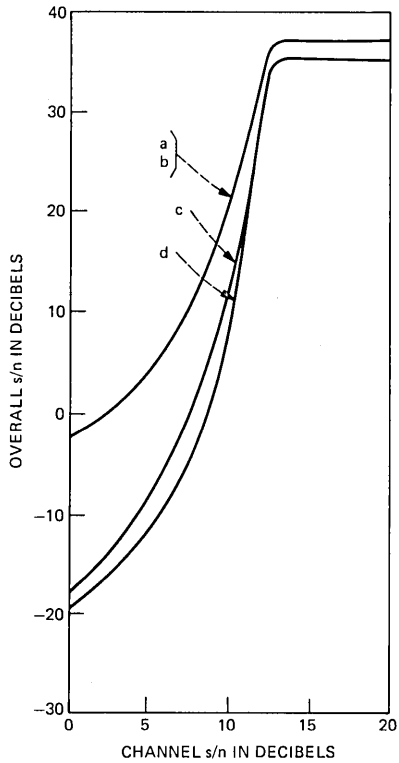

Fig. 8—Gaussian channel. Speech simulation curves of overall s/n against channel s/n for CPSK modulation (a) −17 dB input power, MDC; (b) −17 dB input power, FBC; (c) −40 dB input power, MDC; and (d) −40 dB input power, FBC.

d, coaleased for the input power of −17 dB. For a channel s/n of 30 dB, and the lower input power, MDC had a $\hat{s}/n$ advantage of 5 dB over FBC when bit scrambling was performed, and only a 0.8-dB gain in $\hat{s}/n$ in the absence of bit scrambling. We observed that MDC with bit scrambling, curve e, had a gain in $\hat{s}/n$ of 9 dB compared to curve h, where FBC without bit scrambling was employed. These gains in $\hat{s}/n$ are valid for channel s/n values where $\hat{s}/n > 0$ dB.

We also computed the theoretical curves for NCFSK, and we obtained curves that were almost identical to those shown in Fig. 9 but shifted by 6 dB to higher values of channel s/n. As with CPSK, over most of the range of channel s/n the curves are parallel, indicating that as the Bit Error Rate (BER) increases the relative performance of the different codes is unchanged.

7.2.1 PCM speech over mobile radio channels

The μ-law PCM encoded speech was allowed to two-level CPSK

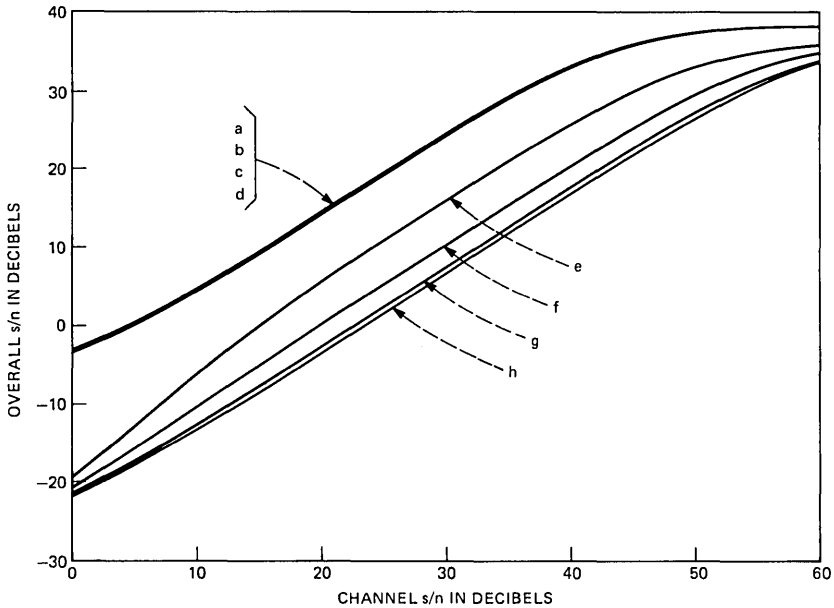

Fig. 9—Rayleigh fading channel. Theoretical curves of overall s/n against channel s/n for nondiversity CPSK modulation: (a) −17 dB input power, bit scrambling, MDC; (b) −17 dB input power, bit scrambling, FBC; (c) −17 dB input power, no bit scrambling, MDC; (d) −17 dB input power, no bit scrambling, FBC; (e) −40 dB input power, bit scrambling, MDC; (f) −40 dB input power, bit scrambling, FBC; (g) −40 dB input power, no bit scrambling, MDC; and (h) −40 dB input power, no bit scrambling, FBC.

modulate an RF carrier. A sequence of the envelope function $A(t)$ was generated from a hardware simulator of frequency-selective Rayleigh-fading mobile radio paths.[17] The $A(t)$ signal was sampled at 32 kHz and inserted into the computer to provide the fading envelope of a vehicle traveling at 15 mph. By resampling $A(t)$ we were able to produce fading envelopes for different vehicular speeds. The CPSK signal was subjected to these fading envelopes and corrupted by cochannel interference. The recovered baseband signal was sampled at the PCM bit rate to produce at the kth instant,[17]

$$B_k = R_k b_k + I_k, \tag{64}$$

where R_k, b_k, and I_k were the amplitudes of the Rayleigh envelope, transmitted bit, and additive interference level, respectively. The regenerated bit, $\hat{b}_k$, was a logical one if $B_k \geqslant 0$; otherwise it was a logical zero. The bits were grouped into PCM words and decoded using μ-law PCM. The difference between the input speech sequence and the decoded PCM sequence yielded the error sequence. The over s/n was then computed.

Figure 10 shows the variation of the $\hat{s}/n$ for our speech signal as a

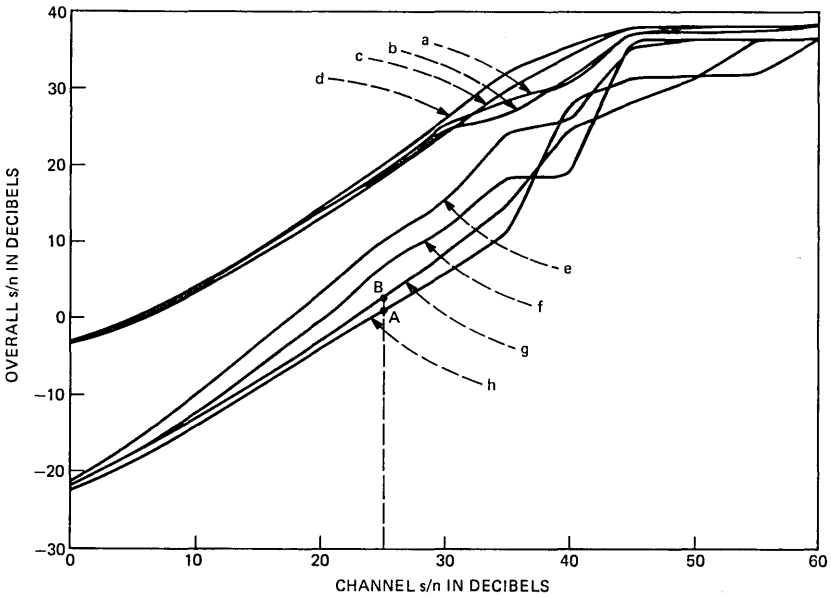

Fig. 10—Mobile radio channel. Speech simulation curves of overall s/n against channel s/n for nondiversity CPSK modulation with a vehicular speed of 30 mph. Curve labels are as in Fig. 9.

function of the channel s/n, for a vehicular speed of 30 mph. Eight curves are displayed corresponding to those used in Fig. 9. The curves of Fig. 10 have the same general shape as those of Fig. 9. We repeated our experiment for vehicular speeds of 60 mph, and overlaid the curves for this speed with those shown in Fig. 10. The fit for the high input levels was fairly exact, but for the −40 dB input level there were substantial discrepancies. Had we been able to take sufficiently long segments of speech and channel variations, our curves at −40 dB would have approached those in Fig. 9, subject to the inherent discrepancy that speech does not have the exponential distribution assumed for the theoretical case. The greater variations in the slopes of the curves of Fig. 10 compared to those in Fig. 9 at the −40 dB input level compared to the −17 dB level is to be expected, since for the same error rate the effect of an error can have a much greater influence on $\hat{s}/n$ when the input level is low.

We display in Fig. 11 a segment of the original input speech waveform, and the corresponding recovered waveforms obtained for conditions marked *A* and *B* in Fig. 10, respectively. The characteristic large error spikes associated with FBC are evident in Fig. 11b, where a spike can exceed half the amplitude range of the input speech signal. The nature of the MDC is to cause small spikes when the input speech

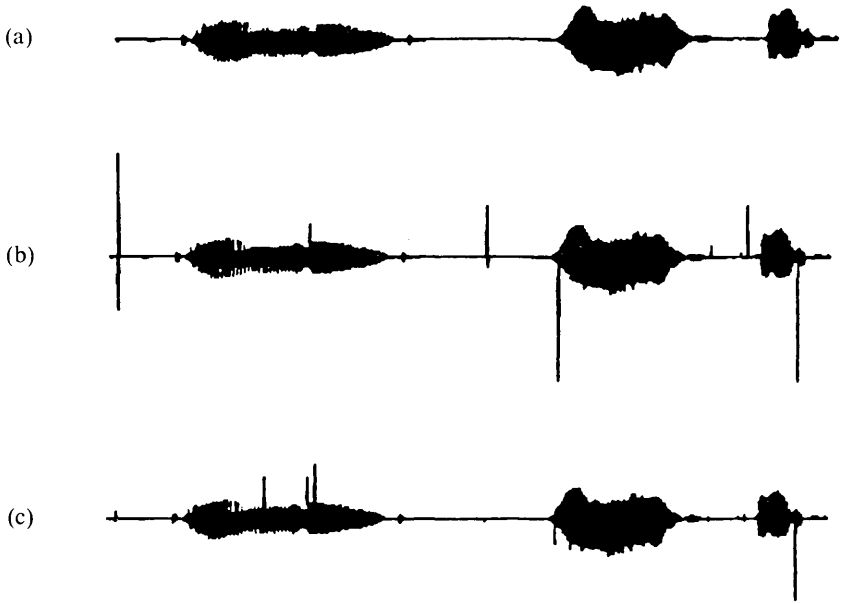

Fig. 11—μ-law PCM speech waveforms for mobile radio channels, nondiversity CPSK, vehicular speed 30 mph, −40 dB input power level, 25-dB channel s/n, and no bit scrambling: (a) original speech; (b) recovered speech with FBC (point A in Fig. 10); and (c) recovered speech with MDC (point B in Fig. 10).

samples are small, or indeed, when they are very large (see Table I and Fig. 11c). Errors in samples quantized to the middle of the range are responsible for the largest spikes with MDC.

7.2.2 Effect of diversity

When 2-branch ($M = 2$) diversity is applied, the value of $\hat{s}/n$ depends upon whether we use ideal maximum-ratio-combining diversity (IMRCD), or ideal selection-combining diversity (ISCD). Figure 12 displays the variation of $\hat{s}/n$ against channel s/n for numerous conditions, the modulation being CPSK. We observe that IMRCD is preferable to ISCD, that MDC coupled with bit scrambling is the best of our choices at the −40 dB input level, and that the curves have the same form as for $M = 1$ (see Fig. 9), except that the system can now operate at significantly lower values of channel s/n.

We do not show the theoretical curves for NCFSK for $M = 2$. Suffice it to say that they are virtually identical to those of CPSK, $M = 2$, except for a shift of 6 dB to higher values of channel s/n.

For the mobile radio channel described in Section 7.2.1 the curves of Fig. 13 were obtained. For reasons of clarity, we show only those curves with bit scrambling. These results are similar to those in Fig.

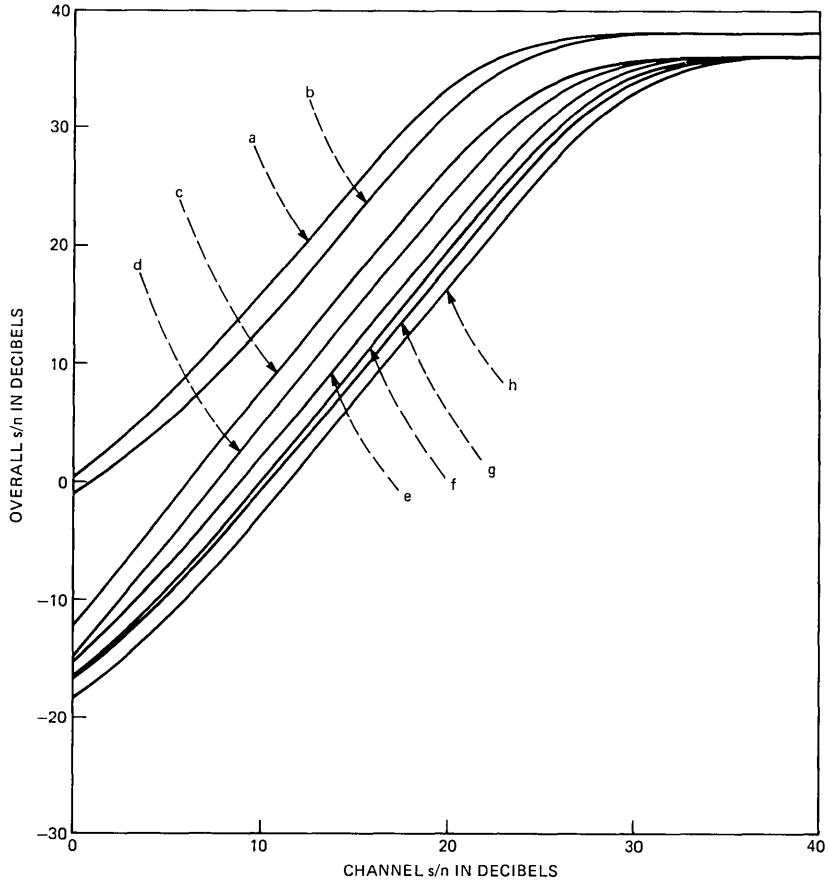

Fig. 12—Rayleigh fading channel (2-branch diversity). Theoretical curves of overall s/n against channel s/n for CPSK modulation: (a) −17 dB input power, IMRCD, bit scrambling and no bit scrambling, FBC, and MDC; (b) −17 dB input power, ISCD, bit scrambling and no bit scrambling, FBC, and MDC; (c) −40 dB input power, IMRCD, bit scrambling, MDC; (d) −40 dB input power, ISCD, bit scrambling, MDC; (e) −40 dB input power, IMRCD, bit scrambling, FBC, also no bit scrambling, MDC; (f) −40 dB input power, IMRCD, no bit scrambling, FBC; (g) −40 dB input power, ISCD, bit scrambling, FBC, also no bit scrambling, MDC; and (h) −40 dB input power, ISCD, no bit scrambling, FBC.

12, where the somewhat erratic behavior of the curves at the lower input power level is attributable to the reasons discussed in connection with the corresponding curves in Fig. 10.

The effect of using different values of M on the theoretical $\hat{s/n}$ is displayed in Fig. 14 for NCFSK, an input power level of −17 dB, MDC, bit scrambling, and IMRCD and ISCD. As M is increased, the knee of the curves moves to lower values of channel s/n, and the advantage of using IMRCD over ISCD increases. Figure 15 shows the

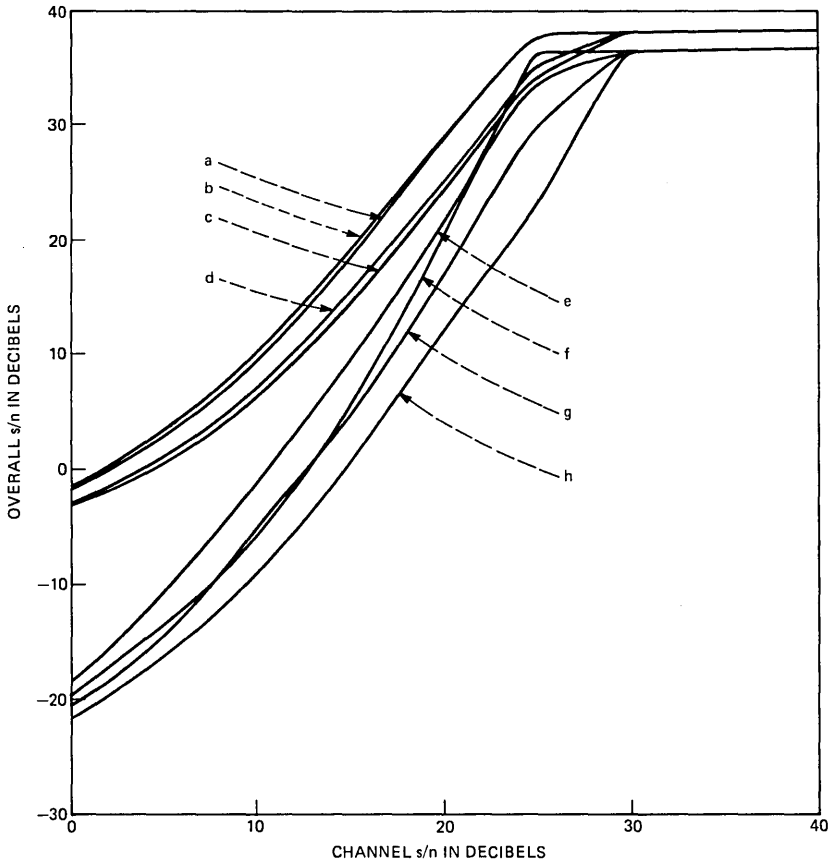

Fig. 13—Mobile radio channel. Speech simulation curves of overall s/n against channel s/n for CPSK modulation. The vehicular speed is 30 mph, with 2-branch diversity and bit scrambling employed: (a) −17 dB input power, IMRCD, MDC; (b) −17 dB input power, IMRCD, FBC; (c) −17 dB input power, ISCD, MDC; (d) −17 dB input power, ISCD, FBC; (e) −40 dB input power, IMRCD, MDC; (f) −40 dB input power, IMRCD, FBC; (g) −40 dB input power, ISCD, MDC; and (h) −40 dB input power, ISCD, FBC.

theoretical curves for the same conditions using CPSK instead of NCFSK. Again we note the close correspondence between the curves if a lateral shift in channel s/n is made.

VIII. DISCUSSION

Digital noise in μ-law PCM systems has been examined for both Gaussian and Rayleigh fading channels. Theoretical results for the digital noise power, i.e., the noise power in the decoded signal, have been presented for both NCFSK and CPSK modulation. Underpinning this theory is the application of the A-factors, and accordingly we have

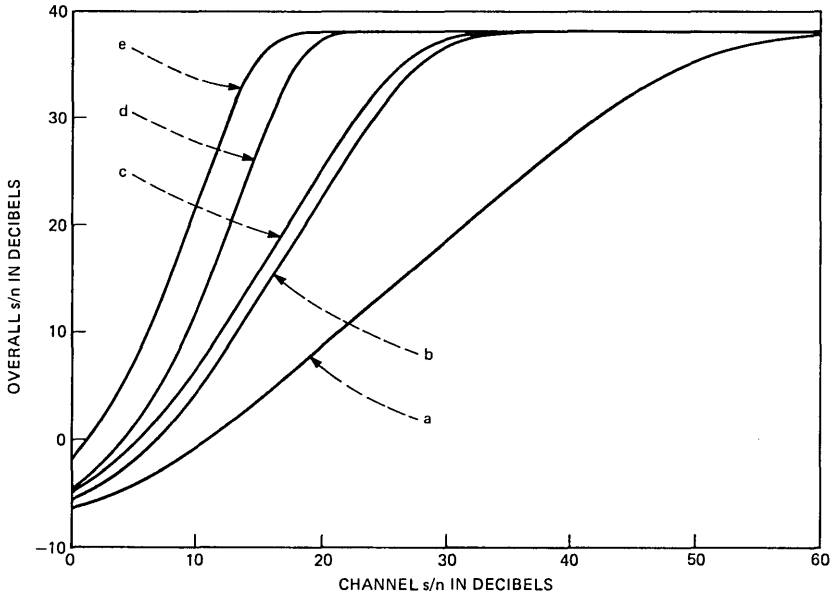

Fig. 14—Effect of diversity on Rayleigh fading channels. Theoretical cuves of overall s/n against channel s/n for −17 dB input power, NCFSK modulation, bit scrambling: (a) no diversity; (b) ISCD (M = 2); (c) IMRCD (M = 2); (d) ISCD (M = 4); and (e) IMRCD (M = 4).

elucidated their significance in detail. Armed with knowledge of the A-factors the determination of the digital noise power is greatly simplified [see eq. (9)]. We emphasize that although we have concentrated our attention on μ-law PCM, the A-factor approach is equally valid for A-law PCM. For this case the A-factors are computed by replacing the μ-law eqs. (29) and (30) by the A-law equations,[1,4] and proceeding as before.

Two binary codes for the μ-law PCM words were investigated: folded binary code (FBC) and minimum distance code (MDC). The MDC code yielded significant gains in $\hat{s}/n$ compared to FBC, with the proviso that the input power level was low. This is readily apparent upon inspection of Figs. 6 through 13. In our deliberations on Rayleigh fading channels we considered the effect of scrambling the bits in the PCM sequence prior to transmission, and compared it to the situation when bit scrambling was not employed. At low input power levels bit scrambling produced a gain of 8 dB when MDC was used, as shown in Fig. 9. The application of diversity made a significant contribution to system performance, and our best results occurred when we used a combination of ideal maximal-ratio-combining diversity, bit scrambling, and MDC binary code.

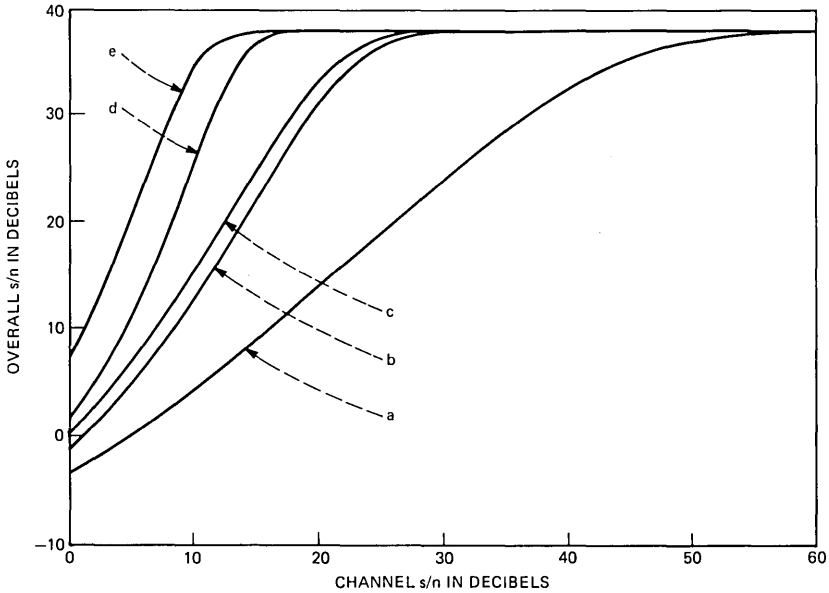

Fig. 15—Effect of diversity on Rayleigh fading channels. Same conditions as in Fig. 14, except that CPSK modulation is used.

Four concatenated sentences of speech were used in our simulations, and we have shown in our figures that there is consistency in the shape of the simulated and theoretical curves. In particular, at the higher input level the simulated and theoretical $\hat{s}/n$ values agree to within a couple of decibels, but for second-order diversity the discrepancy is $\simeq 4$ dB. These departures from the theory are a consequence of deriving our formulae for an input signal having an exponential PDF. Speech, by contrast, has time-varying statistics. However, voiced speech constitutes nearly 80 percent of speech, and its PDF can be approximated by an exponential one. It is for this reason that we used the exponential PDF in our theoretical deliberations.

REFERENCES

1. K. W. Cattermole, *Principles of Pulse Code Modulation*, London: Iliffe, 1969.
2. J. L. Flanagan, M. R. Schroeder, B. S. Atal, R. E. Crochiere, N. S. Jayant, and J. M. Tribolet, "Speech Coding," IEEE Trans. Commun., *COM-27* (April 1979), pp. 710–37.
3. N. Rydbeck and C.-E. Sundberg, "Analysis of Digital Errors in Non-Linear PCM Systems," IEEE Trans. Commun., *COM-24*, No. 1 (January 1976), pp. 59–65.
4. C.-E. Sundberg, "The Effect of Single Bit Errors in Standard Nonlinear PCM Systems," IEEE Trans. Commun., *COM-24*, No. 9 (September 1976), pp. 1062–4.
5. C.-E. Sundberg and N. Rydbeck, "Pulse Code Modulation With Error-Correcting Codes for TDMA Satellite Communication Systems," Ericsson Technics, *32*, No. 1 (1976), pp. 3–56.

6. N. Rydbeck and C.-E. Sundberg, "PCM/TDMA Satellite Communication Systems With Error-Correcting and Error-Detecting Codes," Ericsson Technics, *32*, No. 3 (1976), pp. 195–247.
7. E. Bedrosian, "Weighted PCM," IRE Trans. Inform. Theory, *IT-4* (March 1958), pp. 45–9.
8. C.-E. Sundberg, "Optimum Weighted PCM for Speech Signals," IEEE Trans. Commun., *COM-26*, No. 6 (June 1978), pp. 872–81.
9. C.-E. Sundberg, W. C. Wong, and R. Steele, "Weighting Strategies for Companded PCM Transmitted Over Rayleigh Fading and Gaussian Channels," AT&T Bell Lab. Tech. J, *63*, No 4 (April 1984), pp. 587–626.
10. R. Steele and D. J. Goodman, "Detection and Selective Smoothing of Transmission Errors in Linear PCM," B.S.T.J., *56*, No. 3 (March 1977), pp. 399–409.
11. R. Steele, "Partial Removal of Transmission Errors in Digitally Encoded Speech," Electronics and Power, *24*, No. 6 (June 1978), pp. 451–4.
12. C.-E. Sundberg, "Soft Decision Demodulation for PCM Encoding Speech Signals," IEEE Trans. Commun. *COM-26* (June 1978), pp. 854–9.
13. W. C. Y. Lee, *Mobile Communication Engineering*, New York: McGraw-Hill, 1982.
14. C.-E. Sundberg, "Block Error Probability for Non-Coherent FSK with Diversity for Very Slow Rayleigh Fading in Gaussian Noise," IEEE Trans. Commun., *COM-29*, No. 1 (January 1981), pp. 57–60.
15. A. P. Clark, *Principles of Digital Data Transmission*, London: Pentech Press, 1976.
16. D. J. Goodman and C.-E. Sundberg, "Transmission Errors and Forward Error Correction in Embedded Differential Pulse Code Modulation," B.S.T.J., *62*, No. 9 (November 1983), pp. 2735–64.
17. W. C. Wong, R. Steele, B. Glance, and D. Horn, "Time Diversity With Adaptive Error Detection to Combat Rayleigh Fading in Digital Mobile Radio," IEEE Trans. Commun., *COM-31*, No. 3 (March 1983), pp. 378–87.

AUTHORS

Raymond Steele, (SM '80), B.S. (Electrical Engineering) from Durham University, Durham, England, in 1959, the Ph.D. degree in 1975, and the Doctor of Science Degree (DSc) in 1983. Prior to his enrollment at Durham University, he was an indentured apprenticed Radio Engineer. After research and development posts at E. K. Cole Ltd., Cossor Radar and Electronics, Ltd., and The Marconi Company, all in Essex, England, he joined the lecturing staff at the Royal Naval College, Greenwich, London, England. Here he lectured in telecommunications to NATO and the External London University degree courses. His next post was as Senior Lecturer in the Electronic and Electrical Engineering Department of Loughborough University, Loughborough, Leics., England, where he directed a research group in digital encoding of speech and television signals. In 1975 his book, *Delta Modulation Systems* (Pentech Press, London), was published. He was a consultant to the Acoustics Research Department at Bell Laboratories in the summers of 1975, 1977, and 1978, and in 1979 he joined the company's Communications Methods Research Department, Crawford Hill Laboratory, Holmdel, N.J. In 1983 he became Professor of Communications in the Electronics Department at the University of Southampton, England.

Carl-Erik W. Sundberg, M.S.E.E., 1966, and Dr. Techn., 1975, Lund Institute of Technology, University of Lund, Sweden; Bell Laboratories, 1981–1982. Mr. Sundberg is an Associate Professor in the Department of Telecommunication Theory, University of Lund, and a consultant in his field. He is Director of the consulting company SUNCOM, Lund. During 1976 he was with the European Space Research and Technology Centre (ESTEC), Noordwijk, The Netherlands, as an ESA Research Fellow. He has been a Consulting Scientist at LM Ericsson and SAAB-SCANIA, Sweden, and at AT&T Bell Laboratories. His research interests include source coding, channel coding

(especially decoding techniques), digital modulation methods, fault-tolerant systems, digital mobile radio systems, spread spectrum systems, and digital satellite communication systems. He has published a large number of papers in these areas during the last few years. Senior Member, IEEE; member, SER, Sveriges Elektroingenjörers Riksförening.

Wai Choong (Lawrence) Wong, B.Sc.(Hons.) 1976, and Ph.D. 1980, in Electronic and Electrical Engineering, Loughborough University of Technology, U.K.; Bell Laboratories, 1980–83; from 1980 to 1983 Mr. Wong was with the Communications Methods Research Department at Bell Laboratories, working on speech enhancement, simultaneous transmission of speech and data, fading channel response modeling, and digital modulation techniques. In 1983 he joined the National University of Singapore as a lecturer. His current interests include digital speech and video signal processing, mobile radio communications, and digital modulation techniques.

AT&T Bell Laboratories Technical Journal
Vol. 63, No. 6, July-August 1984
Printed in U.S.A.

Overtone Absorption and Raman Spectra of H_2 and D_2 in Silica Optical Fibers

By J. STONE,* A. R. CHRAPLYVY,* J. M. WIESENFELD,* and C. A. BURRUS*

(Manuscript received February 29, 1984)

We have recorded quantitative optical absorption and Raman spectra of H_2 and D_2 diffused into silica optical fibers at a pressure of 500 atm. The absorption spectra recorded were fundamental through the third overtone for H_2 (0.6 through 2.5 μm) and the first through fourth overtone for D_2 (0.7 through 1.7 μm). The observed spectra show fine structure similar to what has been seen in gas-phase Raman spectra. By considering all our absorption and Raman spectra for both H_2 and D_2, including temperature dependence and anharmonicities, and comparing the spectra to gas-phase Raman spectra, we have made unambiguous assignments for all observed spectral lines. As a result of these assignments, we conclude that H_2 and D_2 are trapped singly in interstitial sites in silica and are free to rotate. The absorption spectra provide information on the added loss due to H_2 saturation of silica optical fibers. For example, extrapolating the experimental results to the case of a fiber saturated under 1 atm of H_2, the added loss due to the intense first overtone Q-branch line is 14 dB/km at 1.2445 μm and 0.14 dB/km at 1.30 μm. High loss due to the fundamental absorption of H_2 occurs beyond 1.5 μm; at 1.55 μm it is 0.8 dB/km for 1 atm of H_2. There is, however, a transmission window in H_2-saturated fibers between 1.32 and 1.45 μm.

I. INTRODUCTION

During a study of the Raman gain properties of molecular hydrogen (H_2) diffused into silica fiber, it was found that H_2 in silica is infrared active with a broad absorption spectrum in a wavelength region extending from 2.4 μm into the visible. The report of this work showed

* AT&T Bell Laboratories.

Copyright © 1984 AT&T. Photo reproduction for noncommercial use is permitted without payment of royalty provided that each reproduction is done without alteration and that the Journal reference and copyright notice are included on the first page. The title and abstract, but no other portions, of this paper may be copied or distributed royalty free by computer-based and other information-service systems without further permission. Permission to reproduce or republish any other portion of this paper must be obtained from the Editor.

a portion of the first overtone spectrum between 1.0 and 1.4 μm (a region of interest for fiber optical transmission), along with tentative spectroscopic assignments.[1] This H_2 optical absorption in fibers subsequently was found to be of practical importance to lightwave communications with the observation of *in situ* generation of H_2 in optical fiber cables due to electrolysis.[2–4] Also, the recent literature contains calibrated first-overtone loss spectra for silica fibers containing H_2 under about 1-atm pressure, as well as spectral assignments for the fundamental and first-overtone regions.[1,3,5,6] We show here that all of the reported assignments are at least partially incorrect.

To obtain sufficient information for unambiguous assignment of all observed absorption lines, we have observed the absorption spectra of silica fibers impregnated with H_2 or D_2 at pressures that (1) are sufficiently high (500 atm) to produce gas concentrations in the fibers close to their saturation limits in silica, and (2) are larger by a factor of 50 than the highest pressures reported in other recent experiments.[4] The observations include calibrated fundamental and first- through third-overtone spectra for H_2, first- through fourth-overtone spectra for D_2, and spontaneous Raman spectra for both H_2 and D_2. The assignments made possible by measurements of these spectra also indicate that the "guest" molecules are trapped singly in the silica and are free to rotate.

II. EXPERIMENTS

In the experiments we employed several-hundred-meter lengths of multimode silica fiber with a 50-μm core and 125-μm outer diameter. The core contained a graded concentration of GeO_2 (about 14 percent GeO_2 at the center) and a small amount of P_2O_5. One fiber was subjected to H_2 at 500-atm pressure at room temperature for 30 days. We calculated the concentration of dissolved H_2 using the Langmuir adsorption model, with data adjusted to 25°C.[7] The resulting concentration of H_2 in the fiber was 5.6×10^{20} molecules/cm^3, which is about 500 times the reported concentration at 1 atm. We treated similar fiber with D_2 in the same way. In addition, we treated a 10m length of single-mode fiber in H_2 under the same conditions for five days. After treatment the fiber was removed from the pressure vessel and its spectra were measured at ambient atmospheric pressure. Between measurements the fibers were stored in liquid nitrogen to eliminate out-diffusion. The absorption spectra of all samples were obtained using a tungsten-lamp source and a 3/4-meter monochromator; all were normalized to the spectrum of an equal length of untreated fiber, and all were fully resolved. We chose absorption path lengths to ensure that the measured absorptions were within the dynamic range of the instrumentation. Raman spectra were obtained on the same mono-

chromator with a krypton-ion laser at 647.1-nm as the excitation source. The spectra were taken at room temperature and 77K.

III. RESULTS AND DISCUSSION

In the gas phase, direct absorption of infrared radiation is a rigorously forbidden process for homonuclear diatomic molecules, such as H_2 and D_2, due to their lack of a transition dipole moment.[8] The high symmetry of H_2 and D_2 dissolved in silica is reduced by the silica matrix surrounding the dissolved molecule, leading to induction of a transition dipole moment and absorption of infrared radiation resonant with molecular transition frequencies. Figure 1a shows the mea-

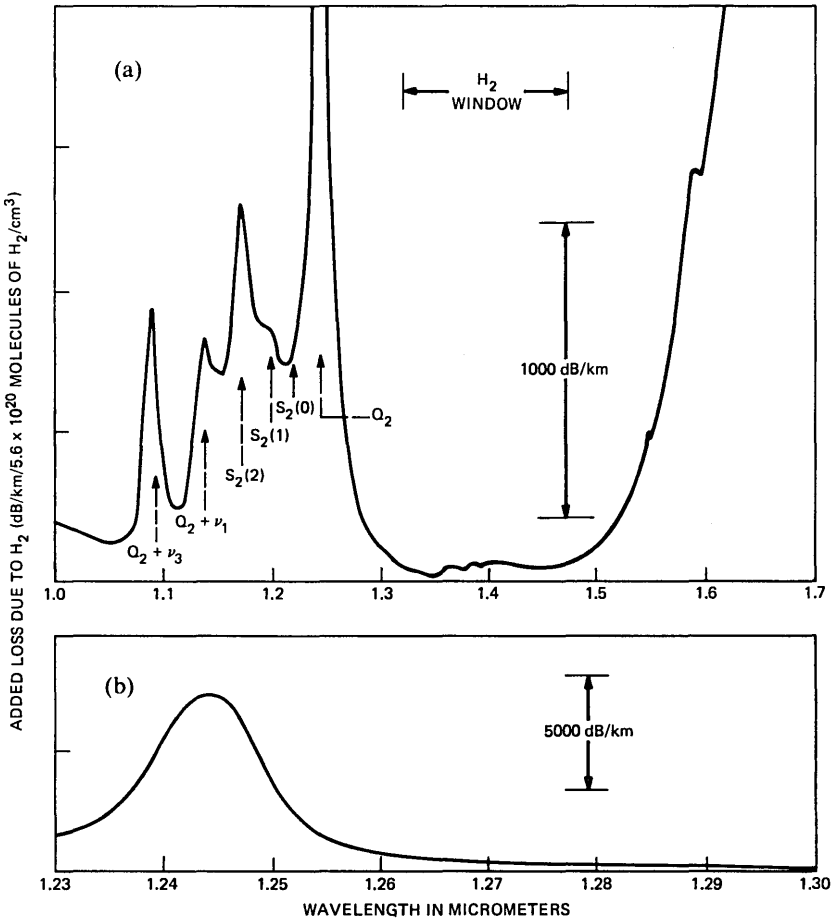

Fig. 1—First-overtone loss spectrum at room temperature of H_2 in silica fiber: (a) Entire spectrum of the first overtone, measured in a 10m single-mode fiber; ν_1 and ν_3 are silica vibrations;[9] (b) Expanded view of the most intense band, the Q branch, measured on 2.3m of multimode fiber.

sured H_2 loss spectrum between 1.0 and 1.6 μm for the single-mode fiber. Figure 1b shows the main absorption band, i.e., the Q branch of the first-overtone transition, measured at high resolution in the multimode fiber. Figures 2 and 3 show the second and third H_2-overtone absorption regions, respectively, for the multimode fiber. We also recorded spectra for the fundamental absorption region of H_2 and the first- through fourth-overtone regions of D_2, as well as Raman spectra for H_2 and D_2. HD was seen as an impurity in the D_2 spectra.

The spectra shown in Figs. 1 through 3 have the general features observed in all the absorption spectra. The strongest feature is identified as the Q-branch transition. Table I shows transition energies, wavelengths, and attenuation coefficients (measured for 500-atm treatment pressure, and reduced to 1 atm) for the observed Q branches of H_2, D_2, and HD. The spacing between successive vibrational levels (Q-branch spacing) decreases due to anharmonicity. Table I also shows the measured high-pressure attenuation coefficients and the derived 1-atm values. Note the large ratios of the H_2 and D_2 absorption strengths. We observed other weaker lines, and assigned these to vibration-rotation transitions, S(J) and O(J) lines (for a general description of the H_2 spectral lines see Ref. 8), or to combination absorptions with the silica tetrahedral modes ν_1 (800 cm^{-1}) and ν_3 (1100 cm^{-1}).[9] Figure 4 shows a correlation diagram of the Raman,

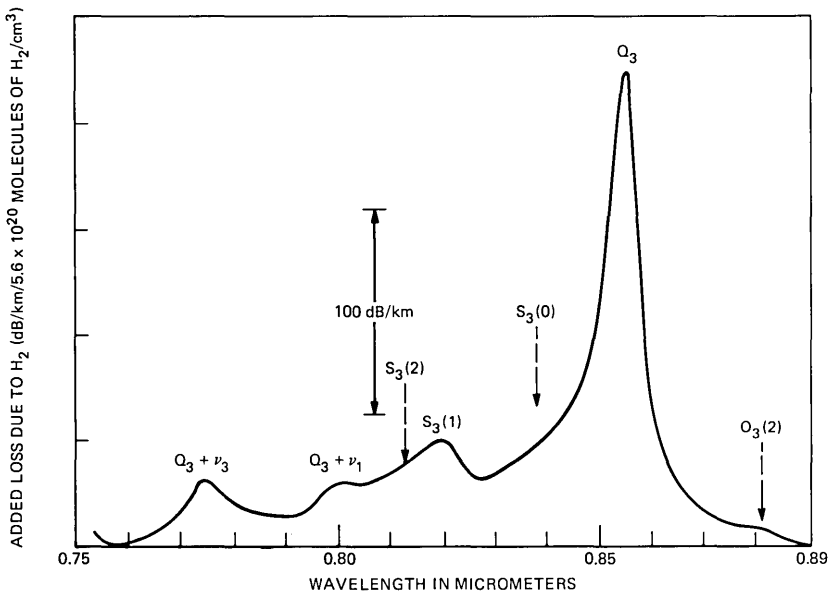

Fig. 2—Second-overtone spectrum of H_2 at room temperature measured on 13m of multimode fiber.

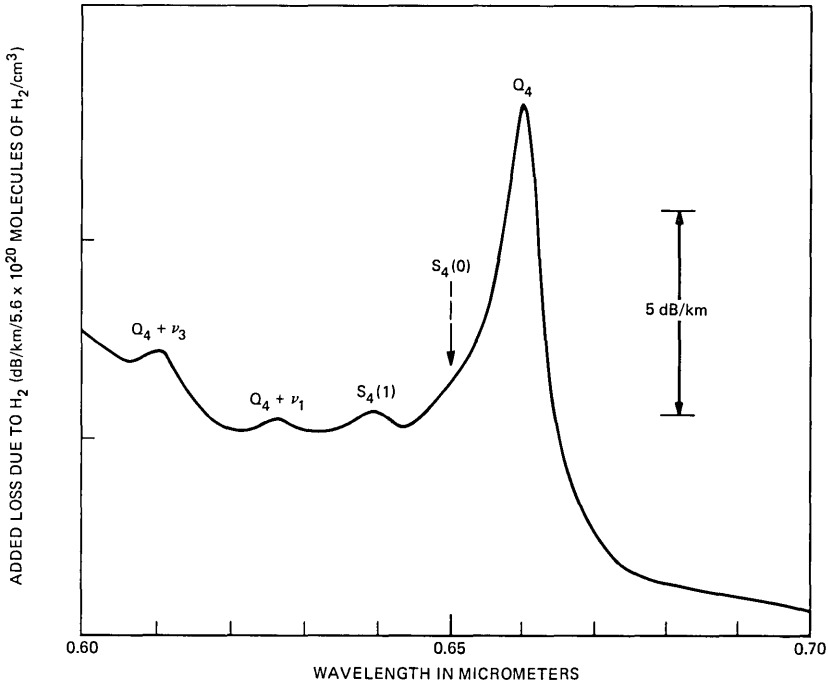

Fig. 3—Third-overtone spectrum of H_2 at room temperature measured on 450m of multimode fiber.

fundamental, and overtone lines for H_2, all relative to the Q-branch lines. If we reference the observed lines to the appropriate Q-branch transition, the consistency of the fine structure in each vibrational transition becomes apparent. This procedure also eliminates the energy shifts due to vibrational anharmonicity. Figure 5 shows similar results for the Raman and first four overtone lines of D_2, as well as gas-phase Raman lines[10] and the positions of the silica tetrahedral modes.[9]

The assignment of the S(J) and O(J) vibration-rotation lines is based on three factors:

1. The closer spacing and greater number of these lines in the D_2 spectra compared to the H_2 spectra, in accord with general expectations for the H-D isotope shifts.[8]

2. The excellent quantitative agreement between the rotational spacings observed in the fiber spectra for H_2 and D_2 compared to the spacings in the corresponding gas-phase spectra.

3. The relative intensities of the lines and the variation of relative intensities with temperature. [At 295K, the most intense rotational lines are S(1) for H_2 and S(2) for D_2. At 77K, the most intense lines are S(0) and S(1) for H_2 and S(0) for D_2.]

Table I—Observed Q-branch transition energies, $\bar{\nu}$, wavelengths, λ, and attenuation coefficients, α, HD room temperature data

	$\bar{\nu}$ (cm^{-1})	λ (μm)	α(dB/km) (a)	α(dB/km) (b)	Intensity (arb)
H_2					
Fundamental	4139	2.4159	4×10^5	800	—
1st Overtone	8035	1.2445	7100	14	—
2nd Overtone	11693	0.8552	260	0.52	—
3rd Overtone	15156	0.6598	13	0.026	—
4th Overtone					
D_2					
Fundamental	2975	3.361	—	—	—
1st Overtone	5828	1.716	2100	4.2	—
2nd Overtone	8565	1.1675	26	0.052	—
3rd Overtone	11198	0.8930	3.1	6.2×10^{-3}	—
4th Overtone	13699	0.7300	0.19	3.8×10^{-4}	—
HD					
Fundamental	3605	2.774	—	—	—
1st Overtone	7067	1.415	—	—	220
2nd Overtone	10293	0.9715	—	—	1
3rd Overtone	—	—	—	—	—
4th Overtone	—	—	—	—	—

(a) Measured coefficient for 500 atm, gas concentration = 5.6×10^{20} molecules/cm^3.
(b) Derived coefficient for 1 atm, gas concentration = 1.1×10^{18} molecules/cm^3.

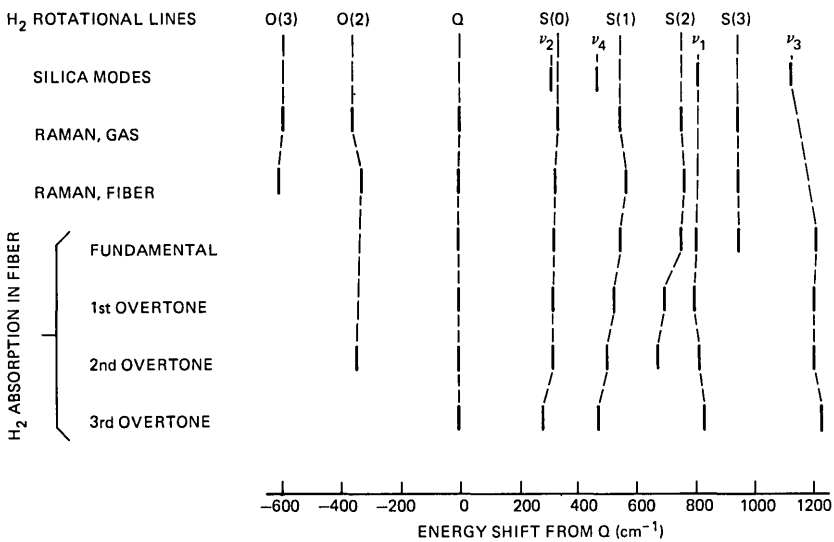

Fig. 4—Correlation diagram of Raman and fundamental and overtone absorption spectra of H_2 in silica. Frequencies are measured with respect to the Q-branch frequency. The gas-phase H_2 rotational structure[10] and silica tetrahedral vibrations[9] are shown.

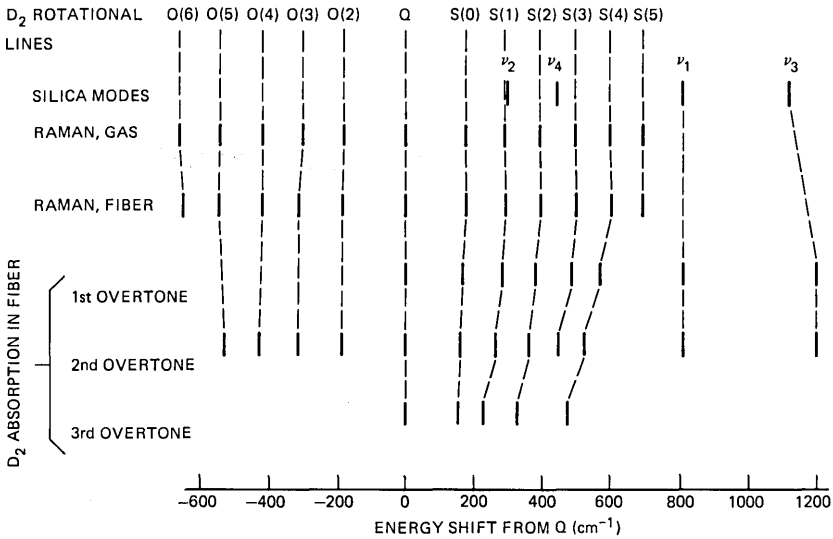

Fig. 5—Correlation diagram of Raman and overtone absorption spectra of D_2 in silica. Frequencies are measured with respect to the Q branch. The gas-phase D_2 rotational structure[10] and silica tetrahedral vibrations[9] are shown.

In contrast, the combination lines with the silica ν_1 and ν_3 modes show none of these effects; the separation from Q is the same in both the H_2 and D_2 spectra, and the intensities relative to Q and each other are independent of temperature. Even the fine details of Figs. 4 and 5 support the above interpretation. The S(J) lines shift closer to Q for the higher-overtone absorptions, as expected, due to rotation-vibration coupling for a nonrigid rotor.[8] In contast, the lines due to combination with the silica modes show no such shift.

Previous workers have observed many of the lines in the first-overtone spectrum reported here, but have made incorrect assignments, either assuming that all lines were due to combinations with silica modes,[6] which would indicate that the H_2 and D_2 did not rotate, or otherwise incorrectly identifying some of the transitions.[3,5] In a Raman study of H_2 and D_2 in bulk silica glass, Hartwig and Vitko observed the S(J) lines and thus concluded that the dissolved species rotated in interstitial sites in the glass.[11]

The full set of spectra that we have recorded, of which only a portion is shown here, contains a wealth of detailed information concerning the nature of H_2 and D_2 dissolved in silica. In a subsequent publication we shall present the complete spectra, a complete set of assignments for all the absorption and Raman spectra, and full analyses of the spectra. Table II identifies the lines of most importance for lightwave communication, those due to H_2 between 1.0 and 1.7 μm.

Table II—Observed transitions between 1.0 and 1.7 μm due to H_2 dissolved in a silica optical fiber

$\lambda(\mu m)$	Transition	Spectral Origin
1.696	$S_1(1) + \nu_3$	Fundamental
1.642	$S_1(2) + \nu_3$	Fundamental
1.590	$S_1(3) + \nu_3$	Fundamental
1.550	$Q_1 + 2\nu_3$	Fundamental
1.2445	Q_2	First overtone
1.197	$S_2(0)$	First overtone
1.1682	$S_2(1)$	First overtone
1.1455	$S_2(2)$	First overtone
1.1320	$Q_2 + \nu_1$	First overtone
1.0825	$Q_2 + \nu_3$	First overtone

The present work shows that H_2, even when dissolved close to saturation in silica, is still free to rotate. In contrast, when N_2 is diffused into a silica fiber, only a single band is observed in the Raman spectrum, and contributions from molecular rotation are absent (although it is possible that these are not observed due to the small concentration of N_2).[12] We also note confirmation of the fact that there is only a single gas molecule per site,[7] since no lines due to double excitations are observed, despite the very high gas concentration.

For H_2 the strongest component of the first overtone, Q_2, is very intense, about 7000 dB/km/5.6 $\times$ 10^{20} molecules/cm^3, but also very narrow. The absorption strength is about 70 dB/km/5.6 $\times$ 10^{20} molecules/cm^3 at 1.30 μm. These values correspond to 14 dB/km at 1.2445 μm, and 0.14 dB/km at 1.30 μm, for the H_2 concentration equivalent to 1 atm. Other reported values for the attenuation coefficient are considerably lower[2,4,6,13] for the Q branch but are in good agreement[2,4,6] at 1.30 μm. We believe this discrepancy in the peak attenuation coefficient of the Q branch is due to saturation that occurred in the other measurements of the intense Q-branch absorption. The absorption in the 1.5 to 1.6-μm portion of the spectrum is very large and increases rapidly with wavelength. The loss in this region is due to wings of the extremely intense fundamental absorption near 2.4 μm, which, like the overtones, is asymmetric and more intense toward shorter wavelengths. At 1.55 μm the absorption due to the wing of the fundamental absorption seen in Fig. 1a is about 400 dB/km/5.6 $\times$ 10^{20} molecule/cm^3 or 0.8 dB/km at 1 atm equivalent. Finally, we note that, even in the presence of H_2, there is a transmission window in silica from about 1.32 μm to about 1.45 μm, which might permit use of a hydrogen-contaminated fiber as a communications medium at a wavelength of approximately 1.4 μm. However, since this is the wavelength at which absorption in silica fibers due to OH contamination occurs,

such use would require the manufacture of fibers with negligible OH concentration. (No additional OH formation in silica due to H_2 has been observed below about 100°C.)[14]

In summary, we have recorded and analyzed both absorption spectra up to the fourth overtone, and Raman spectra for fibers saturated with either H_2 or D_2 at 500 atm. The spectral lines have been completely assigned to vibration-rotation transitions of H_2 (D_2) and combination vibrational transitions with only the ν_1 and ν_3 silica tetrahedral modes. The H_2 (D_2) molecule is trapped singly and is free to rotate.

REFERENCES

1. J. Stone, A. R. Chraplyvy, and C. A. Burrus, "Gas-in-Glass, A New Raman-Gain Medium: Molecular Hydrogen in Solid-Silica Optical Fibers," Opt. Lett. *7* (June 1982), pp. 297–9.
2. K. Mochizuki, Y. Namihara, and H. Yamamoto, "Transmission Loss Increase in Optical Fibers due to Hydrogen Permeation," Electr. Lett., *19* (September 1983), pp. 743–4.
3. N. Uesugi, Y. Murakami, C. Tanaka, Y. Ishida, Y. Mitsunagu, Y. Negishi, and N. Uchida, "Infrared Optical Loss Increase for Silica Fiber Cable Filled With Water," Electr. Lett., *19* (September 1983), pp. 762–4.
4. E. W. Mies, D. L. Philen, W. D. Reents, and D. A. Meade, "Hydrogen Susceptibility Studies Pertaining to Optical Fiber Cables," Conf. on Optical Fiber Commun., New Orleans, Louisiana, January 23–25, 1984, post deadline paper.
5. Y. Noguchi, K. Murakami, and K. Ishihara, "Infrared Loss Spectrum of Hydrogen Molecules in a Silica Fiber," Elec. Lett. *19* (November 1983), pp. 1045–6.
6. K. Mochizuki, Y. Namihara, M. Kuwazuru, and Y. Iwamoto, "Effects of Hydrogen on Infrared Absorption Characteristics in Optical Fibers," Conf. Optical Fiber Commun., New Orleans, Louisiana, January 23–25, 1984, paper WB2.
7. J. E. Shelby, "Molecular Diffusion and Solubility of Hydrogen Isotopes in Vitreous Silica," J. Appl. Phys., *48* (August 1977), pp. 3387–94.
8. G. Herzberg, *Spectra of Diatomic Molecules*, New York: Van Nostrand Reinhold, 1950.
9. J. Stone and G. E. Walrafen, "Overtone Vibrations of OH Groups in Fused Silica Optical Fibers," J. Chem. Phys., *76* (February 1982), pp. 1712–22.
10. B. P. Stoicheff, "High Resolution Raman Spectroscopy of Gases, IX. Spectra of H_2, HD, and D_2," Can. J. Phys., *35* (June 1957), pp. 730–41.
11. C. M. Hartwig and J. Vitko, "Raman Spectroscopy of Molecular Hydrogen and Deuterium Dissolved in Vitreous Silica," Phys. Rev., *B18* (October 1978), pp. 3006–14.
12. J. Stone, A. R. Chraplyvy, and C. A. Burrus, "Observation of Raman Scattering from N_2 in a Silica Optical Fiber," J. Noncrystal Solids, *63* (September 1984).
13. K. J. Beales, D. M. Cooper, and J. D. Rush, "Increased Attenuation of Optical Fibers Caused by Diffusion of Molecular Hydrogen at Room Temperature," Elec. Lett., *19* (October 1983), pp. 917–9.
14. J. Stone and C. A. Burrus, "Reduction of the 1.38 μm Water Peak in Optical Fibers by Deuterium-Hydrogen Exchange," B.S.T.J., *59* (October 1980), pp. 1541–8.

AUTHORS

Charles A. Burrus, Jr., B.S. (cum laude), 1950, Davidson College; M.S., 1951, Emory University, Ph.D., 1955, Duke University, all in physics; AT&T Bell Laboratories, 1955—. In 1955 Mr. Burrus joined the Technical Staff of AT&T Bell Laboratories, Holmdel, N. J., where he did research on the millimeter- and submillimeter-wave region of the spectrum (microwave spectroscopy and various types of semiconductor diodes for millimeter-wave use), and later on sources and detectors for lightwave communications (fiber-compatible LEDs, lasers, and p-i-n photodiodes). Currently, he works on both

sources and detectors for lightwave communications in the 1- to 1.6-μm wavelength region, and on the effects of deuterium and hydrogen in optical fibers. Member, Phi Beta Kappa, Sigma Pi Sigma, Sigma Xi; Fellow American Association for the Advancement of Science, the American Physical Society, the Institute of Electrical and Electronic Engineers, the Optical Society of America. He is the recipient of the 1982 David Richardson Medal in applied optics from the Optical Society of America and the Distinguished Technical Staff Award (1982) from AT&T Bell Laboratories.

Andrew R. Chraplyvy, A.B. (Physics), 1972, Washington University; M.S. (Physics), 1975, Cornell University; Ph.D (Physics), 1977, Cornell University; General Motors Research Laboratories, 1977–1980; AT&T Bell Laboratories, 1980—. Mr. Chraplyvy's research has included studies of nonlinear optical effects in fibers and generation of midinfrared radiation in waveguides as well as high-resolution spectroscopy of impurities in infrared transmitting materials. Member, American Physical Society, Optical Society of America.

Julian Stone, B.S. (Physics), 1950, The City College, New York: M.S. (Physics), 1951, and Ph.D. (Physics), 1958, New York University; AT&T Bell Laboratories, 1969—. Mr. Stone taught at The City College from 1952 to 1953 and 1956 to 1958. He was at The Hudson Laboratories of Columbia University from 1953 to 1969 where he was Associate Director for General Physics and was active in underwater acoustics and optics. At AT&T Bell Laboratories, Mr. Stone has been working on problems in optical transmission. Member, American Physical Society.

Jay M. Wiesenfeld, A.B. (Chemistry and Physics), 1972, A.M. (Physics), 1972, Harvard University; Ph.D (Chemistry), 1978, University of California, Berkeley; AT&T Bell Laboratories, 1978—. At AT&T Bell Laboratories, his work involves picosecond laser sources and their application to ultra-high-speed device performance and to the study of dynamics of solid-state and molecular systems, and the study of loss and dispersion properties of optical fibers. Member, American Chemical Society, American Physical Society, Optical Society of America.

PAPERS BY AT&T BELL LABORATORIES AUTHORS

COMPUTING/MATHEMATICS

Barron E. N., **Remarks on a Simple Optimal-Control Problem With Monotone Control Functions.** J Optim Th 41(4): 573–586, 1983.

Chung F. R. K., **On Optimal Linear Arrangements of Trees.** Comput Math 10(1): 43–60, 1984.

Henschen L. J., Naqvi S. A., **On Compiling Queries in Recursive First-Order Databases.** J ACM 31(1): 47–85, 1984.

Hwang F. K., Dekang Q., Yu J. E., **Complete Balanced Howell Rotations for 16K + 12 Partnerships.** J Comb Th A 36(1): 66–72, 1984.

Mitra D., Morrison J. A., **Asymptotic Expansions of Moments of the Waiting Time in Closed and Open Processor-Sharing Systems With Multiple Job Classes.** Adv Appl P 15(4): 813–839, 1983.

Simon B., **Priority Queues With Feedback.** J ACM 31(1): 134–149, 1984.

Simon B., Disney R. L., **Markov Renewal Processes and Renewal Processes—Some Conditions for Equivalence.** NZ Oper Res 12(1): 19–29, 1984.

Zave P., **The Operational Versus the Conventional Approach to Software Development.** Comm ACM 27(2): 104–118, 1984.

ENGINEERING

Brush G. G., Healy J. D., Liebesman B. S., **A Bayes Procedure for Combining Black-Box Estimates and Laboratory Tests.** P An Rel M (NSYM): 242–246, 1984.

Eisenstein G., Stulz L. W., **High-Quality Antireflection Coatings on Laser Facets by Sputtered Silicon-Nitride.** Appl Optics 23(1): 162–164, 1984.

Jackel J. L., Veselka J. J., **Measuring Losses in Optical Waveguides—A New Method (Letter).** Appl Optics 23(2): 197–199, 1984.

Lee T. P., Burrus C. A., Sessa W. B., **Q-Switching Cleaved-Coupled-Cavity Laser With an Integrated Intracavity Modulator.** Electr Lett 20(1): 1–2, 1984.

Marcuse D., Wiesenfeld J. M., **Chirped Picosecond Pulses—Evaluation of the Time-Dependent Wavelength for Semiconductor Film Lasers.** Appl Optics 23(1): 74–82, 1984.

Reeve H. C., Lim J. S., **Reduction of Blocking Effects in Image-Coding.** Opt Eng 23(1): 34–37, 1984.

Reichmanis E., Wilkins C. W., Ong E., **Materials for Multilevel Resist Schemes.** Polym Eng S 23(18): 1039–1042, 1983.

Siller C. A., **Multipath Propagation.** IEEE Comm M 22(2): 6–15, 1984.

Taylor G. N., Hellman M. Y., Feather M. D. Willenbrock W. E., **Evaluation of the Influence of Process Factors on Plasma-Developed X-Ray Resist Properties.** Polym Eng S 23(18): 1029–1038, 1983.

White J. C., **Proposal for Vacuum Ultraviolet Antistokes Raman Lasers Based on the Group-VI Elements.** Optics Lett 9(2): 38–40, 1984.

Wilkins C. W., Reichmanis E., Chandross E. A., Hartless R. L., **Deep UV Photolithographic Systems and Processes.** Polym Eng S 23(18): 1025–1028, 1983.

PHYSICAL SCIENCES

Ahlers G., Hohenberg P. C., **Background Terms for Second-Sound Damping Near T-Lambda (Letter).** Phys Rev L 52(4): 313, 1984.

Alpar M. A., Anderson P. W., Pines D., Shaham J., **Vortex Creep and the Internal Temperature of Neutron Stars. 1. General Theory.** Astrophys J 276(1): 325–334, 1984.

Aspnes D. E., Studna A. A., Kinsbron E., **Dielectric Properties of Heavily Doped Crystalline and Amorphous Silicon From 1.5 to 6.0 EV.** Phys Rev B 29(2): 768–779, 1984.

Bastard G. et al., **Bound and Virtual Bound States in Semiconductor Quantum Wells.** Sol St Comm 49(7): 671–674, 1984.

Bean J. C., Sheng T. T., Feldman L. C., Fiory A. T., Lynch R. T., **Pseudomorphic Growth of Ge_xSi_{1-x} on Silicon by Molecular-Beam Epitaxy.** Appl Phys L 44(1): 102–104, 1984.

Becker R. S., Higashi G. S., Golovchenko J. A., **Low-Energy Electron Diffraction During Pulsed Laser Annealing—A Time-Resolved Surface Structural Study.** Phys Rev L 52(4): 307–310, 1984.

Blumberg W. E., Eisinger J. Lamola A. A., Zuckerman D. M., **Principles and Applications of Hematofluorometry.** J Cl L Aut 4(1): 29–42, 1984.

Bohn P. W., Bhat R., Harris T. D., **Determination of Trace Constituents of High-Purity Gallium-Arsenide.** Analyt Chem 56(1): 58–62, 1984.

Bonner W. A., Temkin H., **Preparation and Characterization of High-Purity Bulk InP.** J Cryst Gr 64(1): 10–14, 1983.

Cava R. J., Murphy D. W., Rietman E. A., Zahurak S. M., Barz H., **Lithium Insertion, Electrical Conductivity, and Chemical Substitution in Various Crystallographic Shear Structures.** Sol St Ion 9-10(Dec): 407–411, 1983.

Chen C. Y., Pang Y. M., Alavi K., Cho A. Y., Garbinski P. A., **Interdigitated $Al_{0.48}In_{0.52}As/Ga_{0.47}In_{0.53}As$ Photoconductive Detectors.** Appl Phys L 44(1): 99–101, 1984.

Cladis P. E. et al., **Elasticity of Blue Phase-1 of Cholesteric Liquid Crystals.** Phys Rev L 52(7): 542–545, 1984.

Coldren L. A., Ebeling K. J., Swartz R. G., Burrus C. A., **Stabilization and Optimum Biasing of Dynamic Single-Mode Coupled-Cavity Lasers.** Appl Phys L 44(2): 169–171, 1984.

Cooper J. A., **Power Law Broadening of Charge Packets at Semiconductor Interfaces.** Appl Phys L 44(2): 243–245, 1984.

Cullen P., Harbison J. P., Lang D. V., Adler D., **Space-Charge Spectroscopy of the Gap States in Hydrogenated Amorphous Silicon Counterdoped With Boron.** J Non Cryst 59-6(Dec): 261–264, 1983.

Dutta N. K., Agrawal G. P., Focht M. W., **Bistability in Coupled-Cavity Semiconductor Lasers.** Appl Phys L 44(1): 30–32, 1984.

Eibschutz M., Lines M. E., Chen H. S., Masumoto T., **Amorphous Structural Information From Mossbauer Zeeman Spectra—Iron Metalloid Systems.** J Phys F 14(2): 505–520, 1984.

Fisher D. S. et al., **Dynamics of Charge-Density Waves Pinned by Impurities—Comment (Letter).** Phys Rev L 52(6): 481, 1984.

Glass A. M., Liao P. F., Johnson A. M., Humphrey L. M., Lemons R., Olson D. H. Stern M. B., **Periodically Structured Amorphous-Silicon Detectors With Improved Picosecond Responsivity.** Appl Phys L 44(1): 77–79, 1984.

Graebner J. E. et al., **Solid Hydrogen in Hydrogenated Amorphous Silicon.** Phys Rev L 52(7): 553–556, 1984.

Kaplan M. L., Forrest S. R., Schmidt P. H., Venkatesan T., **Optical and Electrical-Properties of Ion-Beam-Irradiated Films of Organic Molecular Solids and Polymers.** J Appl Phys 55(3): 732–742, 1984.

Kastalsky A., Hwang J. C. M., **Illumination-Stimulated Persistent Channel Depletion at Selectively Doped $Al_{0.3}Ga_{0.7}As/GaAs$ Interface.** Appl Phys L 44(3): 333–335, 1984.

Keith H. D., Padden F. J., **Twisting Orientation and the Role of Transient States in Polymer Crystallization.** Polymer 25(1): 28–42, 1984.

Liao A. S. H., Tell B., Leheny R. F., Chang T. Y., Caridi E. A., Beebe E., Dewinter J. C., **Electron Transport in $In_{0.53}Ga_{0.47}As$/Plasma Oxide Inversion Layers.** Appl Phys L 44(3): 344–345, 1984.

Lin B. J. F., Paalanen M. A., Gossard, A. C., Tsui D. C., **Weak Localization of Two-Dimensional Electrons in GaAs-Al_xGa_{1-x} Heterostructures.** Phys Rev B 29(2): 927–934, 1984.

Lundgren J. O. et al., **Neutron-Diffraction Structural Study of Pyroelectric $Li_2SO_4 \cdot H_2O$ at 293, 80, and 20K.** J Chem Phys 80(1): 423–430, 1984.

Mahajan S., Temkin H., Logan R. A., **Formation of Optically Induced Catastrophic Degradation Lines in InGaAsP Epilayers.** Appl Phys L 44(1): 119–121, 1984.

McAfee K. B., Szmanda C. R., Hozack R. S., **Observation of 5S Nitrogen Metastable State in Charge-Exchange Collisions.** J Chem Phys 80(1): 267–271, 1984.

McKoy V., Lynch D., Lucchese R. R., **Dynamics of Molecular Photoionization Processes.** Int J Quant (517): 89–100, 1983.

Miller T. A., **Chemistry and Chemical Intermediates in Supersonic Free Jet Expansions.** Science 223(4636): 545–553, 1984.

Miyoshi T., Tien P. K., Martin R. J., Tennant D. M., Johnson A. M., Downey P. M., **Infrared Photodetection in Proton-Bombarded InP.** Appl Phys L 44(1): 128–130, 1984.

Moore C. A., Davis G. P., Gottscho R. A., **Sensitive, Nonintrusive, Insitu Measurement of Temporally and Spatially Resolved Plasma Electric Fields.** Phys Rev L 52(7): 538–541, 1984.

Murphy D. W., Cava R. J., Zahurak S. M., Santoro A., **Ternary Li_xTiO_2 Phases From Insertion Reactions.** Sol St Ion 9–10(Dec): 413–417, 1983.

Petroff P. M., Miller R. C., Gossard A. C., Wiegmann W., **Impurity Trapping, Interface Structure, and Luminescence of GaAs Quantum Wells Grown by Molecular-Beam Epitaxy.** Appl Phys L 44(2): 217–219, 1984.

Rosamilia J. M., Miller B., **Rapid Potential Scan at Rotating-Disk Electrodes Under Sinusoidal Hydrodynamic Modulation.** J Elec Chem 160(1–2): 131–140, 1984.

Shah J., Pinczuk A., Stormer H. L., Gossard A. C., Wiegmann W., **Hot Electrons in Modulation-Doped GaAs-AlGaAs Heterostructures.** Appl Phys L 44(3): 322–324, 1984.

Sompholinsky H. et al., **Exchange Stiffness and Macroscopic Anisotrophy in Heisenberg Spin Glasses.** Phys Rev L 52(5): 392–395, 1984.

Steinberg V., Brand H. R., **Amplitude Equations for the Onset of Convection in a Reactive Mixture in a Porous Medium.** J Chem Phys 80(1): 431–435, 1984.

Stormer H. L., Gossard A. C., Wiegmann W., Blondel R., Baldwin K., **Temperature Dependence of the Mobility of Two-Dimensional Hole Systems in Modulation-Doped GaAs-(AlGa)As.** Appl Phys L 44(1): 139–141, 1984.

Temkin H., Logan R. A., Vanderziel J. P., **Influence of Orientation-Dependent Growth Kinetics on the Performance of InGaAsP Buried Crescent Lasers.** Appl Phys L 44(2): 160–162, 1984.

Tiong K. K., **Effects of As^+ Ion-Implantation on the Raman Spectra of GaAs—Spatial Correlation Interpretation.** Appl Phys L 44(1): 122–124, 1984.

Tsang W. T., **$Ga_{0.47}In_{0.53}As$/InP Multiquantum-Well Heterostructure Lasers Grown by Molecular-Beam Epitaxy Operating at 1.53 μm.** Appl Phys L 44(3): 288–290, 1984.

Tully J. C., Cardillo M. J., **Dynamics of Molecular Motion at Single-Crystal Surfaces.** Science 223(4635): 445–450, 1984.

Walstedt R. E., **Spin-Glass Behavior in Finite Numerical Samples.** Lect N Phys 192: 177–202, 1983.

Weber T. A., Stillinger F. H., **Pressure Melting of Ice.** J Chem Phys 80(1): 438–443, 1984.

Wilson B. A., Hu P., Harbison J. P., Jedju T. M., **Subnanosecond Photoluminescence in A-Si-H.** J Non-Cryst 59-6(Dec): 341–344, 1983.

Wilt D. P., Schwartz B., Tell B., Beebe E. D., Nelson R. J., **Channeled Substrate Buried Heterostructure InGaAsP/InP Laser Employing a Buried Fe Ion Implant for Current Confinement.** Appl Phys L 44(3): 290–292, 1984.

Woolery G. L., Powers L., Winkler M., Solomon E. I., Spiro T. G., **EXAFS Studies of Binuclear Copper Site of Oxyzidohemocyanin, Deoxyzidohemocyanin, Metaquozidohemocyanin, Metfluorozidohemocyanin, and Metazidohemocyanin From Arthropods and Mollusks.** J Am Chem S 106(1): 86–92, 1984.

SOCIAL AND LIFE SCIENCES

Julesz B., **The Role of Analog Models in Our Digital Age.** Behav Brain 6(4): 668–669, 1983.

Poltrock S. E., Shaw M., **Failures of Grossberg Theory to Compute Depth, Form, and Lightness.** Behav Brain 6(4): 671–673, 1983.

SPEECH AND ACOUSTICS

Francis S. H., Slazak M., Berryman J. G., **Response of Elastic Cylinders to Convective Flow Noise. 1. Homogeneous, Layered Cylinders.** J Acoust So 75(1): 166–172, 1984.

CONTENTS, SEPTEMBER 1984

On Hidden Markov Model and Dynamic Time Warping for Speech Recognition—A Unified View
B.-H. Juang

On the Performance of Isolated Word Speech Recognizers Using Vector Quantization and Temporal Energy Contours
L. R. Rabiner, K. C. Pan, and F. K. Soong

The Overload Performance of Engineered Networks With Nonhierarchical and Hierarchical Routing
J. M. Akinpelu

Methods in Traffic Calculations
D. L. Jagerman

On the Capacity of Sticky Storage Devices
H. S. Witsenhausen

Velocity-Saturated Characteristics of Short-Channel MOSFETs
G. W. Taylor

AT&T BELL LABORATORIES TECHNICAL JOURNAL is abstracted or indexed by *Abstract Journal in Earthquake Engineering, Applied Mechanics Review, Applied Science & Technology Index, Chemical Abstracts, Computer Abstracts, Current Contents/Engineering, Technology & Applied Sciences, Current Index to Statistics, Current Papers in Electrical & Electronic Engineering, Current Papers on Computers & Control, Electronics & Communications Abstracts Journal, The Engineering Index, International Aerospace Abstracts, Journal of Current Laser Abstracts, Language and Language Behavior Abstracts, Mathematical Reviews, Science Abstracts (Series A, Physics Abstracts; Series B, Electrical and Electronic Abstracts; and Series C, Computer & Control Abstracts), Science Citation Index, Sociological Abstracts, Social Welfare, Social Planning and Social Development,* and *Solid State Abstracts Journal.* Reproductions of the Journal by years are available in microform from University Microfilms, 300 N. Zeeb Road, Ann Arbor, Michigan 48106.

AT&T
Bell Laboratories